UNIVERSITÀ DEGLI STUDI DI UDINE

Dipartimento di Energetica e Macchine
Corso di Dottorato in Tecnologie Chimiche ed Energetiche

Tesi di Dottorato

A VORTEX PANEL METHOD FOR VAWT IN DYNAMIC STALL

Relatore:	Dottorando:
Prof. PIETRO GIANNATTASIO	ALESSANDRO ZANON

ANNO ACCADEMICO 2010-2011

"I have not the smallest molecule of faith in aerial
navigation other than ballooning or of expectation of
good results from any of the trials we hear of."
William Thomson, 1st Baron Kelvin

Acknowledgements

First of all, I would like to thank my supervisor, Prof. Pietro Giannattasio for the illuminating advice, support and encouragement he has given to me during the Ph.D. course. Thanks also for the endless nights spent in the patient and meticulous reading of the present thesis. His critical perspective of the nature behaviour was always source of inspiration to me; working with him was a pleasure!!

Loving thanks to Valentina, my girlfriend, for her support when I was a bit, just a bit, hysterical and, especially, for her travelling across Europe just to spend a couple of days with me. Thanks to wait for me. Many thanks to my family that always supported me.

Many thanks to my office colleagues, Alessandro and Claudio, who had to bear my strange exclamations and to offer me a coffee every day :) Many thanks also to Luca who supported me since my M.Sc. degree and made my abroad experience possible.

I'm grateful to Prof. Fulvio Scarano, for welcoming me in Delft and for giving to me the opportunity and the tips to collect the experimental data. Many thanks to Andrea Nati, for the amazing three months spent in the wind tunnel facility, for his acknowledgements and for making me to feel like at home in the flat Holland. Anyway, I'm still waiting the climbing session in the Dolomites!!! Many thanks also to the omniscient Roeland de Kat for the coffee breaks, the precious advices and the help in understanding how Davis works...

Of course, I would like to thank Carlos Simão Ferreira for his precious help in introducing me in the present research field, in understanding how rotating things can produce energy and for the copy of his PhD thesis! It has been a source of endless inspiration for me.

I would like to thank Professors Pascazio and Ricci for their precious advices and suggestions in the review of the present thesis.

Finally, I thank the University of Udine and the department of "Energetica e Macchine" for giving to me the opportunity to become a Ph.D.

Abstract

An efficient and accurate model has been developed for the numerical simulation of a Vertical Axis Wind Turbine (VAWT) in its whole operating range and with emphasis to the dynamic stall condition. In order to reproduce the main features of the separated flow (e.g., the shedding of strong vortical structures), an unsteady 2D panel code has been developed, which uses the “double wake” concept to model the physics of the dynamic stall.

The panel equations for the unsteady potential flow are solved together with the integral boundary layer equations on the aerofoil surface, by using a semi-inverse iterative algorithm to couple the inviscid and viscous flow regions. Both the wake and the flow separation are modelled by introducing two additional panels at the trailing edge and separation point, respectively, and by computing the change in the aerofoil bound circulation on the basis of the shedding of point vortices from those locations (“double wake” approach). The point vortices are convected by the flow according to the local velocities induced by the point vortex population itself and by the singularities on the aerofoil surface. Since an accurate prediction of the separation point is essential for a successful simulation a rather complex model of the boundary layer, including a proper treatment of the transition bubble, has been adopted. Furthermore, an appropriate strategy has been devised to move the separation panel so as to allow the flow reattachment required in condition of dynamic stall at low *Reynolds* numbers.

The model has been validated with reference to a steady and a pitching aerofoil in dynamic stall at high and low *Reynolds* numbers ($Re = 1.5 \times 10^6$ and $Re = 5 \times 10^4$). The numerical results have been compared with experimental data from the literature and with time-resolved PIV measurements performed by the author. An excellent agreement is observed in both attached and separated flow conditions. In particular, satisfactory predictions are obtained of aerodynamic loads, separation and reattachment points, position and shape of the separated shear layer. For the pitching aerofoil, the load hysteresis loops and the dynamics of the leading edge vortex, which characterises the dynamic stall, are well predicted at two pitching frequencies, which proves the good sensitivity of the model to the variation rate of the angle of attack. Also the flow reattachment in dynamic stall is properly simulated thanks to the special strategy devised to move the separation panel along the aerofoil surface.

The model has been used to compute the wake flow past a VAWT in dynamic stall and the numerical results have been compared with phase-locked

PIV data and CFD-DES simulations available in the literature. The complex vorticity distribution due to the energy conversion process is well reproduced, showing the ability of the present model to cope with separated flows and strong wake-blade interactions. The predicted values of the forces turn out to be comparable with the ones provided by the much more expensive CFD approaches.

Subsequently, a study has been carried out about the influence of dynamic stall, number of blades and reduced frequency on the VAWT vorticity field and forces. When compared with a single wake model, which cannot allow for the dynamic stall, the present model predicts much more complex vorticity and induction fields characterised by the release of vorticity of opposite signs from the separation point and the trailing edge, which strongly alters the dynamics of the blade-wake interaction. When considering a two blades VAWT instead of a single blade one, vorticity is observed to accumulate in the downwind region, which causes a strong expansion of the main flow crossing the rotor. A low reduced frequency, corresponding to a condition named “quasi-steady stall” in the present work, gives rise to the release of vortical structures at a frequency much higher than the rotation frequency, which introduces high frequency oscillations in the aerodynamic forces and reduces the power extraction in the downwind part of the blade rotation.

Finally, the 2D VAWT rotor performance, in terms of power coefficient vs. tip speed ratio, has been computed for two different rotor *Reynolds* numbers. As expected, the power coefficient increases with the rotor *Reynolds* number in the whole operating range of the wind turbine. However, in the present thesis no attempt is made to compare the predicted overall performance with that of a real three dimensional VAWT, since the complex 3D effects (e.g., tip vortices) cannot be either neglected or reproduced by a 2D model. Therefore, the extension of the present model to three dimensions, which is a very challenging task, should be pursued in future works.

Contents

List of Figures **xiii**

Nomenclature **xvii**

1 Introduction **1**
1.1 Wind Energy 2
1.2 2D VAWT aerodynamics 5
1.3 Numerical methods for VAWT 7
1.3.1 Momentum models 7
1.3.2 Vortex Methods 9
1.3.3 Computational Fluid Dynamics 10
1.4 Motivation of the research project 11
1.5 2D flow assumption 12
1.6 Previous works 13
1.7 Thesis outline 15

2 Formulation of the Model **17**
2.1 Potential flow equations and panel method 18
2.1.1 Attached Flow 26
2.1.2 Separated Flow 29
2.1.3 The unsteady Kutta condition 34
2.2 Viscous Boundary Layer 36
2.3 Viscous-Inviscid Interaction 40
2.3.1 Definition of Transpiration Velocity 40
2.3.2 Coupling Algorithm 42
2.3.3 Coupling Procedure 45

3 Computational procedure **47**
3.1 Code structure 47
3.2 Numerical Details 50
3.3 Separation criterion 55

4 Validation of the Numerical Model **61**
4.1 Naca 0015, steady and pitching motion 61
4.2 Naca 0012, comparison with time-resolved 2D PIV data . . . 64
4.2.1 Wind Tunnel facility 64
4.2.2 PIV optical arrangement 66
4.2.3 Overview of the PIV data collected 66

4.2.4 Load estimation from the time-resolved 2D-PIV data . 67
4.2.5 Steady Aerofoil Results 71
4.2.6 Pitching aerofoil results, low reduced frequency 76
4.2.7 Pitching aerofoil results, high reduced frequency . . . 80

5 Results 87
5.1 Vertical Axis Wind Turbine 87
5.2 Influence of the dynamic stall on the vorticity field 93
5.3 Influence of the number of blades 99
5.4 Comparison between dynamic and quasi-steady stall 105
5.5 VAWT performance 110

6 Conclusions 113

Appendices 115

A Laminar Closure Relationships 117
A.0.1 Skin friction coefficient (C_f) 117
A.0.2 Dissipation coefficient (C_D) 117
A.0.3 Energy thickness shape parameter (H^*) 117

B Turbulent Closure Relationships 119
B.0.4 Skin friction coefficient (C_f) 119
B.0.5 Dissipation coefficient (C_D) 119
B.0.6 Energy thickness shape parameter (H^*) 119
B.0.7 Equilibrium shear stress coefficient ($C_{\tau eq}$) 120
B.0.8 Normalised wall slip velocity (U_s) 120
B.0.9 Boundary layer thickness (δ) 120
B.0.10 $G - \beta$ locus ($\frac{1}{w_e}\left(\frac{\partial w_e}{\partial s}\right)_{eq}$) 120

C Wake Closure Relationships 121
C.0.11 Dissipation coefficient (C_D) 121
C.0.12 Energy thickness shape parameter (H^*) 121
C.0.13 Equilibrium shear stress coefficient ($C_{\tau eq}$) 121
C.0.14 Normalised wall slip velocity (U_s) 122
C.0.15 Boundary layer thickness (δ) 122
C.0.16 $G - \beta$ locus ($\frac{1}{w_e}\left(\frac{\partial w_e}{\partial s}\right)_{eq}$) 122

References **123**

List of Figures

1.1 The VAWT as an object of design, by Philippe Starck 2
1.2 Example of HAWT and VAWT 3
1.3 3D Flow past a wing 3
1.4 Evolution of trailing vorticity in a HAWT wake 4
1.5 Wake of a single blade VAWT 5
1.6 Schematic behaviour of a VAWT 6
1.7 Expansion of the wake due to the energy extraction in a HAWT 7
1.8 The actuator strip and the streamtube configuration 8
1.9 Evolution of the velocity in the freestream direction (U_x), 2D vs 3D 12
1.10 Wake path in a midplane of a VAWT,2D vs 3D 13
1.11 Example of ibrid model 14

2.1 Flow regions for high *Reynolds* numbers 18
2.2 Control Volume for the application of the divergence theorem 19
2.3 Nomenclature for derivation of Green's identity 20
2.4 Definition of potential inside aerofoil 21
2.5 Definition of panels 22
2.6 Point vortex 23
2.7 Constant Strength vortex distribution 25
2.8 Constant Strength source distribution 26
2.9 Singularities distribution in the attached flow condition 27
2.10 Kelvin Theorem 29
2.11 Circulation in the separated shear layer 30
2.12 Control volume across the boundary layer 30
2.13 Singularities distribution in the separated flow condition 32
2.14 Separation Point 34
2.15 Trailing Edge 35
2.16 Boundary layer on an Aerofoil at high angle of attack 39
2.17 Direct Method 43
2.18 Inverse Method 43
2.19 Semi-inverse Method 44
2.20 Semi-inverse Method, present code 45

3.1 Flow-chart of the solution procedure. 49
3.2 Skin friction coefficient on the suction side of a Naca 0012 . . 55
3.3 Pressure coefficient during downstroke 56
3.4 Normal force coefficient C_n during the downstroke 57

3.5 Angles of attack of reattachment start and end 58

4.1 Comparison of steady lift coefficient. NACA 0015, $Re = 1.5 \times 10^6$. 62
4.2 Lift coefficient, pitching aerofoil NACA 0015 63
4.3 Jet section of the wind tunnel. 64
4.4 Camera and laser setup for PIV measurements. 65
4.5 Field of view of the two cameras 66
4.6 Integration domain for the evaluation of fluid-dynamic forces . 68
4.7 PIV mean vorticity field. NACA 0012 aerofoil, $\alpha = 6°$. 69
4.8 Control surfaces and reference frames for forces evaluation . . 70
4.9 Unfiltered drag coefficient of a cylinder 72
4.10 Filtered drag coefficient of a cilinder 72
4.11 Unfiltered lift coefficient of a pitching aerofoil for $\kappa = 0.15$ . . 73
4.12 Power spectrum of the signal in Fig. 4.11 73
4.13 Results of the cross-correlation of the signal in Fig. 4.11 with its filtered counterpart 74
4.14 Filtered and unfiltered lift coefficient from the PIV data . . . 74
4.15 Mean vorticity field, a) Vortex panel model b) PIV data 75
4.16 Steady flow past a NACA 0012 aerofoil, $Re = 5 \times 10^4$ 76
4.17 Pitching motion results for a NACA 0012 aerofoil at $\kappa = 0.05$ 77
4.18 Instantaneous vorticity field during pitching motion. $\alpha = 12.6°$. 78
4.19 Instantaneous vorticity field during pitching motion. $\alpha = 14°$. 79
4.20 Instantaneous vorticity field during pitching motion. $\alpha = 16.8°$. 80
4.21 Pitching motion results for a NACA 0012 aerofoil at $\kappa = 0.15$ 81
4.22 Instantaneous vorticity field during pitching motion. $\alpha = 16°$. 82
4.23 Instantaneous vorticity field during pitching motion. $\alpha = 19.2°$. 83
4.24 Instantaneous vorticity field during pitching motion. $\alpha = 20°$. 84
4.25 Instantaneous vorticity field during pitching motion. $\alpha = 19°$. 85

5.1 Evolution of the leading edge vortex. PIV data 88
5.2 Evolution of the leading edge vortex. Vortex model 88
5.3 Evolution of the trailing edge vortex. PIV data 89
5.4 Evolution of the trailing edge vortex. Vortex model 89
5.5 Integration contour 90
5.6 Circulation of the VAWT leading edge 91
5.7 Normal forces, Vortex Model vs. CFD 92
5.8 Tangential forces, Vortex Model vs. CFD 93
5.9 Results of the single wake panel model 94
5.10 Results of the double wake panel model 94

5.11 Results of the single wake panel model, phase locked average . 95
5.12 Results of the double wake panel model, phase locked average 96
5.13 Induction factor for the single and double wake models 97
5.14 Angle of attack for the single and double wake models 97
5.15 Two-blades VAWT, time-averaged vorticity distribution 99
5.16 Two-blades VAWT, Phase locked average 100
5.17 Tangential forces over one rotation, one- and two-blades VAWT 101
5.18 Normal forces over one rotation, one- and two-blades VAWT . 101
5.19 Induction factor over one rotation, one- and two-blades VAWT 102
5.20 Induction factor in y direction, one and two bladed VAWT . . 102
5.21 Angles of attack over one rotation, one- and two-blades VAWT 103
5.22 Streamlines and contour plot of the mean velocity field, two-blades VAWT 104
5.23 Streamlines and contour plot of the mean velocity field, one-blade VAWT 104
5.24 Three blades VAWT, time-average vorticity distribution 106
5.25 Three blades VAWT, phase locked averaged vorticity 107
5.26 Normal forces over one rotation, dynamic stall ($\kappa = 0.125$), quasi-steady stall ($\kappa = 0.0416$) and $Re = 5 \times 10^4$ 108
5.27 Tangential forces over one rotation, dynamic stall ($\kappa = 0.125$), quasi-steady stall ($\kappa = 0.0416$) and $Re = 5 \times 10^4$ 108
5.28 Perceived angle of attack over one rotation, dynamic stall ($\kappa = 0.125$), quasi-steady stall ($\kappa = 0.0416$) and $Re = 5 \times 10^4$ . . 109
5.29 Induction factor over one rotation, dynamic stall ($\kappa = 0.125$), quasi-steady stall ($\kappa = 0.0416$) and $Re = 5 \times 10^4$ 109
5.30 Induction factor in y direction, dynamic stall ($\kappa = 0.125$), quasi-steady stall ($\kappa = 0.0416$) and $Re = 5 \times 10^4$ 110
5.31 Power coefficient vs. tip speed ration λ 111

Nomenclature

α	Angle of attack [deg]
$\bar{\xi}$	Continuous function of position inside V
$\bar{A}$	Influence Matrix of a source panel
$\bar{B}$	Influence Matrix of a vorticity panel
$\bar{C}$	Influence Matrix of the panel in the trailing edge wake
$\bar{D}$	Influence Matrix for a vortex blobs [$1/m$]
$\bar{f}$	Body volume forces [m/s^2]
$\bar{n}$	Vector normal to the surface
$\bar{x}$	Position vector
χ	Strength of a doublet
δ^*	Displacement thickness[m]
δ^{**}	Density thickness[m]
Γ	Circulation [m^2/s]
γ	Strength of the vorticity panel [m/s]
κ	Reduced frequency
λ	Tip speed ration of Vertical axis wind turbine $\Omega R_{VAWT}/u_\infty$
μ	Dynamic viscosity [$Pa \cdot s$]
ν	Kinematic viscosity [m^2/s]
Ω	Rotation velocity of Vertical Axis Wind Turbine, or pitching aerofoil [$1/rad$]
ω	Vorticity [rad/s]
ϕ	Velocity potential [m^2/s]
ϕ_s	Potential of a source of unit strength
ρ	Air density [Kg/m^3]

σ	Strength of the source panel $[m/s]$
τ	Total shearing plus Reynolds stresses $[Kg/ms^2]$
τ_w	Wall shear stress $[Pa]$
θ	Angular coordinate $[rad]$
ϑ	Momentum thickness $[m]$
ϑ^*	Kinetic energy thickness$[m]$
a	Induction factor $1 - u_x/u_\infty$
C_D	Dissipation coefficient
C_f	Skin friction coefficient
C_l	Lift coefficient
$C_{\tau eq}$	Shear stress coefficient of an equilibrium flow
C_τ	Shear stress coefficient
C_p	Power coefficient
Dim	Dimension of the space
f, g	Symbolic functions
H, H^*, H^{**}	Shape parameters
k	Coefficient of the boundary layer
K_{rx}	Under relaxation coefficient
l	Length of a panel or a surface, depends on the subscription $[m]$
L, c	Aerofoil chord$[m]$
M_e	Mach number at the edge of the boundary layer
n	Curvilinear coordinate normal to the aerofoil's surface $[m]$
N_p	Number of panels in the aerofoil surface
N_v	Number of vortex blobs

p	pressure $[Pa]$
R	Distance of a Point from the vortex blob centrer $[m]$
r	Radial coordinate $[m]$
R_c	Viscous core radius of vortex blob $[m]$
r_ε	Singolarity radius
R_{VAWT}	Radius of Vertical Axis Wind Turbine
Re	*Reynolds* number
Re_{rotor}	*Reynolds* number (rotor scale) $2R_{VAWT}u_\infty/\nu$
s	Curvilinear coordinate parallel to the aerofoil's surface $[m]$
$S(t)$	Time dependent control surface
t	Time $[s]$
u	Velocity in the absolute frame of reference $[m/s]$
$u_{i,bl}$	Velocity induced by the boundary layer in the wake $[m/s]$
$V(t)$	Time dependent control volume
w	Velocity in the frame of reference attached to the aerofoil $[m/s]$
$w_{transp.}$	Transpiration Velocity $[m/s]$
x, y, z	Cartesian coordinate system in the absolute frame of reference $[m]$

Subscripts, superscripts

$+, -$	Two side of a panel
$1, 2$	Refer to the separated and attached zone on the aerofoil
θ	Angular coordinate
a	Refer to the aerofoil
b	Boundary Layer
e	Edge velocity of the boundary layer

i	Refer to the $i-th$ panel in the aerofoil surface
n	Component in the n axis
n	Iteration step
p	Potential flow
r	Component in radial coordinate
s	Component in the s axis
sp	Refer to the separation position
v	Refer to the vortices in the wake
w	Refer to the panel in the trailing edge wake
x, y, z	Component in Cartesian coordinate

1

Introduction

In the present thesis a vortex panel method is presented for the numerical simulation of the flow field around the Darrieus Wind Turbine. This Vertical Axis Wind Turbine (introduced by G. Darrieus in 1931 [1]) was extensively studied during the 1980s by the Sandia National Laboratories and the National Research Council of Canada, till the Horizontal Axis Wind Turbine (HAWT hereafter) became the standard for the megawatt scale (for an historical overview see Gipe [2]). Therefore, the aerodynamic research was focused on the HAWT rotor whereas the research on the Vertical Axis Wind Turbine (VAWT hereafter) was discontinued and almost restricted to the improvement in the models developed during the eighties.

In the last years, the depletion of global fossil fuel reserves combined with mounting environmental concern has served to focus attention in alternative ways to capture the wind energy. The most promising solutions seem to be the diffuse generation in the urban environment and the offshore application, conditions where the Vertical Axis Wind Turbine has an ace in the hole.

In the building environment, where the flow is highly turbulent with strong vertical gradient, the VAWT represents an attractive choice for its insensitiveness to the yaw flow, for its structural strength to the rapid change in wind direction, for the low noise emission [3], for the good performance in the skewed flow [4] and for the better public acceptance (Fig 1.1).

In the offshore application, the VAWT strength is in the structural features, as the position of the generator and the auxiliary equipment in the bottom of the machine, the absence of the moving nacelle and the lower impact on the performance of the pitch and plunge motions of the floating platforms.

To resume, in the last years the interest in the VAWT is increased but, due to the aerodynamic complexity of the rotor and the sobbing research, a lot design problems are still present. In this thesis it will be presented a model that is able to predict the flow field past a VAWT, allowing a better understanding of the energy conversion process. In the following section a brief description of

S+ARCK
PRAMAC
GROUP

Figure 1.1: The VAWT as an object of design, by Philippe Starck

the wind turbines, with emphasis on the Darrieus VAWT, will be carried out.

1.1 Wind Energy

The wind is the air movement from high pressure to low pressure regions, due to the irregular solar exposition. The use of this "indirect solar energy" is one of the most promising renewable source that can reduce the countries dependence on fossil fuels. Nowadays, the most efficient way to extract energy from the wind is the use of a lifting-device as it may be the wind turbine (the drag wind turbines are not mentioned in the present thesis). The wind turbines are divided in two main categories, depending on the orientation of their rotational axis: the Horizontal Axis Wind Turbine (HAWT, Fig. 1.2(a)) and the Vertical Axis Wind Turbine (VAWT, Fig 1.2(b)). Both have about the same ideal efficiency, but the HAWTs are the most widespread and the most studied.

The HAWT has a propeller type rotor and its rotational axis is parallel to the wind direction (see Fig. 1.2(a)). When a steady flow hits the machine, constant lift forces (so a circulation) are generated on the rotating blades and the wind

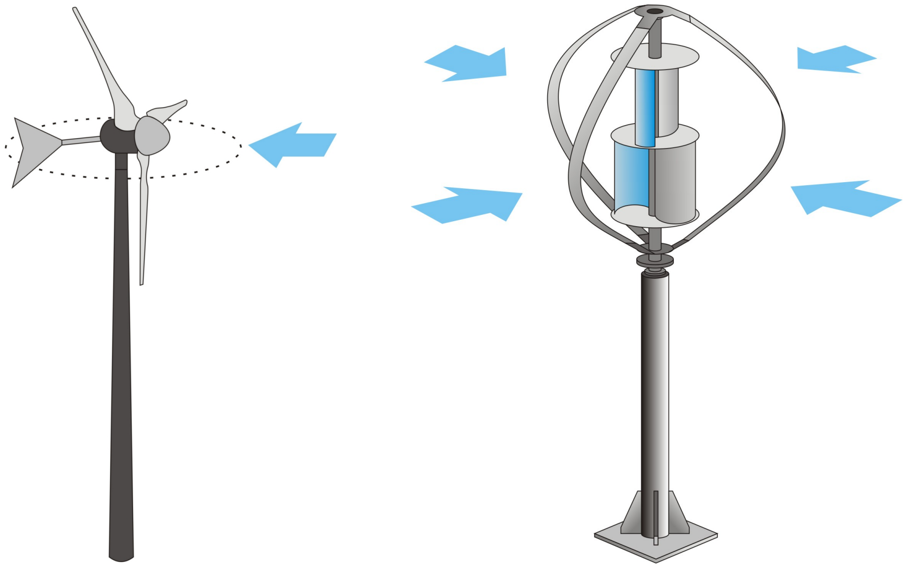

(a) HAWT (b) VAWT

Figure 1.2: Example of Horizontal Axis Wind Turbine (HAWT) and Verical Axis Wind Turbine (VAWT)

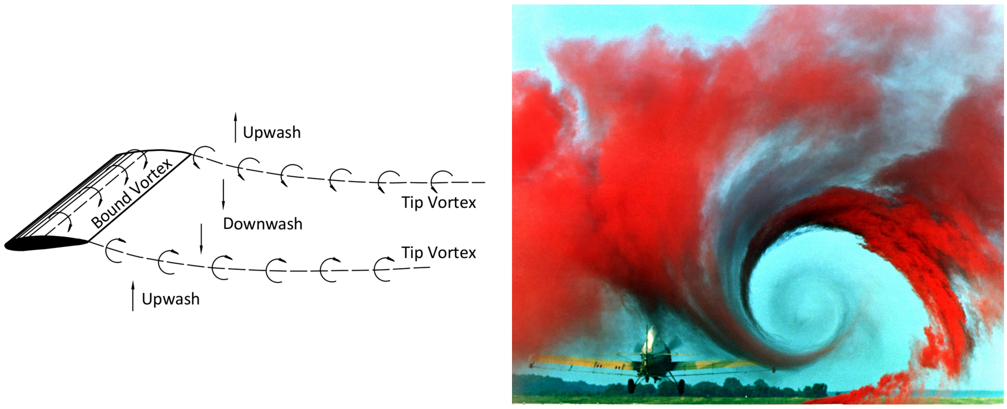

(a) Simplified vortex system in a wing (b) Visualization of the tip vortex

Figure 1.3: 3D Flow past a wing

energy is converted into electrical energy. In this condition, each annular section of the blade is characterised by a constant bound circulation and, from the Kelvin's theorem (see J. Katz and Plotkin [5]), no circulation is shed into the wake. Nevertheless, considering the 3D finite blade, its total bound circulation cannot end in the fluid and so it must be continued as trailing vorticity in the

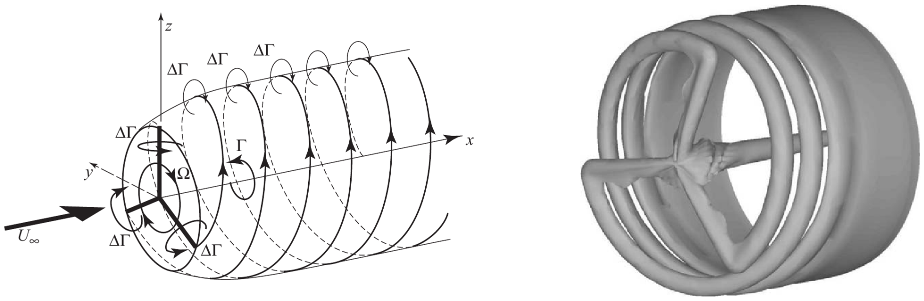

(a) Conceptual representation (b) Numerical simulation

Figure 1.4: Evolution of trailing vorticity in a HAWT wake. Conceptual representation from T. Burton et al. [6](a), numerical simulation from J.N. Sørensen et al. [7](b)

flow till, far downstream, it creates a closed path (Fig. 1.3, Helmholtz's second theorem, see J. Katz and Plotkin [5]). Therefore the HAWT wake (see e.g, Fig 1.4) is mainly composed of the trailing vorticity due to the finite span of the blade, which induces a tangential and an axial velocity to the machine.

The VAWT (see Fig. 1.2(b)) has a bladed rotor with rotation axis perpendicular to the wind direction and it can capture wind from any direction. When the machine is hit by a steady flow, the rotating blades are subjected to a variation in time of the angle of attack that produces unsteady lifting forces. In one transversal section of the machine, the blade rotation produces a variation in time of the bound circulation of the aerofoil and, according to the Kelvin's theorem, a circulation is shed into the wake. Therefore the VAWT wake is composed not only of the trailing vorticity (due to the finite blade span, as in the HAWT) but also of the shed vorticity due to the variation over the rotation of the blade bound circulation (see Fig. 1.5).

The energy conversion process in HAWTs and VAWTs is extremely different, as well as their wakes are. In both machines the wake carries all the information about the power exchange, and it influences the velocity field around the blade. In the HAWT, the strength of the wake is function of the bound circulation of the blade and its influence on the lifting forces can be easily evaluated and included in simple prediction models (e.g., in the blade element momentum model). The VAWT wake is always unsteady, due to the time varying aerofoil circulation, and it interacts with the blade especially in the downwind part of the rotation. That creates a very complex behaviour that cannot be easily modelled and included in the momentum models.

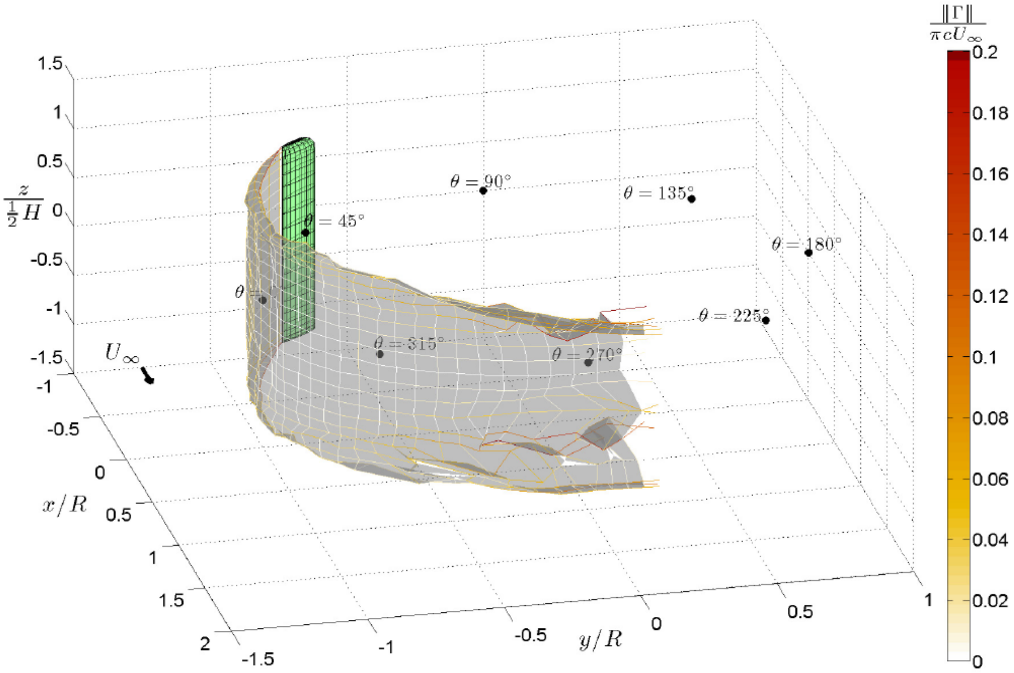

Figure 1.5: Wake of a single blade VAWT, Simão Ferreira [8]

1.2 2D VAWT aerodynamics

The aerodynamics of the VAWT is characterised by three-dimensional unsteady flow effects (i.e., tip vortex), by time varying induction and, when the tip-speed ratio λ is less than four and the reduced frequency $\kappa = \Omega L/2\lambda u_\infty$ is greater than 0.05, by dynamic stall (Hofmann et al. [9] and Simão Ferreira [8]).

The dynamic stall is an unsteady phenomenon that occurs when the angle of attack rapidly changes exceeding the static stall angle. When this happens, in the suction side of the aerofoil leading edge a dynamic vortex starts to develop although the flow keeps on reattaching behind the vortical structure. In this condition the main flow experiences an effective aerofoil shape that comprises the leading edge vortex, which causes an “overshoot” in the lift force due to the high virtual chamber of the aerofoil. When the strong vortical structure has grown enough it detaches from the aerofoil surface and is convected downstream by the main flow. Meanwhile, the aerofoil lift drops and a counter-rotating vortex develops at the trailing edge. After the first dynamic vortex has

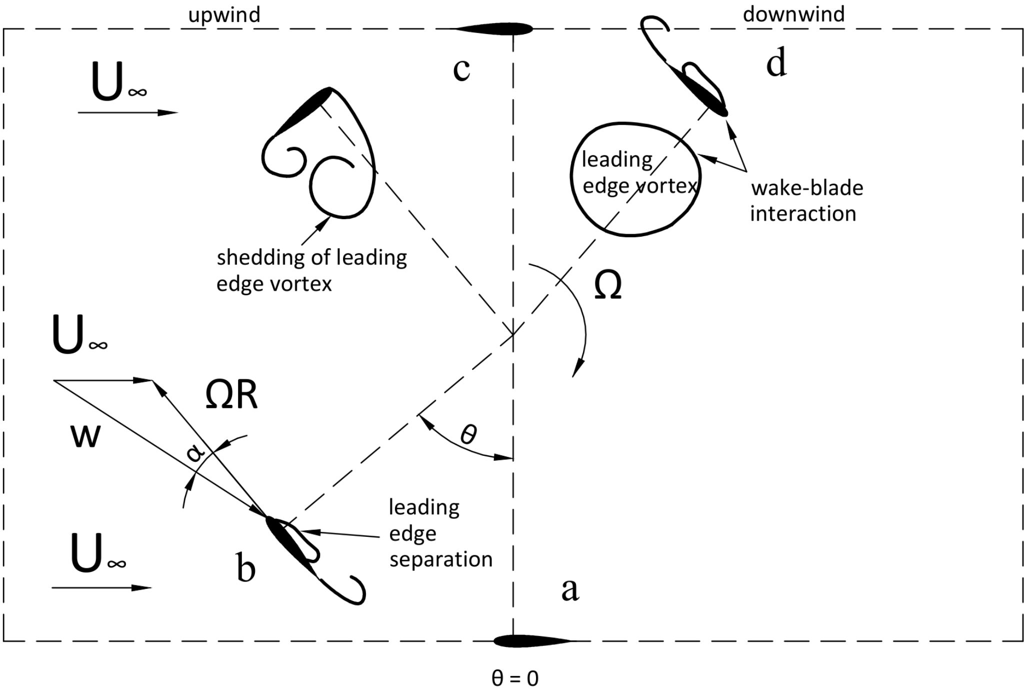

Figure 1.6: Schematic behaviour of a VAWT

been shed, weaker vortices form either on the leading edge or the trailing edge till a condition of normal stall is established.

The present thesis focuses on the 2D flow field where the dynamic stall and the time-dependent aerofoil bound circulation are the main features. In order to better understand the topic of this research, Fig. 1.6 shows a schematic description of the flow field around a single blade VAWT in deep dynamic stall ($\lambda < 4$, $\kappa > 0.05$). For $\theta = 0°$ the geometrical angle of attack is $\alpha = 0°$ and, excluding the influence of the wake, the lift on the aerofoil is zero and only drag is present. By increasing θ, the aerofoil bound circulation changes producing a release of vorticity in the wake (Kelvin theorem, see Katz and Plotkin [5]). If the tip-speed ratio, λ, is between 2 and 4, the angle of attack, α, increases over the static stall angle and flow separation occurs (point b, Fig. 1.6). The blade keeps to rotate and the leading edge vortex increases in size and strength. Before the first half of the rotation is completed the leading edge vortex is released and transported by the fluid downstream (point c, Fig. 1.6). In the leeward region, the suction side of the aerofoil becomes the pressure side and vice-versa. The remaining part of the rotation is characterised by a second stall (point d, Fig. 1.6) and the interaction between the aerofoil and the wake

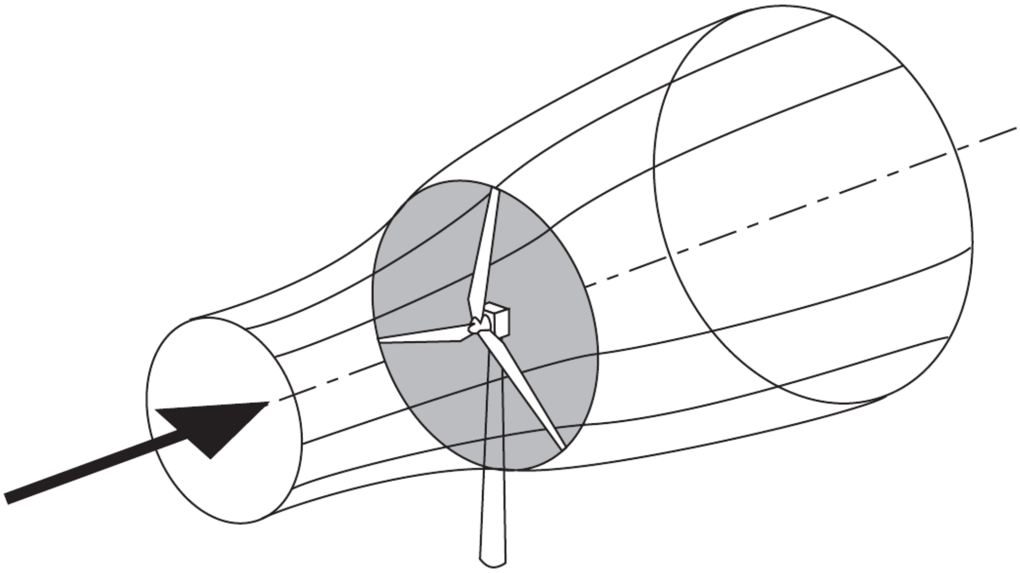

Figure 1.7: Expansion of the wake due to the energy extraction in a HAWT

that was shed in the upwind part of the rotor revolution.

From this brief description it should be clear that the 2D aerodynamics of a VAWT is unsteady with a strong wake-blade interaction.

1.3 Numerical methods for VAWT

1.3.1 Momentum models

The most common and used numerical methods for the analysis of the wind turbines are the momentum models based on the actuator disk concept (Glauert [10]). This approach has been developed for the simulation of the propellers, where the rotor is initially reduced into a 2D actuator surface (zero rotor thickness) and moreover, due to the axisymmetric flow, reduced into a 1D actuator strip.

The actuator disk concept can be used straightforward foe the HAWT simulation, where the streamtube (delimited by the streamlines that cross the blades tip) shows the flow expansion due to the energy extraction (see Fig. 1.7). The flow velocity, along the streamtube, slows down approaching the actuator disk where a pressure jump occurs to balance the force applied by the rotor. The difference between the kinetic energy far upstream and far downstream (where

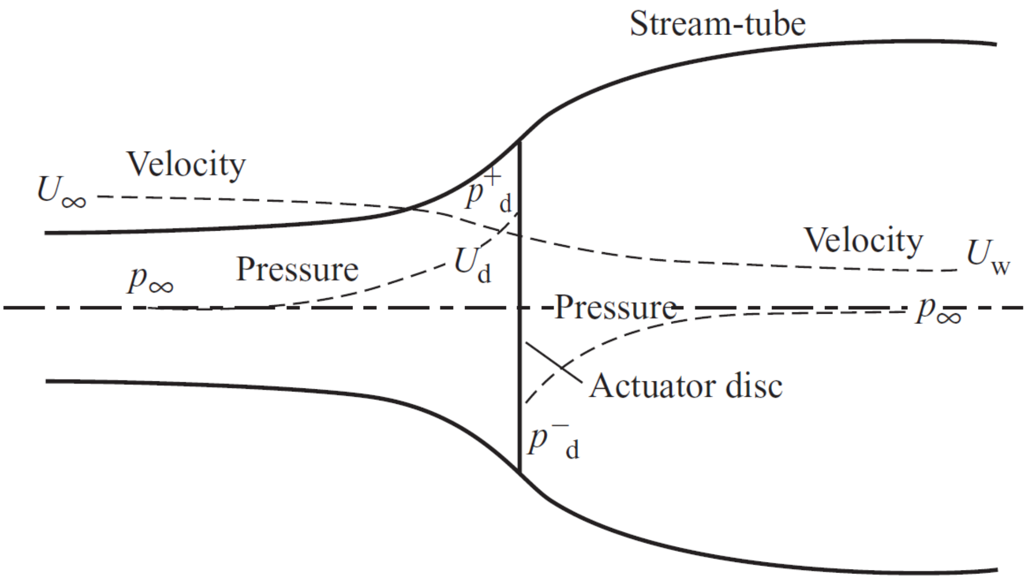

Figure 1.8: The actuator strip and the streamtube configuration for both HAWT and VAWT

the local pressure is equal to the freestream pressure) balances the work done by the flow on the rotor. This approach allows (by an energy balance) the loading on the rotor to be related to the energy exchange and the wake induction and expansion.

To increase the accuracy of this model, the effect of the finite blade span (Fig. 1.3) must be taken into account. The HAWT wake, as explained before, is usually composed of a strong trailing vorticity shed at the blade tip and root. This behaviour can be modelled by introducing a continuous vorticity distribution along the streamline that crosses the blade tip in the actuator disk model (Fig. 1.8, for more details see Burton et al. [6]).

This simple model has shown a great ability in the prediction of HAWT performance and therefore it was applied (with some adjustments) to the 2D VAWT flow field (see, e.g., Wilson et al. [11]). When the actuator disk approach is applied to a 2D VAWT (in a plane normal to the rotation axis, Fig. 1.6) the circular rotor is pressed into a line perpendicular to the flow, that becomes the actuator strip of the model (Fig. 1.8). The continuous shedding of vorticity during the blade rotation (as mentioned in sec. 1.2) is simplified assuming that all vorticity is shed at $\theta = 0°$ and $\theta = 180°$. Thus, the 2D wake is modelled by introducing a continuous vorticity distribution along the streamlines that cross the actuator strip ends.

To increase the accuracy of this model, the effect of the finite blade span should be taken into account. In the literature some formulations are reported (e.g., Paraschivoiu [12]), that introduce a tip-effect correction to the load, in a similar way to what is done for the HAWT.

From the above brief description of the momentum based models, it should be clear that they introduce rather drastic assumptions, especially as far as the position and distribution of the shed vorticity are concerned. These simplifications are reasonable for the HAWT (axisymmetric flow, zero thickness of the rotor, vorticity shed only at the blade tip, etc.) but they are not appropriate for the VAWT [8]. For example, if the continuous shedding of vorticity during the blade rotation, which is peculiar of the VAWT, is replaced by a vorticity shedding at $\theta = 0°$ and $\theta = 180°$, the model can still provide a good prediction of the rotor loading, but no information about the most important part of the energy conversion process can be expected. In other words, the momentum based models, due to their formulation, are not able to reproduce the physics of the energy conversion process, therefore they cannot provide any help in understanding it. An exhaustive description of the intrinsic limitations of the VAWT momentum models can be found in Simão Ferreira [8] or, more concise, in Strickland et al. [13] and Zanne L. [14].

According to [8], the momentum models (e.g., multiple streamtube model) are believed to be at the end of their life. Nowadays, due to the increase of the computer capabilities, the vortex methods could face many problems, the solution of which is “hopeless” [13] by using the momentum models.

However, the models based on the momentum balance are still the most widespread tools for VAWT design and development, due to their simplicity, flexibility, low computational cost (essential for aerolastic code) and to a number of formulations in the literature that include the effects of dynamic stall, tip losses, wake expansion, etc.

1.3.2 Vortex Methods

Nowadays, the vortex methods (VM) represent one of the most promising tools for the study and design of VAWTs [8]. The VMs are numerical methods based on the vorticity equation, in which pressure does not appear explicitly pressure field values are not needed to determine the velocity field [12]. They are grid free, the mesh being required only on the solid surfaces and in the rotational flow regions such as the wake. These methods do not introduce numerical dissipation, which is fundamental in wind turbine applications. In the VMs the flow field past the blade is considered incompressible and irrotational, whereas the rotational wake region, formed by the shed vorticity, is discretized by a collection of singularities (point vortices) that carry away all the circulation released from the blade due to the energy exchange process.

One of the first attempt to use the vortex methods was made by Strickland et al. [13] in the 1980s. Their "free vortex wake method" was applied to simulate the complex unsteady wake past a VAWT, so overcoming some intrinsic limitations of the momentum models. The main weakness of that approach is in the computation of the forces acting on the blade, based on an aerofoil section data, which only accounts for the perceived angle of attack and the velocity in a single point of the flow field. Therefore, this methods (as the one of [14]) can be considered as an evolution of the momentum models and, although the influence of the wake is better captured, it appears to be not yet complete. Moreover, some corrections are necessary to take into account the flow unsteadiness and the dynamic stall, since the forces are obtained from steady aerofoil section data.

To remove the use of aerofoil section data and the empirical correction for the dynamic stall, Oler et al. [15] developed the first vortex panel method capable of modelling the physics of the dynamic stall in a VAWT by using the "double wake " concept. However, this method was abandoned in favour of the momentum models, which were much faster and accurate enough in the rotor loading prediction.

In the last years, due to the increase of the computer capabilities, the vortex models are becoming more and more popular. A recent comparison between a momentum model (the Double Multiple Streamtube, DMST) and a 2D inviscid unsteady panel code is presented in Simão Ferreira [8]. In his Ph.D. thesis he shows that only the panel method is capable of reproducing the complex behaviour of the VAWT wake but, due to the hypothesis of inviscid attached flow (the stall or the dynamic stall are not captured), it cannot be used for design purposes.

In the present thesis, a step forward in the development of an unsteady panel method for VAWT is taken, removing the hypothesis of attached flow condition and introducing the effects of the boundary layer on the pressure distribution on the aerofoil surface.

1.3.3 Computational Fluid Dynamics

The complex unsteady aerodynamics of the VAWT, especially during the dynamic stall, makes the simulation by Computational Fluid Dynamics (CFD) models a challenging matter. As described in sec. 1.2, the 2D aerodynamics of

VAWT in dynamic stall is characterised by the formation, growth and release of the leading and trailing edge vortices, which interact with the blade especially during the downwind passage. The simulation of this behaviour by means of CFD models requires a very fine computational grid throughout the VAWT rotor and not only near the aerofoil surface (it is necessary even though the dynamic stall is not present). This requirement, combined with the need of time-accurate models and the absence of spatial simplification (e.g, plane of symmetry), makes the computational cost of the VAWT simulation almost prohibitive for a widespread study of the machine. A recent comparison between the simulation of VAWT in dynamic stall performed by URANS ($S-A$ and $\kappa-\epsilon$ model), LES and DES models, is presented in Simão Ferreira et al. [16]. The DES model seems to be the only one capable of properly predicting the generation, shedding and convection of the trailing and leading edge vortices, against a high computational cost.

1.4 Motivation of the research project

One of the main features of the Vertical Axis Wind Turbine is the complex wake that develops during the extraction of energy from the wind. However, the generation of the wake of the VAWT and its impact on the energy conversion process is still not fully understood, especially during operation in dynamic stall.

The aim of the present research is to deepen the knowledge of the relation between the wake structure and the rotor loading, starting from the analysis of the dynamic stall and its influence on the generation and evolution of the wake and the induced velocity field in the two-dimensional flow case.

To achieve that purpose, an unsteady two-dimensional panel model coupled with the boundary layer equations has been developed, which is able to model the physics of the dynamic stall by using the "double wake" concept (Riziotis et al. [17]). In order to demonstrate the capabilities of the model the results are compared at first with experimental data for pitching aerofoils at medium-high *Reynolds* number (from [18]) and medium-low *Reynolds* number (time resolved PIV data, collected by the author at the Delft University of Technology). Subsequently, the model predictions are compared with PIV measurements and CFD simulations of a VAWT (from Simão Ferreira et al.[19], [16]).

The simulation results allow the characterisation of the dynamic stall in the aerofoil scale and in the rotor/wake scale. The first one is very important in the upwind stage (see Fig. 1.6), where the stall mainly affects the pressure distribution on the blade, so reducing the lift and, consequently, the turbine performance. In the rotor/wake scale the dynamic stall modifies the vorticity

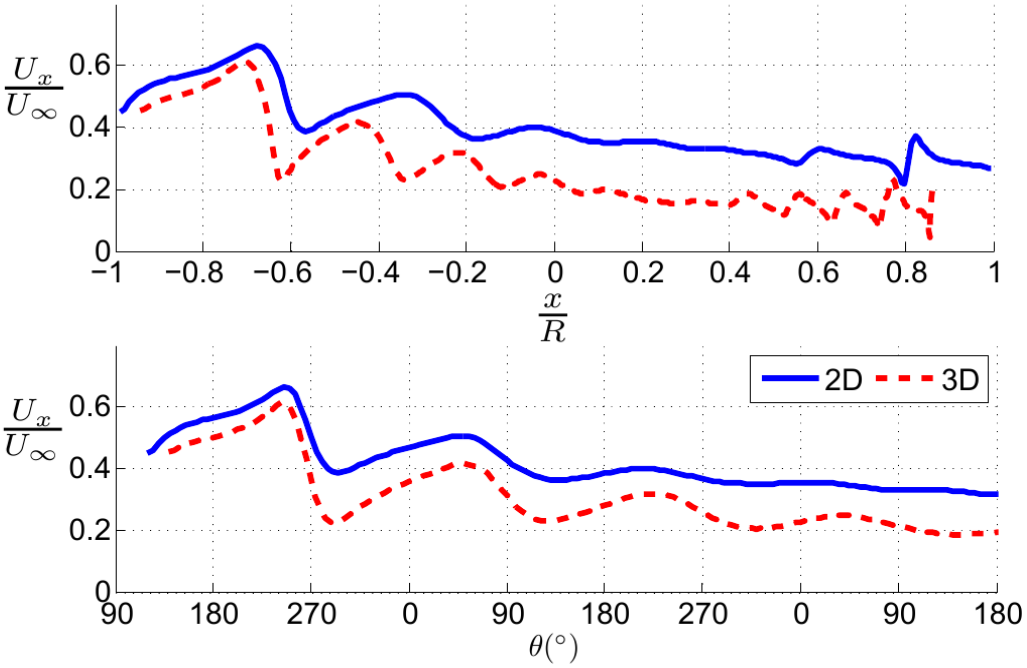

Figure 1.9: Evolution of the velocity in the freestream direction (U_x) in the midspan plane of a VAWT compared with the results of a 2D simulation [8]

.

distribution in the wake, which, especially in the downwind stage, introduces a strong wake-blade interaction.

1.5 2D flow assumption

The model developed in the present thesis is based on the assumption of a two-dimensional flow, as well as the momentum models. Where the effects of the finite blade span need to be considered (as in the loading simulation of a real VAWT), it is possible to use an approach equivalent to the Prandtl's tip-loss function [20] and the Prandtl's finite-wing theory developed for the momentum models [12].

However, as pointed out in [8], those approaches are aimed at applying tip-effect corrections to the loading, dismissing the real physics of the flow. Therefore, in order to avoid "non-physical" and empirical corrections, at present they are not implemented in the model.

An interesting study on the 3D effects in the midspan plane of a VAWT is carried out in [8] and it can be useful to understand the limitations of the 2D

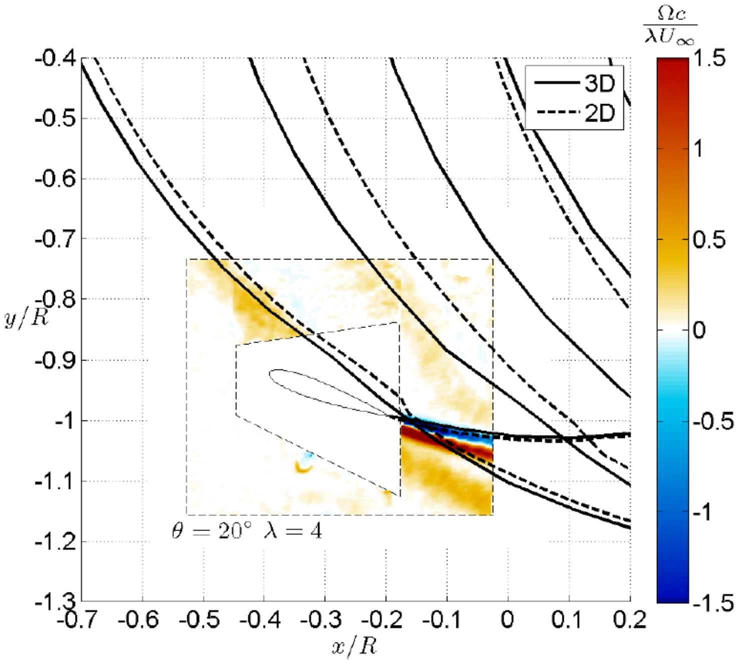

Figure 1.10: Wake path in the midplane of a VAWT. Comparison between 2D and 3D simulations [8]

flow assumption made in the present thesis. When a 2D simulation is compared with the 3D solution in a midspan plane of a VAWT the main difference seems to be a reduction of the wake convection velocity in the mainstream direction, especially in the downwind passage (Fig. 1.9). The lower convection speed of the 3D wake corresponds to that of a 2D wake at a higher tip-speed ratio [8]. Furthermore, Fig. 1.10 shows that the structure of the wake in the midspan plane of the 3D VAWT is similar to the one of the 2D VAWT. Therefore it seems reasonable to assume 2D flow in a plane far from the blade tips in order to study the physics of the energy conversion process.

1.6 Previous works

The vortex methods for the simulation of VAWTs were introduced to overcame some intrinsic weaknesses of the momentum models. The first model (free vortex wake method) can be considered as an evolution of the momentum models, where the wake is modelled as a collection of vortex blobs but the forces acting on the aerofoil are derived from the aerofoil section data (as

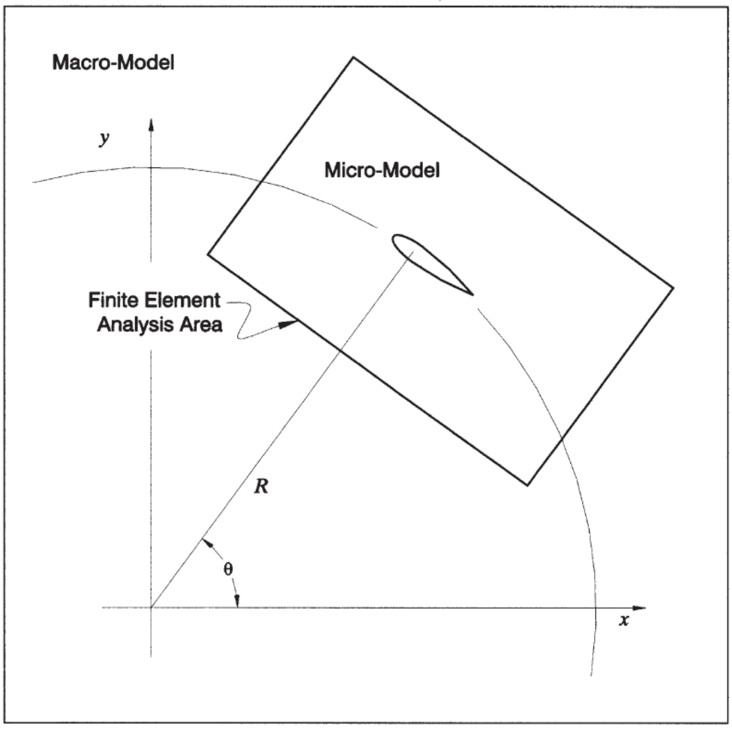

Figure 1.11: Example of ibrid model, vortex method in the Macro-Model and finite element method in the Micro-Model [21]

in the momentum models). This “ibrid” solution can increase the accuracy in the evaluation of the wake influence, but it still misses part of the physics of the energy conversion process and it needs some empirical relations to handle the dynamic stall. Examples of this model can be found in Strickland et al. [13], McIntosh S.C. et al. [22], Coton [23] and Zanne L. [14]. Another ibrid model is the FEVDTM presented in Ponta et al. [21], where the wake is still modelled by the vortex method but a finite element analysis is used in the flow surrounding the blades (Fig. 1.11).

The first vortex panel method for VAWT capable of modelling the physics of the dynamic stall (by using the “double wake ” concept) without the use of the aerofoil section data and empirical corrections for the dynamic stall, was presented by Oler et al. [15]. However, this convincing method was penalised by a computational cost that was too high in the eighties and by inadequate boundary layer closure relationships, an erroneous coupling of the boundary layer and the potential flow equations, and the use of not optimal boundary conditions.

Nowadays, due to the increase of available experimental data and computational capabilities, the vortex panel method for VAWT in dynamic stall can be revisited. Recently, Riziotis et al. [17] presented a vortex panel method coupled with the boundary layer equations that was able to model the dynamic stall of pitching aerofoils at medium-high *Reynolds* number. The model developed in the present thesis can be considered as an extension of the model in [17] to rotating multi-aerofoils (VAWT) at medium-low *Reynolds* number. Taking advantage of the progress made during the last three decades, the present model is capable of solving the problems that penalised the model of Oler et al. [15], providing an accurate approach to the study of the complex VAWT flow field.

The good accuracy of the present model (comparable to the one of the more complex CFD DES, sec. 5.1) and its reasonable computational cost make its use attractive in the VAWT design and in aerolastic codes.

1.7 Thesis outline

After this brief introduction, in Chapter 2 the mathematical formulation of the model is derived, while in Chapter 3 the algorithm and the separation criterion are described. In Chapter 4 the validation of the code by means of available experimental data is carried out. Also, the time resolved PIV data collected by the author are presented. In Chapter 5 the present code is used to analyse the influence of the dynamic stall on VAWT performance and in Chapter 6 the conclusions and the recommendations for future research works are provided.

2

Formulation of the Model

The aim of this research is to deepen the knowledge of the relation between the structure of the wake and the loading on the rotor of a VAWT, starting from the analysis of dynamic stall and its influence on the generation and evolution of the wake and the induced velocity field in the two-dimensional case. To achieve that purpose, an unsteady two dimensional panel method coupled with the boundary layer equations is developed, which is able to model the physics of dynamic stall by using the "double wake" concept (Riziotis et al. [17]).

In the field of aerodynamics, the fluid motion is governed by the continuity and Navier-Stokes equations. Under the assumptions of constant viscosity μ and incompressible flow, these equations can be written as:

$$Continuity \Rightarrow \nabla \cdot \bar{u} = 0 \tag{2.1}$$

$$N/S \Rightarrow \frac{\partial \bar{u}}{\partial t} + \bar{u} \cdot \nabla \bar{u} = \bar{f} - \frac{\nabla p}{\rho} + \nu \nabla^2 \bar{u} \tag{2.2}$$

The simultaneous solution of these three scalar equations is sufficient to determine the velocity and pressure fields. However, their solution in wind turbines practical applications needs a very large computational time, due to the non-linearity of the Navier-Stokes equations. To reduce the computational effort, a dimensional analysis of these equations makes it possible to identify the terms that can be neglected in certain flow regions, while the essential physics of the flow field can still be captured. An example is the model developed in the present thesis, based on the assumption that an incompressible external flow over an aerofoil for high *Reynolds* numbers can be split in two regions (Prandtl's boundary layer theory, Fig. 2.1):

The outer flow, where the viscous effects are negligible and the Navier-Stokes equations reduce to the Euler equations (with body forces neglected):

$$\frac{\partial \bar{u}}{\partial t} + \bar{u} \cdot \nabla \bar{u} = -\frac{\nabla p}{\rho} \tag{2.3}$$

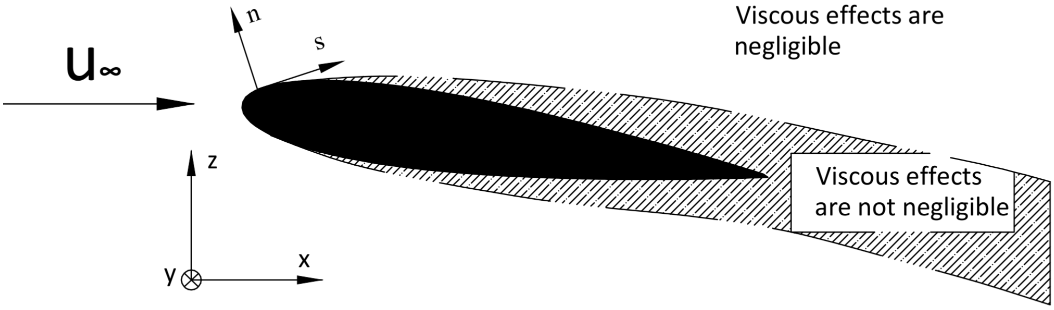
U∞
n
s
Viscous effects are negligible
z
Viscous effects are not negligible
y
x

Figure 2.1: Flow regions for high *Reynolds* numbers

The thin boundary layer, where the viscous effects cannot be neglected and the Navier-Stokes equations reduce in the classical boundary layer equations (see Schlichting [24])

$$\begin{aligned}(s) &\Rightarrow \rho\left(u_s\frac{\partial u_s}{\partial s}+u_n\frac{\partial u_s}{\partial n}\right)=-\frac{\partial p}{\partial s}+\mu\frac{\partial^2 u_s}{\partial^2 n}\\ (n) &\Rightarrow 0=-\frac{\partial p}{\partial n}\end{aligned}\tag{2.4}$$

where s represents the curvilinear coordinate along the body surface and n is the coordinate normal to it.

To complete the set of equations the continuity equation (2.1) is needed. This splitting allows to use the mathematical properties of the simplified equations to reduce noticeably the computational effort (e.g., in the inviscid region the mesh is necessary only on the aerofoil and wake surface and in the viscous zone the integral formulation of the boundary layer equations can be used).

In this chapter the governing equations for the two flow regions and the algorithm used to couple the viscous and the inviscid flow field will be described.

2.1 Potential flow equations and panel method

The vortex panel methods are based on the hypothesis that the flow surrounding the aerofoil and its wake is incompressible, inviscid and irrotational. Under these assumptions, the flow is governed by its kinematics and only the continuity equation together with the irrotationality requirement are needed to compute the velocity field. The equations of the flow dynamics (the Euler equations) can be used afterwards to compute the pressure distribution. After

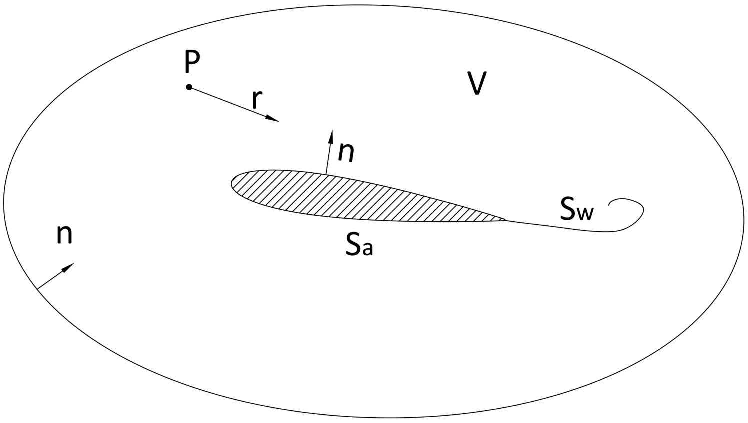

Figure 2.2: Control Volume for the application of the divergence theorem

these considerations, from a physical point of view, there is no way that an inviscid flow can apply a force on a solid body, so an extra-condition to simulate the main effects of the viscosity is needed. It is the “Kutta condition”, which will be described and derived in section (2.1.3).

Assuming incompressible, inviscid and irrotational flow, a velocity potential ϕ can be defined, and continuity equation (2.1) becomes:

$$\nabla \cdot \bar{u} = \nabla \cdot (\nabla \phi) = \nabla^2 \phi = 0 \tag{2.5}$$

which is the Laplace equation. From Katz and Plotkin [5] it is known that the solution of the Laplace equation can be obtained by the distribution of elementary solutions (e.g. point source, doublet or vorticity) on the aerofoil surface and wake. The proof rests on the divergence theorem:

$$\int_V \nabla \cdot \bar{\xi} \; dV = - \int_S \bar{n} \cdot \bar{\xi} \; dS \tag{2.6}$$

Here V is the control volume, $\bar{\xi}$ is a continuous function of position inside V, S is the boundary of V and $\bar{n}$ is a unit vector normal to S and directed into V (see Fig.. 2.2). The vector $\bar{\xi}$ is defined by:

$$\bar{\xi} = \phi \nabla \phi_s - \phi_s \nabla \phi \tag{2.7}$$

where ϕ is the flow velocity potential in V, whereas ϕ_s is the potential of a 2-D source of unit strength at some arbitrary point P in V (for more details see [25]), defined as:

$$\phi_s = \frac{1}{2\pi} ln \; r \tag{2.8}$$

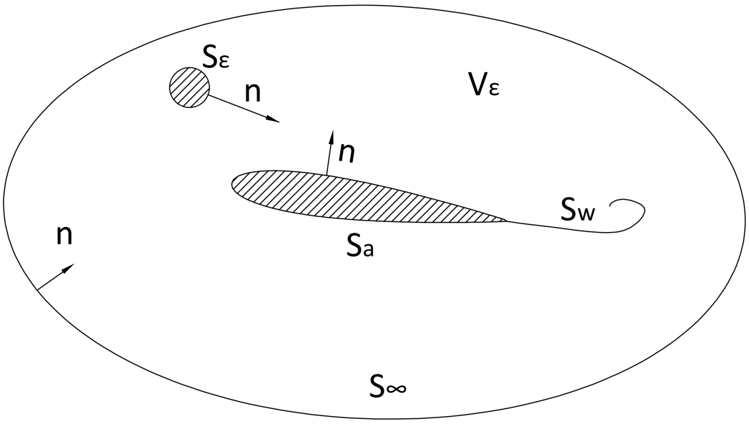

Figure 2.3: Nomenclature for derivation of Green's identity

where r is the distance from P to the point at which $\bar{\xi}$ is to be evaluated, as shown in Fig. 2.2. If function $\bar{\xi}$ is to be continuous in V, so must be ϕ, $\nabla\phi$, ϕ_s and $\nabla\phi_s$. But ϕ_s and its derivatives do not exist at P. Therefore, a small circle of radius r_ε centered at P should be carved out (see Fig. 2.3). Let V_ε be the part of V outside that circle and S_ε the surface of the circle. Now, the source potential ϕ_s satisfies the Laplace equation everywhere in V_ε, just as ϕ does. Therefore, the divergence of vector $\bar{\xi}$ is:

$$\nabla \cdot \bar{\xi} = \phi\nabla^2\phi_s - \phi_s\nabla^2\phi = 0 \tag{2.9}$$

Thus, applying equation (2.6) to region V_ε gives:

$$\int_{V_\varepsilon} \nabla \cdot \bar{\xi}\ dV = 0 = -\int_{S+S_\varepsilon} \bar{n} \cdot (\phi\nabla\phi_s - \phi_s\nabla\phi)\ dS \tag{2.10}$$

It is convenient to separate the integrals over two surfaces S and S_ε and to rewrite eq. (2.10) as:

$$\int_{S_\varepsilon} \bar{n} \cdot (\phi\nabla\phi_s - \phi_s\nabla\phi)\ dS = -\int_{S} \bar{n} \cdot (\phi\nabla\phi_s - \phi_s\nabla\phi)\ dS \tag{2.11}$$

When $\varepsilon \to 0$, ϕ and $\nabla\phi$ approach their values at P (ϕ_p and $\bar{u}_p$), so the left-hand side of equation 2.11 becomes:

$$\int_{S_\varepsilon} \bar{n} \cdot (\phi\nabla\phi_s - \phi_s\nabla\phi)\ dS \approx \phi_p \int_{S_\varepsilon} \bar{n} \cdot \nabla\phi_s\ dS - \bar{u}_p \cdot \int_{S_\varepsilon} \bar{n}\phi_s\ dS \tag{2.12}$$

The first integral on the right is the volume flow rate through S_ε, which is equal to the strength of the source inside the circle (equal to one by definition, Eq.

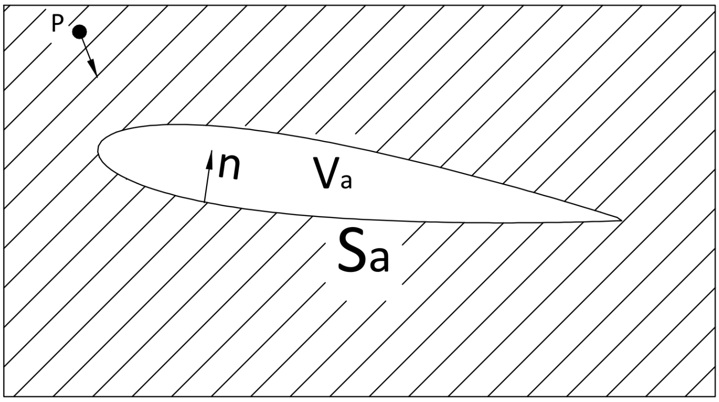

Figure 2.4: Definition of potential inside aerofoil

2.8). In the second integral, ϕ_s is constant on S_ε, so that integral reduces to:

$$\int_{S_\varepsilon} \bar{n}\ dS \tag{2.13}$$

which is zero. So equation (2.11) becomes, in the limit, the *Green's identity*:

$$\phi_p = \int_S [(\bar{n}\cdot\nabla\phi)\phi_s - \phi(\bar{n}\cdot\nabla\phi_s)]\ dS \tag{2.14}$$

This formula gives the value of ϕ at any point P in V, where ϕ satisfies the Laplace equation in terms of the values of ϕ and $\bar{n}\cdot\nabla\phi$ on the boundary of V. At this point the integral over S is separated out into an integral over S_∞, far from any body in the flow field, and an integral over S_a and S_w (see Fig. 2.3). On S_∞:

$$\phi_\infty \approx u_{x\infty}x + u_{z\infty}z \tag{2.15}$$

and eq. (2.14) becomes:

$$\phi_p = \phi_\infty + \int_{S_a+S_w} [(\bar{n}\cdot\nabla\phi)\phi_s - \phi(\bar{n}\cdot\nabla\phi_s)]\ dS \tag{2.16}$$

A new potential ϕ^* is introduced as a solution of the Laplace equation in region V_a that is inside the body surface S_a (see Fig. 2.4). In a point P outside the body surface:

$$\bar{\xi}^* \equiv \phi^*\nabla\phi_s - \phi_s\nabla\phi^*. \tag{2.17}$$

Then, as it was found in eq.(2.9),

$$\nabla\cdot\bar{\xi}^* = 0 \tag{2.18}$$

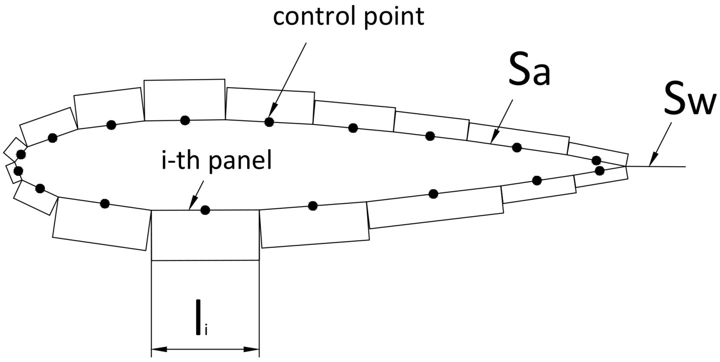

Figure 2.5: Definition of panels

and, from eq.(2.6),

$$0 = \int_{S_a} \bar{n}^* \cdot (\phi^* \nabla \phi_s - \phi_s \nabla \phi^*) dS \tag{2.19}$$

Adding eq.(2.16) and eq.(2.19) leads to:

$$\phi_p = \phi_\infty + \int_{S_a+S_w} (\sigma \phi_s - \chi \bar{n} \cdot \nabla \phi_s) \; dS \tag{2.20}$$

where:

$$\begin{aligned} \sigma &\equiv \bar{n} \cdot \nabla(\phi - \phi^*) && \textit{Strength of a Source} \\ \chi &\equiv \phi - \phi^* && \textit{Strength of a Doublet} \end{aligned} \tag{2.21}$$

At this point surfaces S_a and S_w are divided into a number N_p of straight lines that become the panels of the method, as shown in Fig. 2.5. The sources and the doublets are distributed on the straight-line panels, so that the potential in point P becomes:

$$\phi_p = \phi_\infty + \sum_{j=1}^{N_p} \int_{panel\ j} (\sigma \phi_s - \chi \bar{n} \cdot \nabla \phi_s) \; dS \tag{2.22}$$

or, after integration on each panel:

$$\phi_p = \phi_\infty + \sum_{j=1}^{N_p} (\phi_{\sigma,j} + \phi_{\chi,j}) \tag{2.23}$$

From Katz and Plotkin [5] it is known that the potential induced by a doublet distribution can be expressed as induced by a vortex distribution, so eq.(2.23)

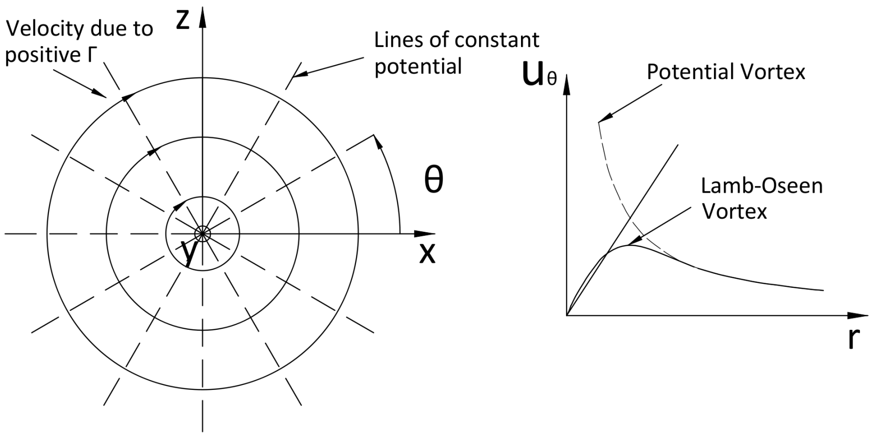

Figure 2.6: Point vortex

can be rewritten as:

$$\phi_p = \phi_\infty + \sum_{j=1}^{N_p} (\phi_{\sigma,j} + \phi_{\gamma,j}) \tag{2.24}$$

and using the definition of velocity potential:

$$\begin{aligned} \nabla\phi_p = \bar{u}_p =& \nabla\phi_\infty + \sum_{j=1}^{N_p} \nabla(\phi_{\sigma,j} + \phi_{\gamma,j}) \\ =& \bar{u}_\infty + \sum_{j=1}^{N_p} (\bar{u}_{j,\sigma} + \bar{u}_{j,\gamma}) \end{aligned} \tag{2.25}$$

In this way the velocity in each point of the flow field is expressed as the sum of the "velocity induced" by source and vortex panels on the boundary. To conclude, the *Green's identity* allows the Laplace equation to be solved by distributing elementary solutions (or singularities) on the boundaries (aerofoil surface and wake). The strength of these singularities can be obtained by applying the boundary conditions.

In the present model three different singularities are used. The panel with constant - strength source and the panel with a constant - strength vortex distribution on the aerofoil surface and in the near wake. In the far wake, the vortex panel is changed into a vortex blob.

Vortex Blobs This elementary solution has only a tangential velocity component, as shown in Fig. 2.6. So, in polar coordinates:

$$\begin{aligned} u_r &= 0 \\ u_\theta &= u_\theta(r, \theta) \end{aligned}$$

From the continuity equation:

$$\frac{\partial u_r}{\partial r} + \frac{1}{r}\frac{\partial u_\theta}{\partial \theta} + \frac{u_r}{r} = 0$$

u_θ turns out to be only a function of r. By applying the definition of vorticity and the requirement of irrotational flow:

$$\omega_y = -\frac{1}{r}\left[\frac{\partial}{\partial r}(r u_\theta) - \frac{\partial}{\partial \theta}(u_r)\right] = 0 \Rightarrow r u_\theta = const = K \tag{2.26}$$

where K can be computed by using the definition of circulation (according to right-hand rule):

$$\Gamma = \oint_l \bar{u} \cdot d\bar{l} = \int_{2\pi}^{0} u_\theta \cdot r d\theta = -2\pi K \tag{2.27}$$

Therefore, the velocity field induced by a point vortex of strength Γ is given by:

$$\begin{aligned} u_r &= 0 \\ u_\theta &= -\frac{\Gamma}{2\pi r} \end{aligned} \tag{2.28}$$

In Cartesian coordinate (x, z), the velocity induced at point $P(x, z)$ by vortex in (x_0, z_0) is:

$$\begin{aligned} u_x &= \frac{\Gamma}{2\pi}\frac{z - z_0}{(x - x_0)^2 + (z - z_0)^2} \\ u_z &= \frac{-\Gamma}{2\pi}\frac{x - x_0}{(x - x_0)^2 + (z - z_0)^2} \end{aligned} \tag{2.29}$$

It is useful to introduce a vector notation for the velocity induced by a point vortex:

$$\begin{aligned} \bar{u} &= \Gamma \bar{D} \\ \bar{D} &= \begin{bmatrix} \frac{1}{2\pi}\frac{z-z_0}{(x-x_0)^2+(z-z_0)^2} \\ -\frac{1}{2\pi}\frac{x-x_0}{(x-x_0)^2+(z-z_0)^2} \end{bmatrix} \end{aligned} \tag{2.30}$$

The requirement of potential flow constraints all the vorticity in an infinitesimal part of the vortex centre, which induce a singularity in the

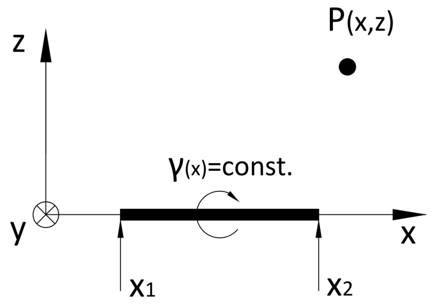

Figure 2.7: Constant Strength vortex distribution

velocity that is unacceptable on the physical ground. To remove this singularity and to mimic the real flow a viscous core is used and the Lamb - Oseen vortex model has been chosen:

$$\bar{D} = \begin{bmatrix} \frac{1}{2\pi}\frac{z-z_0}{R^2}(1-e^{(-R^2/R_C^2)}) \\ -\frac{1}{2\pi}\frac{x-x_0}{R^2}(1-e^{(-R^2/R_C^2)}) \end{bmatrix} \tag{2.31}$$

Where $R^2 = (x-x_0)^2 + (z-z_0)^2$ and R_C is the viscous core radius ($\propto \sqrt{4\nu t}$). Anyway, in the present model, the core spreading due to the diffusion is not considered as relevant for wind turbines applications, so the core size is kept constant.

Constant-Strength Vortex distribution : it is a vortex distribution along the x axis (see Fig. 2.7) where the strength per unit length, γ, is constant on the panel. The velocity induced by this distribution at a point $P(x,z)$ is an integral of the influence of the point vortex (see [5]):

$$\begin{aligned} u_x &= \frac{\gamma}{2\pi}\int_{x_1}^{x_2}\frac{z}{(x-x_0)^2+z^2}dx_0 \\ u_z &= -\frac{\gamma}{2\pi}\int_{x_1}^{x_2}\frac{x-x_0}{(x-x_0)^2+z^2}dx_0 \end{aligned} \tag{2.32}$$

Where the circulation on a line around the panel is:

$$\Gamma = \gamma(x_2 - x_1) \tag{2.33}$$

and in vector notation:

$$\bar{u} = \gamma\bar{B}$$
$$\bar{B} = \begin{bmatrix} \frac{1}{2\pi}\int_{x_1}^{x_2}\frac{z}{(x-x_0)^2+z^2}dx_0 \\ -\frac{1}{2\pi}\int_{x_1}^{x_2}\frac{x-x_0}{(x-x_0)^2+z^2}dx_0 \end{bmatrix} \tag{2.34}$$

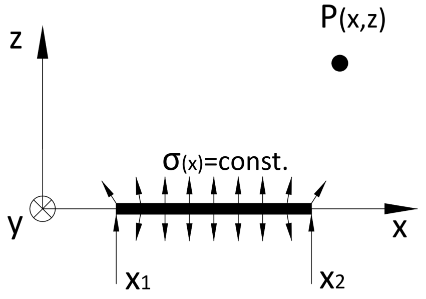

Figure 2.8: Constant Strength source distribution

Constant-Strength source distribution : it is a source distribution along the x axis (Fig. 2.8) where the strength per unit length, σ, is constant on the panel. The velocity induced in $P(x,z)$ is an integral of the influence of the point source (see [5]):

$$\begin{aligned} u_x &= \frac{\sigma}{2\pi}\int_{x_1}^{x_2}\frac{x-x_0}{(x-x_0)^2+z^2}dx_0 \\ u_z &= \frac{\sigma}{2\pi}\int_{x_1}^{x_2}\frac{z}{(x-x_0)^2+z^2}dx_0 \end{aligned} \tag{2.35}$$

As usual, in vector notation

$$\begin{aligned} \bar{u} &= \sigma\bar{A} \\ \bar{A} &= \begin{bmatrix} \frac{1}{2\pi}\int_{x_1}^{x_2}\frac{x-x_0}{(x-x_0)^2+z^2}dx_0 \\ \frac{1}{2\pi}\int_{x_1}^{x_2}\frac{z}{(x-x_0)^2+z^2}dx_0 \end{bmatrix} \end{aligned} \tag{2.36}$$

2.1.1 Attached Flow

To simplify the description without loss of generality, the system of equations for one aerofoil will be presented. In multi - aerofoils problems the difference is in the calculation of the velocities, where a velocity induced by the other aerofoils and their wakes appears. In unsteady attached flow condition the surface of the aerofoil is divided in N_p panels with source distribution of strength σ_i and a vorticity distribution of strength γ (Fig. 2.9). The wake is defined by a collection of vortex blobs, except for the part close to the trailing edge that is discretized by a vortex segment of length l_w and strength γ_w. Its position, following Basu et al. [26] and Riziotis et al. [17], should be parallel to the upper or lower surface at the trailing edge, depending on the sign of the aerofoil circulation. But this formulation has a weakness when $\partial\Gamma_{aerofoil}/\partial t \rightarrow 0$ because

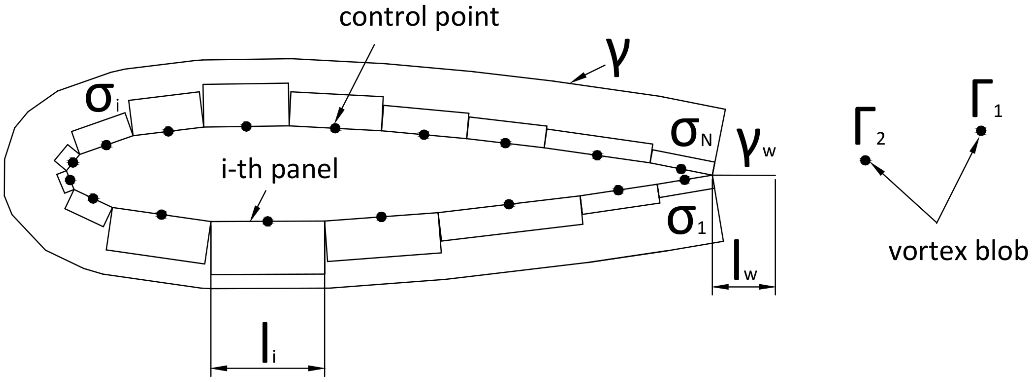

Figure 2.9: Singularities distribution in the attached flow condition

the flow is constrained to leave the aerofoil parallel to either the upper or the lower surface instead to the bisector of the trailing edge angle, as it happens in the real flow. In the present model, to overcame this issue, the position of the panel is set parallel to the vector sum of the velocities at the two adjacent panels at the trailing edge. So, the panel inclination indirectly depends on the value of $\partial \Gamma_{aerofoil}/\partial t$.

In this configuration the model has N_p+2 unknowns (the N_p source intensity σ_i, the vorticity γ and the circulation of the panel in the wake Γ_w) and it needs N_p+2 boundary conditions to be determined. Due to the linearity of the Laplace equation the velocity normal to the panel in the $i-th$ control point can be expressed as the sum of the velocity induced by each singularities plus the freestream velocity:

$$\bar{u}_i(t)\cdot\bar{n}_i(t) = [\bar{u}_{i\infty} + \sum_{j=1}^{N_p}\sigma_j(t)\bar{A}_{ij} + \gamma(t)\sum_{j=1}^{N_p}\bar{B}_{ij} + \gamma_w(t)\bar{C}_{iw}(t) + \bar{u}_{iv}(t)]\cdot\bar{n}_i(t) \tag{2.37}$$

Where:

- $\bar{n}_i(t)$ is the normal vector to the $i-th$ panel.
- $\bar{u}_i(t)$ is the total velocity in the $i-th$ control point.
- $\bar{u}_{i\infty}$ is the freestream velocity in the $i-th$ control point.
- A_{ij}, B_{ij} are the influence matrices in the $i-th$ control point due to the $j-th$ panel, for the source and the vorticity, respectively.
- $C_{iw}(t)$ is the influence matrix for the first panel in the wake.

- $\bar{u}_{iv}(t) = \sum_{k=1}^{N_v(t)} \Gamma_{k,v} \bar{D}_{ik}$: velocity induced from all the vortex blobs of the wake in the $i-th$ control point.
- $N_v(t)$: number of vortex blobs in the wake.

The first boundary condition is based on the requirement that the flow does not penetrate the surface in each N_p control points:

$$[\bar{u}_i(t) - \bar{u}_{ia}(t)] \cdot \bar{n}_i(t) = \bar{w}_i(t) \cdot \bar{n}_i(t) = 0 \tag{2.38}$$

where:

- $\bar{u}_{ia}(t)$ is the velocity of the aerofoil's surface in the $i-th$ point
- $\bar{w}_i(t)$ is the velocity in the frame of reference attached to the aerofoil

At this point only other two boundary conditions are needed to solve the system of equations. The first comes from the Kelvin's theorem, which states that: *In an inviscid, barotropic flow with conservative body forces, the circulation around a closed curve moving with the fluid remains constant with time* ([27]). So, the substantial derivative of the circulation in a closed path around the aerofoil and its wake (in the inviscid region) is constant in time:

$$\frac{D\Gamma}{Dt} = 0 \tag{2.39}$$

The statement of this theorem is fundamental in the unsteady aerodynamics problems, because it introduces the time - dependent term in the boundary conditions of the Laplace equation.

If we consider an aerofoil surrounded by a flow at rest for $t = 0$ (Fig. 2.10 the circulation around the curve (a) is equal to zero. When $t > 0$ the flow suddenly sets into motion and circulation $\Gamma_{aerofoil}$ develops around the aerofoil. But, from the Kelvin's theorem, the circulation around the path (a) in Fig.2.10 still has to be zero. So, a starting vortex Γ_{wake} must exist and its intensity is equal and opposite to $\Gamma_{aerofoil}$.

In the present model this means that the sum of the circulation of all the singularities is zero in each time step:

$$\gamma(t) l_a + \Gamma_w + \sum_{k=1}^{N_v(t)} \Gamma_{k,v} = 0 \tag{2.40}$$

where:

- l_a is the total length of the aerofoil surface

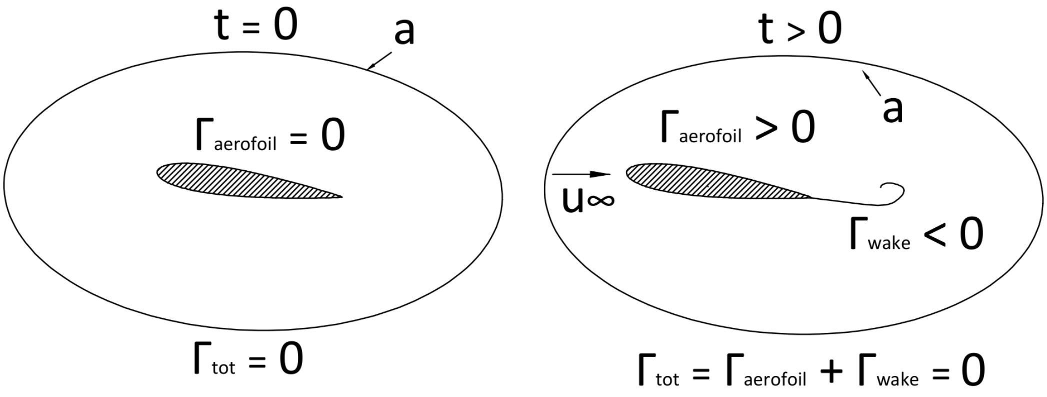

Figure 2.10: Kelvin Theorem

- $\Gamma_w = \gamma_w(t) l_w(t)$ is the circulation of the first panel in the wake
- $\Gamma_{k,v}$ is circulation of $k - th$ vortex blob

The last boundary condition needed to close the problem is the Kutta condition, which will be described in detail in section 2.1.3

2.1.2 Separated Flow

Previous research works (e.g., Riziotis et al. [28], M. Vezza et al. [29], J. Katz [30]) extended the vortex panel methods to separated flows by introducing in addition to the trailing edge vortex panel a second panel originating from the separation point. This "double wake" concept is based on the remark that at separation, vorticity is continuously released in the inviscid flow along a strong shear layer that bounds the separation bubble. The circulation that is released at the separation position, can be assessed from the velocity on the edge of the shear layer (Fage and Johansen [31]). So, the circulation around a rectangle of length l_{sp} across the vortex sheet (see Fig. 2.11), having sides parallel and normal to the sheet, is given by:

$$\Gamma_{sp} = \oint_C \bar{u} \cdot d\bar{l} \approx (u^+ - u^-) l_{sp} \tag{2.41}$$

where:

$$l_{sp} = \frac{(u^+ + u^-)}{2} dt \tag{2.42}$$

If the velocities are evaluated in the aerofoil frame of reference, where $w^- = 0$,

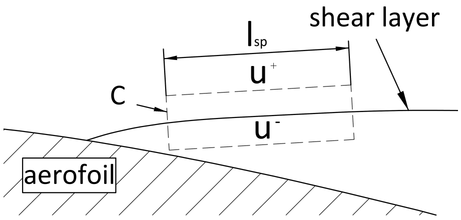

Figure 2.11: Circulation in the separated shear layer

the released circulation is:

$$\Gamma_{sp} \approx \frac{(w^+)^2}{2} dt \tag{2.43}$$

The stall, if its position is known, can be modelled by adding a singularity of strength Γ_{sp} at the separation position (Riziotis et al. [28]). This purely inviscid approach was shown (Riziotis et al. [28] and M. Vezza et al. [29]) to produce an aerodynamic load prediction in good agreement with the experimental results.

Another approach can be adopted to clarify the way we are modelling the physics of the flow separation. Full Navier-Stokes equations can be written as:

$$\frac{\partial \bar{w}}{\partial t} = -\bar{w} \cdot \nabla \bar{w} - \frac{\nabla p}{\rho} + \nu \nabla^2 \bar{w} \tag{2.44}$$

where the acceleration term due to the noninertial reference frame has been neglected (it is usually very small in the present applications). Equations (2.44) can be used to express the rate of change of circulation around a closed path c across the boundary layer (Fig. 2.12):

$$\begin{aligned} \frac{d\Gamma}{dt} &= \oint_c \frac{\partial \bar{w}}{\partial t} \cdot d\bar{l} = -\oint_C (\bar{w} \cdot \nabla \bar{w}) \cdot d\bar{l} - \oint_C \frac{\nabla p}{\rho} d\bar{l} + \oint_C \nu \nabla^2 \bar{w} \cdot d\bar{l} = \\ &= -\int_A \nabla \times (\omega \times \bar{w}) \cdot \bar{n}\, dA + \oint_c \nu \nabla^2 \bar{w} \cdot d\bar{l} \end{aligned} \tag{2.45}$$

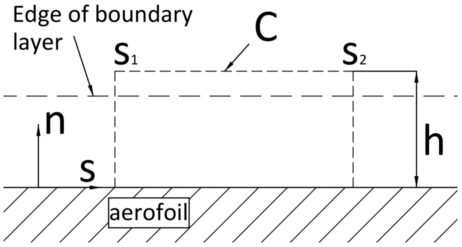

Figure 2.12: Control volume across the boundary layer

where Stokes theorem and vector identity $(\bar{w} \cdot \nabla)\, \bar{w} = \bar{\omega} \times \bar{w} + \nabla\left(w^2/2\right)$ have been used to obtain the final result.

The viscous term in eq.(2.45) is significant only on the body surface, where it can be evaluated by using eq.(2.44):

$$\oint_c \nu \nabla^2 \bar{w} \cdot d\bar{s} = \int_{s_2}^{s_1} \nu \left(\frac{\partial^2 w_s}{\partial n^2}\right)_{n=0} ds = \int_{s_2}^{s_1} \frac{1}{\rho} \left(\frac{\partial p}{\partial s}\right)_{n=0} dx = \frac{p_1 - p_2}{\rho} \tag{2.46}$$

The convective term in eq.(2.45) can be expressed as:

$$\begin{aligned} &\int_A \nabla \times (\omega \times \bar{w}) \cdot \bar{n}\; dA = \\ &\int_0^h \int_{s_1}^{s_2} \frac{\partial}{\partial s}(\omega w_s) ds dn + \int_{s_1}^{s_2} \int_0^h \frac{\partial}{\partial n}(\omega w_n) ds dn = \\ &\int_0^h (\omega w_s)_{s=s_2} dn - \int_0^h (\omega w_s)_{s=s_1} dn \end{aligned} \tag{2.47}$$

Substitution of equations (2.46) and (2.47) into eq. (2.45) leads to:

$$\frac{d\Gamma}{dt} = -\int_0^h (\omega w_s)_{s=s_2} dn + \int_0^h (\omega w_s)_{s=s_1} dn + \frac{p_1 - p_2}{\rho} \tag{2.48}$$

This equation shows that the time rate of change of circulation depends on an advection term (the net flux of vorticity) and a diffusion term corresponding to a streamwise pressure difference. As an example, we can assume that the separation starts inside the control volume at s_1, and that s_2 lies inside the separation region at the position where the tangential velocity is zero. In this case the vorticity flux at $s = s_2$ is obviously zero. Applying the Kutta condition (see sec. 2.1.3), the pressure jump across the two boundaries turns out to be zero, so also the diffusion term in eq. (2.48) vanishes. Therefore,

$$\frac{d\Gamma}{dt} = \int_0^h (\omega w_s)_{s=s_1} dn = \frac{w_e^2}{2} \tag{2.49}$$

where w_e is the relative velocity at the edge of the boundary layer. It could be objected that in the case of flow separation in s_1 the boundary layer disappears and, strictly speaking, eq.(2.48) is no longer valid.

However, eq.(2.49) relates a rate of change of circulation to a vorticity flux through section s_1, which cannot disappear as the flow separates. Therefore, it must be accepted that there is a circulation released in the inviscid flow at the separation point.

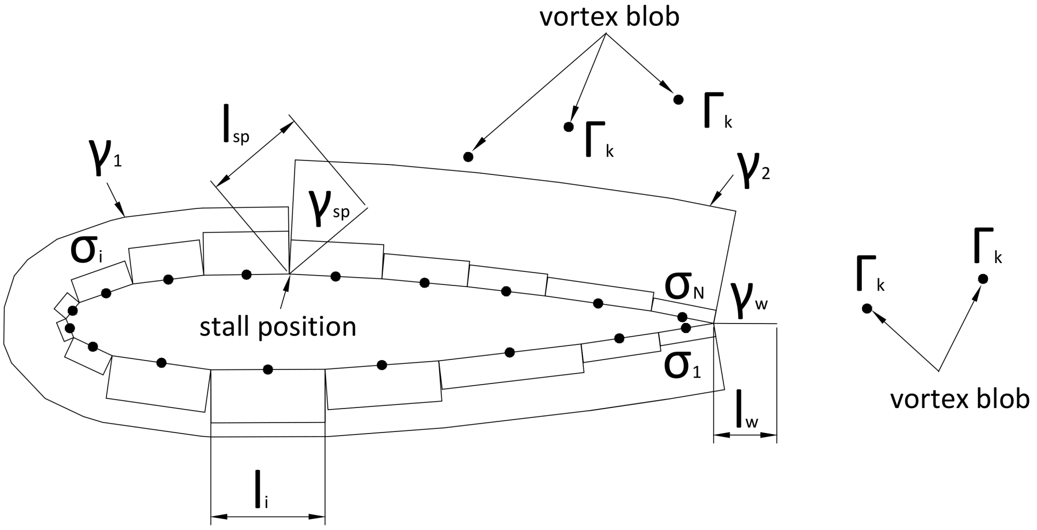

Figure 2.13: Singularities distribution in the separated flow condition

To recapitulate, there is a vorticity that cannot be diffused (the viscous term is set to zero) and cannot disappear, so it should be injected in the irrotational flow. To meet this requirement, in the present model, an additional panel with constant vorticity is introduced at the separation point. Its circulation is given by eq.(2.49):

$$\Gamma_{sp} = \frac{w_e^2}{2}\Delta t \tag{2.50}$$

which is exactly the same solution of eq.(2.43) if $w_e = w^+$. This means that at the point where separation occurs the vorticity flux coming from the boundary layer is released into the inviscid flow field through the shedding of vortex blobs.

As for the case of attached flow, the system of equations for the separated flow past an aerofoil will be presented. In multi-aerofoil problems, the only difference is in the additional computation of the velocities induced by the others aerofoils and their wakes. Figure 2.13 shows the singularities distribution for the separated flow. In this case the unknowns are $N_p + 4$: the N_p source intensity, σ_i, the circulation per unit length on the aerofoil, γ_1 and γ_2, the circulation around the wake panel, Γ_w, and the circulation of the panel at the stall position, Γ_{sp}. The direction of the trailing edge wake panels is derived as in the attached flow condition, until reverse flow occurs. At this point the inclination is assumed to be parallel to the surface of the pressure side to mimic what happens in the real flow. The direction of the panel in the separation wake is determined by averaging the velocities at the panel centre and at the separation position. The first boundary condition is the no-penetration requirement, as in the attached flow condition (eq.(2.38)), but the normal velocity at the $i-th$ point is obtained from the new set of singularities:

$$\begin{aligned}\bar{u}_i(t)\cdot\bar{n}_i(t) = [\bar{u}_{i\infty} + \bar{u}_{iv}(t) + \sum_{j=1}^{N_p}\sigma_j(t)\bar{A}_{ij} + \gamma_1(t)\sum_{j=1}^{N_{sp}(t)-1}\bar{B}_{ij} \\ +\gamma_2(t)\sum_{j=N_{sp}(t)}^{N_p}\bar{B}_{ij} + \gamma_w(t)\bar{C}_{iw}(t) + \gamma_{sp}(t)\bar{C}_{isp}(t)]\cdot\bar{n}_i(t)\end{aligned} \tag{2.51}$$

where:

- $N_{sp}(t)$ is the index of the panel where the stall occurs
- $\gamma_1(t), \gamma_2(t)$ are the circulation per unit length on the aerofoil surface referred to the attached flow portion and to the separated one, respectively.
- $C_{isp}(t)$ is the influence matrix for the first panel in the separation wake

The second condition is the Kelvin's theorem:

$$\gamma_1(t)(l_a - l_2(t)) + \gamma_2(t)l_2(t) + \Gamma_w(t) + \Gamma_{sp}(t) + \sum_{k=1}^{N_v(t)}\Gamma_{k,v} = 0 \tag{2.52}$$

where:

- $\Gamma_w(t) = \gamma_w(t)l_w(t)$ is the circulation of the panel in the trailing edge wake.
- $\Gamma_{sp}(t) = \gamma_{sp}(t)l_{sp}(t)$ is the circulation of the panel at the separation position
- $l_2(t)$ is the length of the aerofoil surface where γ_2 is applied
- $N_v(t)$ is the number of the vortex blobs in the wake

The third and fourth boundary conditions come from the experimental observation that the tangential velocity after the separation is equal to zero and the shed circulation at that position can be derived from the velocity at the edge of the shear layer:

$$\Gamma_{sp}(t) = \gamma_{sp}(t)l_{sp}(t) = \frac{(w^+_{s,sp})^2}{2}\Delta t \tag{2.53}$$

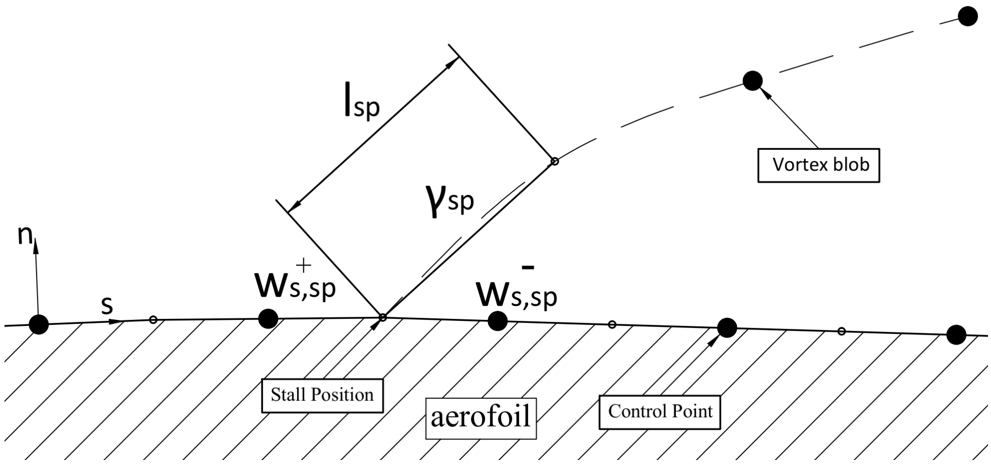

Figure 2.14: Separation Point

where $w^+_{s,sp}$ is the tangential velocity just before the stall position (Fig. 2.14). With this boundary condition the set of equations is not anymore linear and an iterative scheme, with an initial guess, needs to be implemented. The requirement of the third condition (tangential velocity equal to zero) is applied to the control point just after the stall position ($w^-_{s,sp} = 0$ in Fig. 2.14). The fifth, and last, boundary condition is derived from the Kutta condition that will be described in the next section together with the one used in the attached flow condition. The model described above is able to model unsteady, incompressible separated flow but the deficiency is that the separation point should be known a priori. To overcome this problem the thin, steady boundary layer theory is used and coupled with the potential flow solution.

2.1.3 The unsteady Kutta condition

The present model, both in attached and separated flow conditions, is based on the assumption that the flow outside the boundary layer can be considered as inviscid. Under this hypothesis another condition needs to be invoked to obtain a unique solution. In 1902 Willhelm Kutta proposed the following rule: *In flow over a two-dimensional body with a sharp trailing edge, there develops a circulation of magnitude just sufficient to move the rear stagnation point to the trailing edge.* This is called the Kutta condition and its mathematical formulation depends on the model that is used. In the present model, for steady flow conditions it leads to imposing equal tangential velocity in the control points of the two panels at the trailing edge. It should be note that this condition can be interpreted, in steady condition, as no vorticity shedding

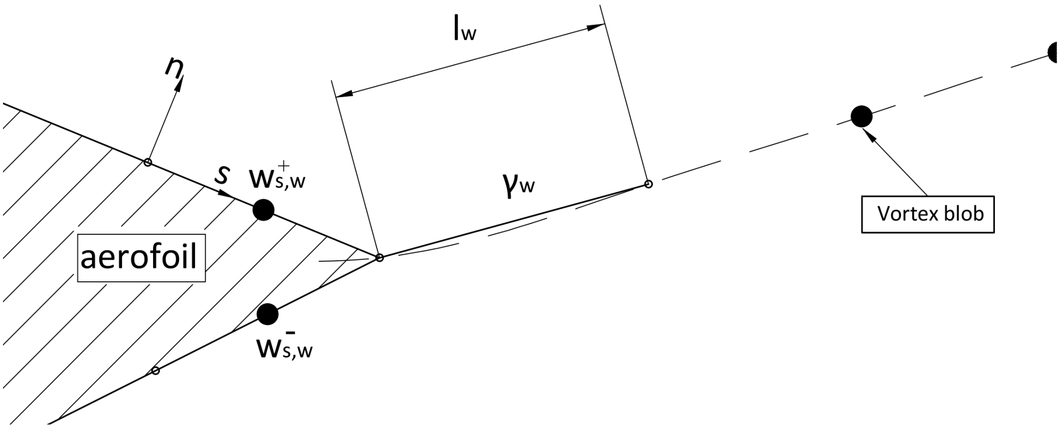

Figure 2.15: Trailing Edge

from the aerofoil and zero-loading of the trailing edge (because the pressures on the two sides are equal).

For unsteady flow, the interpretation of the Kutta condition is not unique in the literature and this leads to different formulations. One is based on the requirement that the vorticity at the trailing edge should be equal to zero (Katz [30]), which can be fulfilled imposing equal velocities in the control points of the two panels at the trailing edge both in attached and separated flow conditions. This is also the formulation used by Giensing [32]. To understand its physical meaning, the unsteady Bernulli equation applied at the trailing edge (see Fig. 2.15) is considered:

$$\frac{\partial \phi^+}{\partial t} - \frac{\partial \phi^-}{\partial t} + \frac{(w_s^+)^2 - (w_s^-)^2}{2} = \frac{p^- - p^+}{\rho} \tag{2.54}$$

When the surface velocities are made equal ($w_s^+ = w_s^-$), since the flow is unsteady $\left(\frac{\partial \phi^+}{\partial t} \neq \frac{\partial \phi^-}{\partial t}\right)$, a pressure jump at the trailing edge should occur. The implication is that there is a finite loading applied to the trailing edge and to the wake, which is not acceptable on physical grounds [26].

The second formulation is the one proposed by Basu et al. [26] where the Kutta condition for unsteady flow is interpreted as a zero loading across the trailing edge and the shed vorticity. So, from eq.(2.54) with $p^+ = p^-$, a velocity difference is present that is compatible with the shedding of vorticity during unsteady motion. In the present model, due to its persuasive physical justification and after some numerical tests (see Zanon and Ferreira [33]), this second approach was used.

The boundary condition for attached flow can be expressed as:

$$\frac{\partial \phi^-}{\partial t} - \frac{\partial \phi^+}{\partial t} = -\frac{\partial \Gamma_a}{\partial t} = \frac{(w_s^+)^2 - (w_s^-)^2}{2} = \frac{(w_s^+ + w_s^-)(w_s^+ - w_s^-)}{2} \tag{2.55}$$

where the right-hand side could be interpreted as the outflow of vorticity from the two boundary layers. As explained in subsection 2.1.2, the vorticity flux does not disappear but it is convected downstream, so that a singularity of strength $\gamma_w = w_s^+ - w_s^-$ and length $(w_s^+ + w_s^-)dt/2$ is introduced at the trailing edge.

When the angle of attack reaches the critical value separation occurs and a different Kutta condition should be used for both separation and trailing edge panels. With the same approach used above, the unsteady Bernoulli equation is applied at the two sides of each panel so obtaining:

$$Trailing\ edge \Rightarrow \Delta h = \frac{\partial}{\partial t}(\phi^- - \phi^+) + \frac{1}{2}[(w_{s,w}^-)^2 - (w_{s,w}^+)^2] \tag{2.56}$$

$$Separation\ point \Rightarrow \Delta h = \frac{\partial}{\partial t}(\phi_s^+ - \phi_s^-) + \frac{1}{2}(w_{s,sp}^+)^2 \tag{2.57}$$

where the region between the two wakes exhibits a total head jump Δh with respect to the outer region. Joining together the two equations, the Kutta condition is obtained [29]:

$$\frac{\partial}{\partial t}(\phi^- - \phi^+) - \frac{\partial}{\partial t}(\phi_s^+ - \phi_s^-) = -\frac{\partial \Gamma_a}{\partial t} = -\frac{1}{2}[(w_{s,w}^-)^2 - (w_{s,w}^+)^2] + \frac{1}{2}(w_{s,sp}^+)^2 \tag{2.58}$$

The time derivative of the circulation can be expressed by introducing singularities where the vorticity is shed in the potential flow:

$$-\frac{\partial \Gamma_a}{\partial t} = \frac{\partial}{\partial t}[\gamma_w l_w + \gamma_{sp} l_{sp}] \tag{2.59}$$

Which is equivalent to the Kelvin's theorem. In conclusion, it can be noted that a consequence of the unsteady Kutta condition is that all the vorticity in the boundary layers is shed in the inviscid flow at the separation point and at the trailing edge.

2.2 Viscous Boundary Layer

Nowadays, many methods for the computation of the boundary layer flow can be found in the literature, based on both integral equations and partial differential equations (see, e.g., Kline et al. [34]). Among the different models, the Drela's integral approach for steady flows [35] has proved over the years its ability in simulating laminar and turbulent boundary layers. Since its implementation is relatively simple and well suited to panel methods it has been chosen for the present model. Although an extended model for slow unsteady flow can be found in Riziotis et al. [17], at this stage of development, the present model uses the steady equations. This could be a weakness, but it will be shown that the use of the quasi-steady flow approximation for the boundary layer is reasonable for the purposes of the present model. The starting point of Drela's approach is the Prandtl boundary layer equations:

$$conservation\ of\ mass \Rightarrow \frac{\partial(\rho w_s)}{\partial s} + \frac{\partial(\rho w_n)}{\partial n} = 0 \qquad \boxed{2.60}$$

$$conservation\,of\ momentum \Rightarrow \rho w_s \frac{\partial w_s}{\partial s} + \rho w_n \frac{\partial w_s}{\partial n} = \rho_e w_e \frac{d w_e}{ds} + \frac{\partial \tau}{\partial n} \qquad \boxed{2.61}$$

where s,n are the local streamwise and normal coordinates, w_s,w_n are the velocity components and τ is the total shearing plus Reynolds stress. The values at the edge of the boundary layer are denoted by subscript e. By integrating eq.(2.61) across the boundary layer, the von Karman momentum equation is obtained:

$$\frac{s}{\vartheta}\frac{d\vartheta}{ds} = \frac{s}{\vartheta}\frac{C_f}{2} - \left(\frac{\delta^*}{\vartheta} + 2 - M_e^2\right)\frac{s}{w_e}\frac{dw_e}{ds} \qquad \boxed{2.62}$$

Where:

- $\vartheta = \int_0^\infty (1 - \frac{w_s}{w_e})\frac{\rho w_s}{\rho_e w_e} dn$ is the momentum thickness
- $\delta^* = \int_0^\infty (1 - \frac{\rho w_s}{\rho_e w_e}) dn$ is the displacement thickness
- $C_f = \frac{2}{\rho_e w_e^2}\tau_w$ is the skin friction coefficient
- M_e is the mach number at the edge of the boundary layer.

If eq.(2.61) is multiplied by velocity w_s and then integrated, the kinetic energy integral equation is obtained:

$$\frac{s}{\vartheta^*}\frac{d\vartheta^*}{ds} = \frac{s}{\vartheta^*}2C_D - (\frac{2\delta^{**}}{\vartheta^*} + 3 - M_e^2)\frac{s}{w_e}\frac{dw_e}{ds} \qquad \boxed{2.63}$$

where:

- $\vartheta^* = \int_0^\infty (1 - (\frac{w_s}{w_e})^2)\frac{\rho w_s}{\rho_e w_e} dn$ is the kinetic energy thickness

- $\delta^{**} = \int_0^\infty (1 - \frac{\rho}{\rho_e}) \frac{w_s}{w_e} dn$ is the density thickness
- $C_D = \frac{1}{\rho_e w_e^3} \int_0^\infty \tau \frac{\partial w_s}{\partial n} dn$ is the dissipation coefficient.

By introducing the following shape parameters:

$$H = \frac{\delta^*}{\vartheta} \quad H^* = \frac{\vartheta^*}{\vartheta} \quad H^{**} = \frac{\delta^{**}}{\vartheta} \tag{2.64}$$

the momentum and kinetic energy (shape parameter) equations become:

$$\frac{s}{\vartheta} \frac{d\vartheta}{ds} = \frac{s}{\vartheta} \frac{C_f}{2} - (H + 2 - M_e^2) \frac{s}{w_e} \frac{dw_e}{ds} \tag{2.65}$$

$$\frac{s}{H^*} \frac{dH^*}{ds} = \frac{s}{\vartheta} \frac{2C_D}{H^*} - \frac{s}{\vartheta} \frac{C_f}{2} - (\frac{2H^{**}}{H^*} + 1 - H) \frac{s}{w_e} \frac{dw_e}{ds} \tag{2.66}$$

Finally, under the assumption of incompressible flow (Mach number M_e below 0.3, which is common in wind turbines applications), the equations used in the present model are obtained:

$$\frac{\partial \vartheta}{\partial s} + (2 + H) \frac{\vartheta}{w_e} \frac{\partial w_e}{\partial s} = \frac{C_f}{2} \tag{2.67}$$

$$\vartheta \frac{\partial H^*}{\partial s} + (H^*(1 - H)) \frac{\vartheta}{w_e} \frac{\partial w_e}{\partial s} = 2C_D - H^* \frac{C_f}{2} \tag{2.68}$$

Von Karman equation (2.67) and the shape parameter equation (2.68) are valid for laminar, turbulent and free wake boundary layers.

Figure 2.16 shows the boundary layer characteristics for an aerofoil at medium-low *Reynolds* number and high angle of attack. The boundary layer starts from the stagnation point and, moving toward the suction side, it stays laminar up to the separation bubble. At this point, the shape parameter H (that directly indicates how close the boundary layer is to separation [36]) reaches a critical value and laminar separation occurs. When the flow becomes turbulent, the increase in momentum transport may lead to the reattachment of the boundary layer (or may not) as far as turbulent separation point is reached. The region between the laminar separation and the turbulent reattachment is called separation bubble and its length is a function of the *Reynolds* number. For flows with high turbulence intensity, or for high *Reynolds* number and low angle of attack, the laminar instabilities can induce transition before the occurrence of laminar separation and the separation bubble is not present. To solve equations (2.67) and (2.68) a set of empirical relationships, depending on the flow condition, need to be introduced.

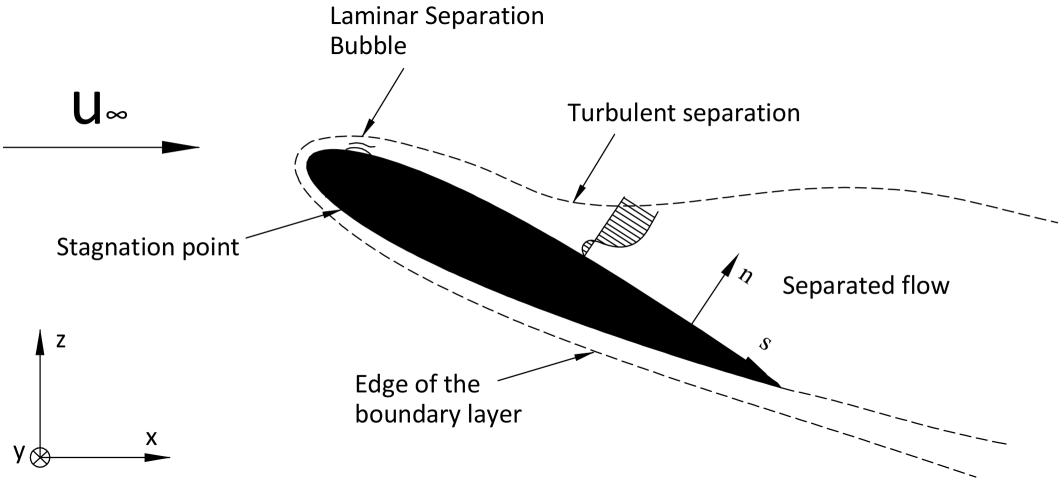

Figure 2.16: Boundary layer on an Aerofoil at high angle of attack

The laminar closure relationships are based on the Falkner-Skan one-parameter velocity profiles and are presented in Drela [37] or Wolles et al. [38] in the form (see appendix A):

$$H^* = H^*(H, Re_\vartheta) \quad C_f = C_f(H, Re_\vartheta) \quad C_D = C_D(H, Re_\vartheta) \tag{2.69}$$

To increase the accuracy of the laminar equations inside the separation bubble Drela used non-similar velocity profiles. When compared to the Falkner-Skan profiles, these latter have smaller reverse velocities and are claimed to be more representative of the typical separation bubble profiles [39].

The turbulent closure equations are taken from Xfoil [39] (see appendix B):

$$\begin{gathered} H^* = H^*(H, Re_\vartheta) \quad C_f = C_f(H, Re_\vartheta) \quad C_D = C_D(H, Re_\vartheta, C_\tau) \\ C_{\tau eq} = C_{\tau eq}(H, H^*, Re_\vartheta) \quad \delta = \delta(H, \vartheta, \delta^*) \end{gathered} \tag{2.70}$$

where a third differential equation (the “Shear lag equation”) is added to take into account the upstream history effects (for more details about this equation, see, e.g., Drela [37] or Kernkamp [40]):

$$\frac{\delta}{C_\tau}\frac{\partial C_\tau}{\partial s} = k(\sqrt{C_{\tau eq}} - \sqrt{C_\tau}) + \frac{2\delta}{w_e}\left(\frac{\partial w_e}{\partial s}\right)_{eq} - \frac{2\delta}{w_e}\frac{\partial w_e}{\partial s} \tag{2.71}$$

In the wake, where the momentum and the shape equations are still valid if skin friction coefficient C_f is set to zero, a new set of empirical relations needs to be added. As pointed out by Drela [37], the wakes in aerodynamic flows of interest should not be laminar, so only the turbulent relations are needed. Turbulent boundary layer closure equations (2.70) and (2.71) (with C_f set to zero) describe quite well the free wakes, so a slightly modified version of them is used [39] (see appendix C).

For the laminar-turbulent transition, the spatial-amplification theory based on the *Orr - Sommerfeld* equations is used (e^n method, [41]). This method assumes transition when the *Tollmien - Schlichting* wave has grown by a an empirical factor (usually $e^9 = 8103$) that is a function of the turbulence intensity of the freestream flow. The simplified version for the Falkner - Skan profile family derived by Drela et al. [42] is implemented in the present model.

2.3 Viscous-Inviscid Interaction

As anticipated in the introduction of this chapter, the flow field past an aerofoil can be split into a viscous zone close to the surface and an outer inviscid zone. In the previous sections the governing equations for these two flow regions were presented. The velocities at the edge of the boundary layer are the solution of the potential flow problem, which is influenced in turn by the development of the boundary layer. Therefore, a coupling strategy and a proper solution algorithm of the equations pertaining to the two flow regions are required. This is a not trivial problem due to serious difficulties arising in the numerical solution.

The coupling procedure adopted in the present model is described in the following sections.

2.3.1 Definition of Transpiration Velocity

Under the assumption of thin boundary layer ($\delta^* << L$) the velocity field can be computed approximately as inviscid. In the length scale of the outer potential flow, the velocity at the aerofoil surface is:

$$w_e = \lim_{n/L \to 0} w_s$$

where n is the distance from the surface and L is the chord of the aerofoil. Expanding the region close to the surface, the tangential velocity w_e becomes the flow velocity at the edge of the boundary layer. In the length scale of the viscous layer, w_e is seen as the flow velocity at large distance from the surface, i.e.:

$$w_e = \lim_{n/\delta^* \to \infty} w_s$$

Thus, w_e is, at the same time, the tangential velocity on the body surface in the inviscid scale, L, and the velocity at infinite distance from the aerofoil in the viscous scale, δ^*. This is an acceptable approximation as long as the value of n is large compared to δ^* but small compared to L or, in other words, $\delta^* << L$. After a first computation of potential flow velocity w_e on the aerofoil surface, the inviscid pressure distribution (or the velocity field in steady flow) can be corrected for the presence of the boundary layer in the following manner. From the solution of the viscous equations, the velocity normal to the surface at large distance $n/\delta^* \to \infty$ (but at small distance in the inviscid scale, $n/L \to 0$) can be computed and then used as a boundary condition for the potential flow:

$$\underbrace{w_n|_{n/L=0}}_{Inviscid} = \underbrace{\lim_{n/\delta^* \to \infty} w_n(s,n)}_{Viscous} \quad \text{(2.72)}$$

Velocity component $w_n(s,n)$ can be computed in terms of w_s by using the continuity equation for incompressible flow:

$$w_n(s,n) = \int_0^n \frac{\partial w_n}{\partial n^*}(s,n^*)dn^* = -\frac{\partial}{\partial s}\int_0^n w_s dn^*$$

or

$$w_n(s,n) = \frac{\partial}{\partial s}\int_0^n [w_e(s) - w_s(s,n^*)]dn^* - n\frac{dw_e}{ds}$$

At this point, if n^* is large compared to δ and so $w_s(s,n^*) \approx w_e(s)$, the integral can be extended to ∞ and, by using the definition of displacement thickness, it yields:

$$w_n(s,n) = \frac{d}{ds}w_e\delta^* - n\frac{dw_e}{ds}$$

Evaluating this equation at $n = 0$ (respect to L) and considering that the edge velocity of the boundary layer has to be equal to the surface velocity obtained from the potential flow, the relations that couple the inviscid and the viscous flows are:

$$Transpiration\ Velocity \Rightarrow w_n|_{n/L=0} = w_{transp.} = \frac{d}{ds}(w_e\delta^*) \quad \text{(2.73)}$$
$$w_{e,inviscid} = w_{e,viscous}$$

To recapitulate, in the inviscid flow the presence of the boundary layer is simulated changing the boundary condition $w_n|_{n=0} = 0$ at the wall with $w_n|_{n=0} = w_{transp.}$. Unfortunately, the transpiration velocity neither is known at priori nor is an explicit function of the problem unknowns, so that an iterative solution scheme is needed.

2.3.2 Coupling Algorithm

After the definition of the transpiration velocity, an appropriate algorithm to compute the interaction between the boundary layer and the potential flow has to be designed. Special care is required in the selection of a suitable coupling strategy, because an inappropriate choice can lead to insurmountable mathematical difficulties [43]. This happens when the solution of the viscous flow is computed from a prescribed pressure distribution on the aerofoil surface, which leads to an ill-posed problem in those regions where a strong interaction exists between the viscous and inviscid flow. An example is the so called the "Goldstein singularity" [44] that occurs in the flow separation point where the existence of a solution for the boundary layer equation with prescribed pressure is uncertain. This is the main problem of the classical "direct" method, where the inviscid flow equations are solved with a prescribed displacement thickness whereas the viscous flow is solved with a prescribed pressure (or edge velocity in steady flow, Fig. 2.17). To overcome these difficulties must be chosen a different approach, and in the following section the main solution strategies will be described. To simplify the description, the equations are written in terms of w_e (velocity at the edge of the viscous region) and δ^* (displacement thickness), so that:

$$PotentialFlow \Rightarrow w_e = f(\delta^*) \tag{2.74}$$

$$BoundaryLayer \Rightarrow w_e = g(\delta^*) \tag{2.75}$$

Direct iterative method . It solves eq.(2.74) + eq.(2.75) with the following scheme (Fig. 2.17):

$$\begin{aligned} w_e^n &= f(\delta^{*n-1}) \\ \delta^{*n} &= g^{-1}(w_e^n) \end{aligned} \tag{2.76}$$

where n is the iteration counter and g^{-1} is the symbolic inverse of g). When the interaction between the viscous and the inviscid part of the flow is weak, this algorithm could converge; on the contrary, when the interaction is strong (like in the separation bubble or at the trailing edge of an aerofoil) g^{-1} is near singular (see [43]) and no solution can be found.

Inverse Method . To avoid the use of g^{-1}, the iteration process needs to be reversed, so obtaining (Fig. 2.18):

$$\begin{aligned} \delta^{*n} &= f^{-1}(w_e^{n-1}) \\ w_e^n &= g(\delta^{*n}) \end{aligned} \tag{2.77}$$

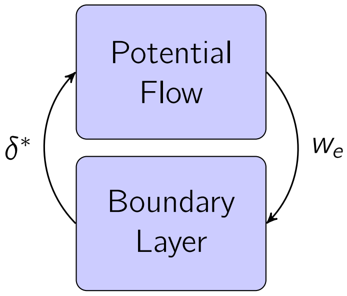

Figure 2.17: Direct Method

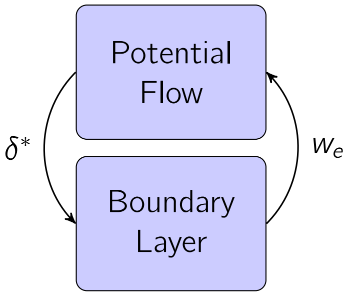

Figure 2.18: Inverse Method

In this form, the equations system does not exhibit any numerical difficulty, but the large under-relaxation required to get the convergence increases substantially the computational time (see [43]).

Semi-inverse Method . The direct and inverse methods are combined to speed up the convergence while keeping the stability of the inverse method (Fig. 2.19). :

$$\begin{aligned} w_{e,p} &= f({\delta^*}^{n-1}) \\ w_{e,b} &= g({\delta^*}^{n-1}) \\ {\delta^*}^{n} &= \lambda(w_{e,p}, w_{e,b}, {\delta^*}^{n-1}) \end{aligned} \tag{2.78}$$

where λ represents a relaxation function.

Simultaneous Method . This approach performs the simultaneous solution of the viscous and inviscid flow equations. It assures a fast convergence but the numerical implementation is a rather difficult task.

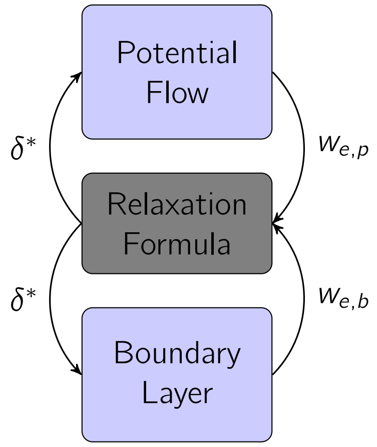

Figure 2.19: Semi-inverse Method

From the description above, it turns out that the semi-inverse or the simultaneous method should be chosen to simulate separated flows past an aerofoil. The main goal of the computer code developed in the present thesis is to demonstrate the ability of the "double wake" panel method in simulating complex flows like the wake after a VAWT. Maximizing the efficiency of the numerical solver was not the major goal. Therefore, to avoid numerical complications, a semi-inverse method was used instead of the simultaneous coupling.

The semi-inverse method performs the coupling by solving both the viscous and the inviscid flow equations for the same value of the displacement thickness, δ^*. Since the present model uses the concept of "transpiration velocity" to simulate the presence of the boundary layer, it is not possible to prescribe directly δ^* to the potential flow equations. So, a slightly different approach was used and it is represented in Fig. 2.20. The equations are:

$$\begin{aligned} w_{e,p} &= f({w_{transp.}}^{n-1}) \\ w_{e,b} &= g({\delta^*}^{n-1}) \\ {\delta^*}^{n} &= \lambda(w_{e,p}, w_{e,b}, {\delta^*}^{n-1}) \\ {w_{transp.}}^{n} &= \frac{d}{ds}(w_{e,b}{\delta^*}^{n}) \end{aligned} \tag{2.79}$$

and the relaxation function λ is:

$$ {\delta^*}^{n} = {\delta^*}^{n-1}\left(1 + K_{rx}\frac{w_{e,b} - w_{e,p}}{w_{e,b}}\right) \tag{2.80}$$

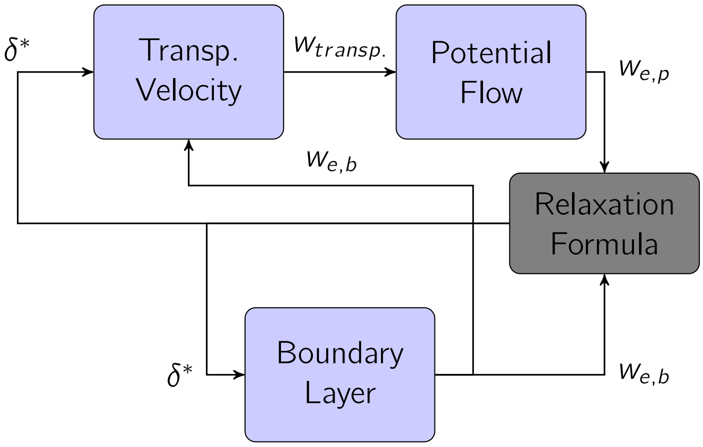

Figure 2.20: Semi-inverse Method, present code

Coefficient K_{rx} should be chosen sufficiently smaller than unity in order to guarantee fast convergence and stability of the numerical procedure. Moreover it should have a different value for the laminar and turbulent portions of the boundary layer (usually smaller in the turbulent case).

2.3.3 Coupling Procedure

In this subsection it will be described how the boundary conditions of the inviscid equations change due to the presence of the boundary layer. The two cases of attached and separated flows will be distinguished.

Attached flow . The iterative procedure starts by considering the flow around the aerofoil as inviscid and hence using the boundary condition in eq.(2.38). The boundary layer equations are solved starting from the stagnation point near the leading edge and moving towards the trailing edge along the pressure and the suction sides of the aerofoil. In the wake, for few chords downstream, the boundary layer equations are also solved by posing $C_f = 0$ (zero friction). For this purpose several source panels are introduced in the wake and their strength is set equal to the transpiration velocity. After this first iteration, the boundary conditions for inviscid equations are modified from:

$$Inviscid \Rightarrow \bar{w}_i(t) \cdot \bar{n}_i(t) = 0 \tag{2.81}$$

to

$$Inviscid\ \&\ Viscous \Rightarrow \bar{w}_i(t) \cdot \bar{n}_i(t) = \frac{d}{ds}(w_e \delta^*) \tag{2.82}$$

and velocity $\bar{u}_{i,bl}(t)$ induced by the sources in the wake is included in the velocity computation:

$$\begin{aligned}
Inviscid \Rightarrow \bar{u}_i(t) &= \bar{u}_{i\infty} + \sum_{j=1}^{N_p} \sigma_j(t)\bar{A}_{ij} \\
&+\gamma(t)\sum_{j=1}^{N_p} \bar{B}_{ij} + \gamma_w(t)\bar{C}_{iw}(t) + \bar{u}_{iv}(t)
\end{aligned}$$

$$\begin{aligned}
Inviscid \;\&\; Viscous \Rightarrow \bar{u}_i(t) &= \bar{u}_{i\infty} + \sum_{j=1}^{N_p} \sigma_j(t)\bar{A}_{ij} \\
&+\gamma(t)\sum_{j=1}^{N_p} \bar{B}_{ij} + \gamma_w(t)\bar{C}_{iw}(t) + \bar{u}_{iv}(t) + \bar{u}_{i,bl}(t)
\end{aligned} \tag{2.83}$$

Separated Flow . As before, the iteration procedure starts by considering the flow as inviscid and the separation position is obtained from the solution at the previous time step. The boundary layer equations are still solved starting from the stagnation point near the leading edge and moving towards the trailing edge as far as separation occurs (when $C_f < 0$ and, hopefully, on the suction side). Transpiration velocity is set equal to zero on both wakes originating at the trailing edge and at the separation point. The same is done in the whole separated flow region between the two wakes, which means that the boundary layer is not considered in that region.

3

Computational procedure

The present numerical model is aimed at simulating the Vertical Axis Wind Turbine behaviour throughout its operating range, in different geometrical configurations and for uneven freestream velocity. The computational model is required to be flexible and able to handle different geometries and laws of motion. The presence of diffusers or obstacles in the flow field should be taken into account in order to study their influence on turbine performance.

To meet this requirements, the present code allows the law of motion of any kind of body to be specified as an input, and to select models of different degree of complexity, namely, potential flow, coupled potential-boundary layer flow for attached or moderately separated flow, inviscid modelling of the stall. The code is designed to handle unsteady flows, but the steady solutions can be obtained for attached (or moderately separated) flows directly rather than as a degeneration of the unsteady problem. The computer code has been written in the high-level Matlab language, using the multidimensional feature and the implicit parallelization. In the previous chapter the flow governing equations and the viscous-inviscid coupling algorithm were presented, while in the present the details of the solution algorithm are provided.

3.1 Code structure

The solution procedure developed in the present thesis consists of several blocks that are enabled according to the fluid dynamic problem considered (inviscid, viscous flow, etc.). The general computational procedure, for the unsteady potential-boundary layer flow with inviscid modelling of the stall, is presented hereafter (see Fig 3.1). In this situation there are three nested loops: the inner one will be called “inviscid loop”, the outer one is the “time step loop”, and the intermediate one is the “viscous loop”.

The simulation starts with the loading of all information about the fluid dynamic problem, namely, the geometry and law of motion of each solid body and the freestream velocity distribution. Then the, first time step iteration starts, and the velocities induced by the wakes, the freestream velocities and the surface velocities are computed at aerofoil control-points. The panels in the trailing edge wake and in the separated wake if any, are created with an initial guess of their inclination (θ_w, θ_{sp}) and length (l_w, l_{sp}) (in the subsequent time steps the values at the old time level are used). The system of linear equations is built up and all the boundary conditions are applied. The system is solved by a parallelized Gaussian elimination algorithm and the new values of θ and l are computed. If the convergence criterion on the values of l_w, l_{sp}, θ_w, θ_{sp} is not fulfilled, the new values are assigned to the variables and the "inviscid" iteration restarts (see fig 3.1). This inner loop is extremely fast and it requires about 4 iterations to get the convergence.

After the "inviscid" loop is finished, an initial value of δ^* is guessed (in the subsequent time steps the values at the old time level are used) and the boundary layer equations are solved over the body surface and, if the flow is attached, on the wake. The inviscid and the viscous edge velocities are then compared and if the convergence criterion is not met, δ^{*n} is computed by the relaxation formula (2.80). The transpiration velocity is updated by eq.(2.79) (see section 2.3.1), and, in the case of attached flow, the strength of the wake source panels are computed. At this point the system of equations is rebuilt with the new boundary conditions and the "inviscid" loop is recalled. When the convergence criterion for the "viscous" loop is satisfied (in about 6-8 iterations depending on the flow configuration) the aerodynamic forces are computed, and all the results are stored for the next time step. The panels in the trailing edge wake and at the stall position are transformed into vortex blobs whose core size is set equal to panel length. The status of the boundary layer is evaluated to check the occurrence of flow separation. The "time step loop" ends with the convection of the wake according to the velocities induced at the position of each vortex blob.

In the present case, the limitation of the computational cost would suggest the use of a simultaneous method (see paragraph 2.3.2) and a Newton - Raphson solution algorithm. However, this approach would increase considerably the complexity of the code and it was deemed unnecessary to speed up a numerical procedure that is fast enough for the present purposes, i.e., the simulation of VAWT.

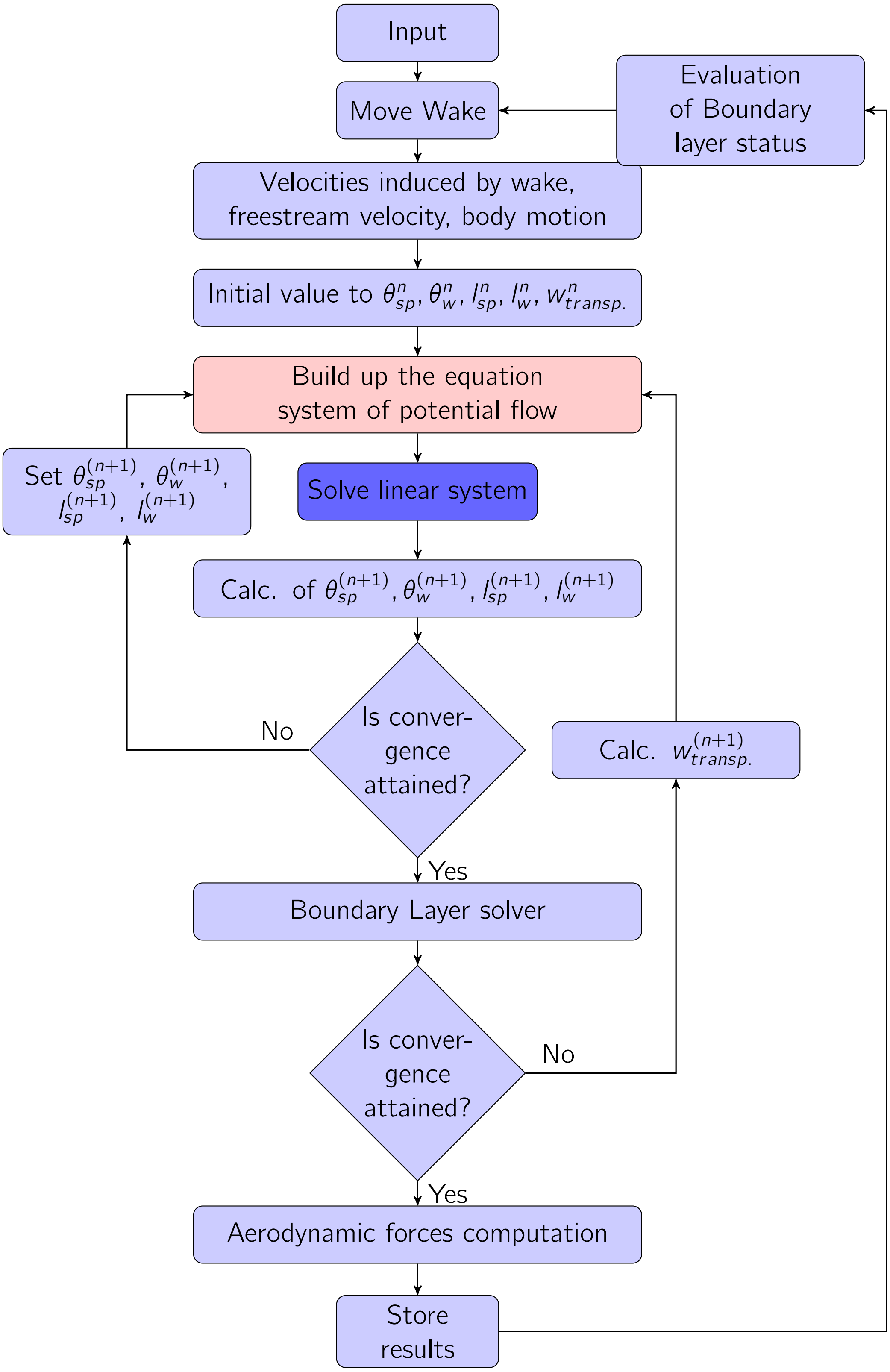
Input
Move Wake
Evaluation of Boundary layer status
Velocities induced by wake, freestream velocity, body motion
Initial value to $\theta^n_{sp}, \theta^n_w, l^n_{sp}, l^n_w, w^n_{transp.}$
Build up the equation system of potential flow
Set $\theta^{(n+1)}_{sp}$, $\theta^{(n+1)}_w$, $l^{(n+1)}_{sp}$, $l^{(n+1)}_w$
Solve linear system
Calc. of $\theta^{(n+1)}_{sp}, \theta^{(n+1)}_w, l^{(n+1)}_{sp}, l^{(n+1)}_w$
No
Is convergence attained?
Calc. $w^{(n+1)}_{transp.}$
Yes
Boundary Layer solver
Is convergence attained?
No
Yes
Aerodynamic forces computation
Store results

Figure 3.1: Flow-chart of the solution procedure.

3.2 Numerical Details

The aerofoil geometry is provided as an input data by a collection of points that are connected by straight-lines, the panels. They are numbered in clockwise order, starting from the trailing edge. So, there are N_p panels (188 in the present simulations) and the two panels that meet at the trailing edge have indexes 1 and N_p. For each panel, the unit vectors normal and tangent to the surface ($\bar{n}_i$ and $\bar{s}_i$) are computed. The normal unit vector is directed outward the body surface and the tangent one is directed according to the clockwise rotation around the aerofoil.

A constant source distribution of strength σ_j, and a constant vortex distribution, γ_1 or γ_2 (see section 2.1.2), are assigned to each panel. The wake panels at the separation point and at the trailing edge are built, and the initial values of their length (l_w, l_{sp}) and inclination (θ_w, θ_{sp}) are taken from the old time level. Since, for constant source and vortex strength, the velocity is infinite at the ends of each panel, the boundary conditions on the aerofoil surface are imposed at N_p control points located in the middle of each panel. Then the following computations are performed in the $i-th$ control point:

- Influence matrices $\bar{A}_{i,j}$, $\bar{B}_{i,j}$, $\bar{C}_{i,w}$, $\bar{C}_{i,sp}$ (see sections 2.1.1 and 2.1.2) are computed using equations (2.34) and (2.36).

- The freestream velocity, $\bar{u}_{i,\infty}$, is computed using the velocity distribution provided in the input file.

- The velocity induced by the collection of the vortex blobs in the wakes, $\bar{u}_{iv} = \sum_{k=1}^{N_v} \Gamma_{k,v} \bar{D}_{ik}$, is computed using equation (2.30).

- The velocity of the body surface, $\bar{u}_{i,a}$, is computed by second-order accurate backward finite differences.

The first boundary condition (eq.(2.82)) leads to N_p equations in $N_p + 4$ unknowns:

$$1^{st} B.C. \Rightarrow (\bar{u}_i - \bar{u}_{i,a}) \cdot \bar{n}_i = \bar{w}_{i,transp.} \quad for \ i = 1, 2, \ldots, N_p \tag{3.1}$$

where $\bar{u}_i$ is defined for separated flows by eq.(2.51) and for attached flows by eq.(2.83). Introducing the other boundary conditions for separated flows and moving the known terms and the transpiration velocity at the right-hand side, the following system of linear equations is obtained:

$$\begin{array}{c|ccccccc|}
 & A_{n,1,1} & \cdots & A_{n,1,N_p} & B_{n,1,\gamma_1} & B_{n,1,\gamma_2} & C_{n,1,w} & C_{n,1,sp} \\
1^{st} & & & & \vdots & & & \\
 & A_{n,N_p,1} & \cdots & A_{n,N_p,N_p} & B_{n,N_p,\gamma_1} & B_{n,N_p,\gamma_2} & C_{n,N_p,w} & C_{n,N_p,sp} \\
2^{nd} & 0 & \cdots & 0 & (l_a - l_2) & l_2 & l_w & l_{sp} \\
3^{rd} & A_{s,N_{sp+1},1} & \cdots & A_{s,N_{sp+1},N_p} & B_{s,N_{sp+1},\gamma_1} & B_{s,N_{sp+1},\gamma_2} & C_{s,N_{sp+1},w} & C_{s,N_{sp+1},sp} \\
4^{th} & A_{s,\Delta w,1} & \cdots & A_{s,\Delta w,N_p} & B_{s,\Delta w,\gamma_1} & B_{s,\Delta w,\gamma_2} & C_{s,\Delta w,w} - 1 & C_{s,\Delta w,sp} \\
5^{th} & A_{s,N_{sp},1} & \cdots & A_{s,N_{sp},N_p} & B_{s,N_{sp},\gamma_1} & B_{s,N_{sp},\gamma_2} & C_{s,N_{sp},w} & C_{s,N_{sp},sp} - 1
\end{array} \bullet$$

$$\begin{bmatrix} \sigma_1 \\ \vdots \\ \sigma_{N_p} \\ \gamma_1 \\ \gamma_2 \\ \gamma_w \\ \gamma_{sp} \end{bmatrix} = \begin{bmatrix} -\left(u_{n,1,\infty} + u_{n,1,v}\right) + u_{n,1,a} + w_{1,transp.} \\ \vdots \\ -\left(u_{n,N_p,\infty} + u_{n,N_p,v}\right) + u_{n,N_p,a} + w_{N_p,transp.} \\ -\sum_{k=1}^{N_v(t)} \Gamma_{k,v} \\ -\left(u_{s,N_{sp+1},\infty} + u_{s,N_{sp+1},v}\right) + u_{s,N_{sp+1},a} \\ -\left(u_{s,\Delta w,\infty} + u_{s,\Delta w,v}\right) + u_{s,\Delta w,a} \\ -\left(u_{s,N_{sp},\infty} + u_{s,N_{sp},v}\right) + u_{s,N_{sp},a} \end{bmatrix} \tag{3.2}$$

where

- $A_{n,i,j} = \bar{A}_{i,j} \cdot \bar{n}_i$
- $A_{s,i,j} = \bar{A}_{i,j} \cdot \bar{s}_i$
- $A_{s,\Delta w,j} = \bar{A}_{1,j} \cdot \bar{s}_1 + \bar{A}_{N_p,j} \cdot \bar{s}_{N_p}$
- $B_{n,i,\gamma_1} = \sum_{j=1}^{N_{sp}-1} \bar{B}_{i,j} \cdot \bar{n}_i$
- $B_{s,i,\gamma_1} = \sum_{j=1}^{N_{sp}-1} \bar{B}_{i,j} \cdot \bar{s}_i$
- $B_{s,\Delta w,\gamma_1} = \sum_{j=1}^{N_{sp}-1} \bar{B}_{1,j} \cdot \bar{s}_1 + \sum_{j=1}^{N_{sp}-1} \bar{B}_{N_p,j} \cdot \bar{s}_{N_p}$
- $B_{n,i,\gamma_2} = \sum_{j=N_{sp}}^{N_p} \bar{B}_{i,j} \cdot \bar{n}_i$
- $B_{s,i,\gamma_2} = \sum_{j=N_{sp}}^{N_p} \bar{B}_{i,j} \cdot \bar{s}_i$
- $B_{s,\Delta w,\gamma_2} = \sum_{j=N_{sp}}^{N_p} \bar{B}_{1,j} \cdot \bar{s}_1 + \sum_{j=N_{sp}}^{N_p} \bar{B}_{N_p,j} \cdot \bar{s}_{N_p}$
- $C_{n,i,w} = \bar{C}_{i,w} \cdot \bar{n}_i$
- $C_{s,i,w} = \bar{C}_{i,w} \cdot \bar{s}_i$

- $C_{s,\Delta w,w} = \bar{C}_{1,w} \cdot \bar{s}_1 + \bar{C}_{N_p,w} \cdot \bar{s}_{N_p}$
- $C_{n,i,sp} = \bar{C}_{i,sp} \cdot \bar{n}_i$
- $C_{s,i,sp} = \bar{C}_{i,sp} \cdot \bar{s}_i$
- $C_{s,\Delta w,sp} = \bar{C}_{1,sp} \cdot \bar{s}_1 + \bar{C}_{N_p,sp} \cdot \bar{s}_{N_p}$

The system of equations for attached flow conditions is obtained by performing the following changes in eq.(3.2):

- The 3^{rd} boundary condition is replaced by $\gamma_1 = \gamma_2$
- The 5^{th} boundary condition is changed into the requirement $\gamma_{sp} = 0$
- The velocity induced by the sources in the wake, $\bar{u}_{i,bl}$, is introduced in the right-hand side.

So, for attached flow conditions:

$$\begin{array}{r} \\ 1^{st} \\ \\ 2^{nd} \\ 3^{rd} \\ 4^{th} \\ 5^{th} \end{array}
\left[\begin{array}{ccccccc}
A_{n,1,1} & \cdots & A_{n,1,N_p} & B_{n,1,\gamma_1} & B_{n,1,\gamma_2} & C_{n,1,w} & C_{n,1,sp} \\
 & & & \vdots & & & \\
A_{n,N_p,1} & \cdots & A_{n,N_p,N_p} & B_{n,N_p,\gamma_1} & B_{n,N_p,\gamma_2} & C_{n,N_p,w} & C_{n,N_p,sp} \\
0 & \cdots & 0 & (l_a - l_2) & l_2 & l_w & l_{sp} \\
0 & \cdots & 0 & 1 & -1 & 0 & 0 \\
A_{s,\Delta w,1} & \cdots & A_{s,\Delta w,N_p} & B_{s,\Delta w,\gamma_1} & B_{s,\Delta w,\gamma_2} & C_{s,\Delta w,w} - 1 & C_{s,\Delta w,sp} \\
0 & 0 & 0 & 0 & 0 & 0 & 1
\end{array}\right] \bullet$$

$$\begin{bmatrix} \sigma_1 \\ \vdots \\ \sigma_{N_p} \\ \gamma_1 \\ \gamma_2 \\ \gamma_w \\ \gamma_{sp} \end{bmatrix} =
\begin{bmatrix}
-\left(u_{n,1,\infty} + u_{n,1,v} + u_{n,1,bl}\right) + u_{n,1,a} + w_{1,transp.} \\
\vdots \\
-\left(u_{n,N_p,\infty} + u_{n,N_p,v} + u_{n,N_p,bl}\right) + u_{n,N_p,a} + w_{N_p,transp.} \\
-\sum_{k=1}^{N_v(t)} \Gamma_{k,v} \\
0 \\
-\left(u_{s,\Delta w,\infty} + u_{s,\Delta w,v} + u_{s,\Delta w,bl}\right) + u_{s,\Delta w,a} \\
0
\end{bmatrix} \tag{3.3}$$

Once the system of linear equations (3.2) or (3.3) has been is solved the length and the inclination of the panels at the separation point and at the trailing edge can be computed:

- $l_w^{n+1} = \Delta t(w_{s,N_p} - w_{s,1})/2$, where $w_{s,i}$ is the tangential component of the velocity in the i-th control point in the aerofoil frame of reference and n is the iteration counter

- $l_{sp}^{n+1} = (\Delta t \ w_{s,N_{sp}})/2$

- $\theta_w^{n+1} = tan^{-1}\left(\frac{w_{s,1}s_{y,1}+w_{s,N_p}s_{y,N_p}}{w_{s,1}s_{x,1}+w_{s,N_p}s_{x,N_p}}\right)$ where $s_{x,i}$ and $s_{y,i}$ are the x and y components, respectively, of the tanget unit vector, $\bar{s}_i$, at the *i-th* panel.

- $\theta_{sp}^{n+1} = tan^{-1}\left(\frac{w_{s,N_{sp}}s_{y,N_{sp}}+w_{y,sp}}{w_{s,N_{sp}}s_{x,N_{sp}}+w_{x,sp}}\right)$ where $w_{x,sp}$ and $w_{y,sp}$ are the x and y velocity components, respectively, at the midpoint of the panel in the separated wake.

The new values of l and θ are compared with the old ones, and if the convergence conditions are not fulfilled (e.g., if $|\frac{l_w^{n+1}-l_w^n}{l_w^n}| > 10^{-5}$) the new values are assigned to the variables and the panel influence matrices $\bar{C}_{i,w}$ and $\bar{C}_{i,sp}$ are computed again. Then, the system of equations is rebuilt up and the loop is repeated until convergence is attained.

The boundary layer equations (2.67), (2.68) and (2.71) are discretized by 2^{nd}-order accurate differences. The unknowns are computed in the same control points used in the inviscid problem. These point are numbered starting from the stagnation point of the leading edge and moving towards the trailing edge, and their curvilinear coordinate ζ is computed on both pressure and suction sides of the aerofoil. The discretized momentum, shape and shear-lag equations, at the *i-th* station are:

$$ln\left(\frac{\vartheta_{i+1}}{\vartheta_i}\right) - \frac{1}{2}ln\left(\frac{\zeta_{i+1}}{\zeta_i}\right)\left(C_f\frac{\zeta}{\vartheta}\right)_{i+\frac{1}{2}} + (H_{i+\frac{1}{2}}+2)ln\left(\frac{w_{s,i+1}}{w_{s,i}}\right) = 0 \tag{3.4}$$

$$ln\left(\frac{H^*_{i+1}}{H^*_i}\right)+(1-H_{i+\frac{1}{2}})ln\left(\frac{w_{s,i+1}}{w_{s,i}}\right)+ln\left(\frac{\zeta_{i+1}}{\zeta_i}\right)\left(\frac{C_f\zeta}{2\vartheta}-\frac{2C_D\zeta}{H^*\vartheta}\right)_{i+\frac{1}{2}} = 0 \tag{3.5}$$

$$\begin{aligned} k\left(\sqrt{C_{\tau eq}}-\sqrt{C_\tau}\right)_{i+\frac{1}{2}}(\zeta_{i+1}-\zeta_i) - \delta_{i+\frac{1}{2}}ln\left(\frac{C_{\tau,i+1}}{C_{\tau,i}}\right) \\ +2\delta_{i+\frac{1}{2}}\left(U_{q,i+\frac{1}{2}}(\zeta_{i+1}-\zeta_i) - ln\left(\frac{w_{s,i+1}}{w_{s,i}}\right)\right) = 0 \end{aligned} \tag{3.6}$$

where

- ζ_i is the curvilinear coordinate of the *i-th* boundary layer station.

- $U_{q,i+\frac{1}{2}} = \frac{1}{w_{s,i+\frac{1}{2}}}\left(\frac{\partial w_s}{\partial \zeta}\right)_{eq,i+\frac{1}{2}}$

Logarithmic differencing of the derivatives is used because it gives an exact result in similar flows, so diminishing the discretization error resulting from the large values of $\Delta\zeta/\zeta$ that occur near the leading edge [37].

The boundary layer equations are solved on each side of the aerofoil, using the value of δ^* at the old time level by a Newton-Raphson solution procedure. The velocities at the edge of the boundary layer, $w_{e,b}$, are then compared with the velocities of the potential flow, $w_{e,p}$. If the convergence criterion is not fulfilled (i.e., $|\frac{w_{e,b,i}-w_{e,p,i}}{w_{e,b,i}}| > 0.01$) for the next iteration step a new value of δ^{*n+1} is computed by the relaxation formula in eq.(2.80), while the transpiration velocity is computed by eq.(2.73) discretized by third-order central differences to avoid spurious oscillations.

Once the convergence criterion on $w_{e,p}$, $w_{e,b}$ is fulfilled, the aerodynamic forces are computed by integrating the surface pressures and by adding the skin friction contribution. The pressure in the *i-th* control point is computed by using the unsteady Bernulli equation:

$$\frac{p_\infty - p_i}{\rho} = \frac{1}{2}\left(u_i^2 - u_\infty^2\right) + \left(\frac{\partial\phi_i}{\partial t} - \frac{\partial\phi_\infty}{\partial t}\right) \tag{3.7}$$

where $\partial\phi_i/\partial t$ is defined in an Eulerian reference frame. The change in potential with respect to time for a point on the body surface can be computed by converting to a body Lagrangian reference frame:

$$\frac{\partial\phi_i}{\partial t}|_{Eulerian} = \frac{\partial\phi_i}{\partial t}|_{body} - \bar{u}_{i,a}\cdot\nabla\phi \tag{3.8}$$

where the potential function on the aerofoil surface is approximated by integrating the surface velocity field from the trailing edge in the clockwise direction. In the separated flow region, if any, the total head jump Δh (sec. 2.1.3) with respect to the outer region is added to eq.(3.7).

Once a complete solution has been obtained at time t, the model is then set up for time $t+\Delta t$. Existing vortices are convected to their new positions by computing the velocities of their centres and using the first order Euler scheme:

$$\bar{X}_i^{n+1} = \bar{X}_i^n + \bar{u}_i(\Delta t) \tag{3.9}$$

where Δt is the time step, $\bar{X}_i$ is the position vector of the $i-th$ vortex blob and $\bar{u}_i$ is the velocity of the blob centre. Velocity $\bar{u}_i$ is computed by using eq.(2.83) for attached flows and eq.(2.51) for separated flows.

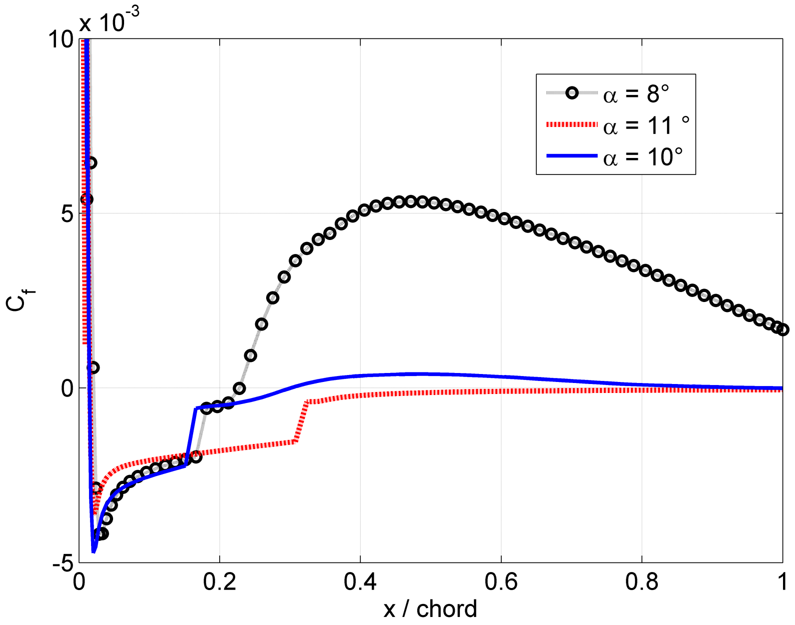

Figure 3.2: Skin friction coefficient (C_f) on the suction side of a Naca 0012 aerofoil, $Re = 5 \cdot 10^4$ and $\alpha = 8°, 10°$ and $11°$. Steady solution, single wake.

3.3 Separation criterion

As mentioned previously, the separation criterion used in the present code is based on the value of the skin friction coefficient C_f (flow separates when C_f becomes negative). This has been shown to be a reliable criterion in previous works (see Riziotis et al. [17]), but it fails when applied to pitching aerofoils at medium-low *Reynolds* numbers. In fact, when a transition bubble is present, it does not allow to recover a reattachment condition after a deep stall at the leading edge has occurred.

To understand what happens under these conditions, Figure 3.2 shows the skin friction coefficient on the suction side of a Naca 0012 aerofoil for an angle of attack of 8° and $Re = 5 \cdot 10^4$, computed in a steady flow condition. It should be noted that the flow is attached, but C_f is negative for $0.02 < x/L < 0.23$. This is because the shape factor reaches its critical value before the *Tollmien - Schlichting* wave has grown enough to trigger the transition, and laminar separation occurs. Moreover, for this angle of attach, when the flow becomes turbulent, the increase of momentum transport leads to flow reattachment. This does not happen for $\alpha = 11°$ (Fig. 3.2) where laminar separation occurs and the flow does not reattach any longer. Therefore, when the angle of

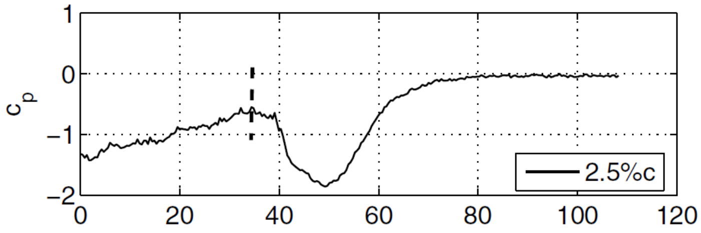

a) Nondimensional time, τ

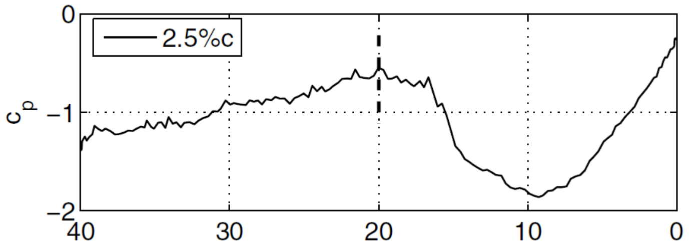

b) α , deg

Figure 3.3: Pressure coefficient C_p at 2.5%-chord location on the suction side of the aerofoil during downstroke. a) C_p against the nondimensional time b) C_p against the angle of attack. The dashed lines indicate the $|C_p| - rise$ point [46]

attack increases during the pitching motion (upstroke), the separation point does not move with continuity from the trailing edge to the leading edge but the separation "jumps" from a position downstream of the transition bubble (usually close to the trailing edge) to the leading edge (Fig. 3.2 shows attached flow for $\alpha = 10°$ and separated flow from the leading edge for $\alpha = 11°$). This is a usual behaviour of aerofoils at *Reynolds* numbers below $3 \cdot 10^5$ [45]. In the pitching motion of an aerofoil in a real flow, when the angle of attack exceeds the static stall angle, this "explosion" of the stall creates a big leading edge vortex that strongly affects the flow field, as shown by the PIV data presented in the next chapter. The criterion based on the sign of C_f has no problem in predicting the position of the separation point when it moves from the trailing edge to the leading edge, also in such an extreme condition. On the contrary, this criterion fails during the downstroke, when the flow is still separated from the leading edge but the angle of attack is low enough to allow the flow to reattach after a transition bubble. In fact, the application of the C_f criterion in this condition leads to the prediction of a separation point that cannot move back through the transition bubble.

In order to handle the flow reattachment, an additional criterion needs to

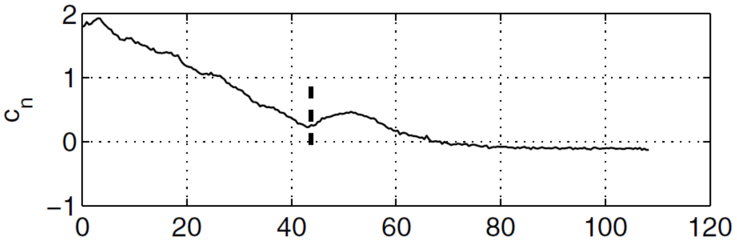

a) Nondimensional time, τ

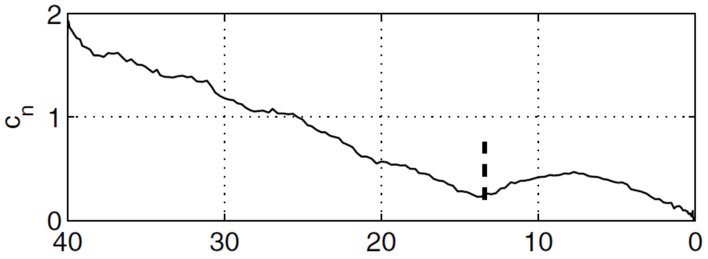

b) α, deg

Figure 3.4: Trend of the aerofoil normal force coefficient C_n during the downstroke. a) C_n against the nondimensional time b) C_n against the angle of attack. The dashed lines indicate the C_{Nmin} point [46]

be introduced. This is a crucial point because the periodic separation and reattachment is also a feature of the flow past a VAWT.

From the analysis of the PIV data collected by the author (see chapter 4), and in agreement with Sheng et al. [47], the reattachment process on pitching aerofoils occurs when the vorticity on the suction side is convected downstream, so allowing the boundary layer to be reestabilished. Niven et al. [46] had taken the start of that process to be the suction pressure rise ($|C_p| - rise$) at the 2.5%-chord location (Fig 3.3).

However, they also clarified that there was no particular significance about this location and it could have been taken anywhere in the leading edge suction region. Sheng et al. [47] found that the convective process ends at the time when the normal force coefficient reaches a local minimum, C_{Nmin} (Fig. 3.4).

During the downstroke of pitching motion (Figure 3.5) the angle of attack of $|C_p| - rise$ turns out to be is almost independent of the reduced pitch rate, $r = \dot{\alpha}L/2U_\infty$. The time needed to complete the convection process is also independent of r, thus the angle of attack at which the reattachment process comes to an end depends linearly on the reduced pitch rate (Figure 3.5).

On the basis of the above experimental observations, the following algo-

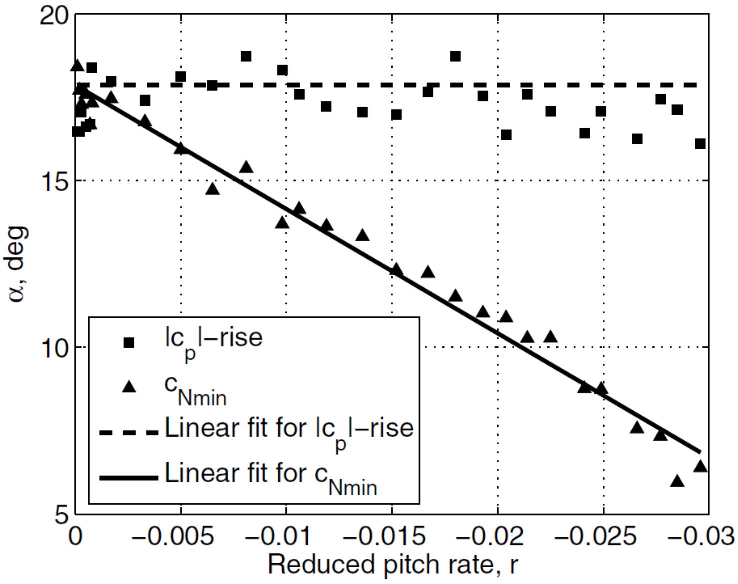

Figure 3.5: Angles of attack of reattachment start ($|C_p| - rise$) and end (C_{Nmin}) for different reduced pitch rates [46]

rithm is developed to handle the flow reattachment at low *Reynolds* numbers. During the upstroke, the increase of flow acceleration on the leading edge leads to a stronger diffusion of the velocity on the suction side of the aerofoil, which causes shape factor H to rise. As stated in section 2.2, the value of H directly indicates how close the boundary layer is to separation, so its increase indicates that the laminar separation position in the transition bubble is moving towards the leading edge and that the turbulent flow is losing its ability to cope with the adverse pressure gradient (compare the results for $\alpha = 8°$ and $\alpha = 10°$in Fig. 3.2). Then, during upstroke, it is possible to single out a critical position of the laminar separation point beyond which the turbulent boundary layer does not reattach any longer. From this observation, it seems reasonable to assume that as long as the laminar separation position is upstream of the critical one, the turbulent flow will not be able to cope with the adverse pressure gradient. Thus, in the present solution procedure, it is assumed that during downstroke the turbulent reattachment cannot exist as long as the laminar separation position is upstream of the critical point stored during the upstroke. When the laminar separation reaches the critical position and shape factor H starts to strongly decrease, the turbulent reattachment becomes possible and the position of the separation panel is no longer based on the sign of the skin friction coefficient. As mentioned previously, in the real flow the reattachment starts when all the vorticity on the suction side of the aerofoil is convected downstream. To mimic this behaviour, in the present model the position of the separation panel is forced to move downstream (even if $C_f < 0$) with the same velocity of the the surrounding vortex blobs as long as the stored position of the turbulent separation (memorized in the critical laminar separation position during upstroke) is reached. At this point, the position of the separation panel is kept fixed until a new boundary layer is established on the suction side. When the skin friction coefficient becomes greater than zero the separation criterion on the C_f is restored.

It should be noted that the aim of the present work is not to simulate pitching aerofoils, but more complex flows. Therefore, it may happen that during the reattachment the angle of attack starts to increase again, restoring a fully separated flow condition. This is not a problem when adopting the proposed algorithm because an increase of the angle of attack causes an increase of shape factor H that stops the reattachment routine and restores the criterion based on the skin friction.

4

Validation of the Numerical Model

In this Chapter the predictive capability of the model and the PIV data collected by the author are presented. In the dynamic stall working conditions of VAWT, the vorticity field is characterised by a strong leading edge vortex that is shed during the upwind part of the blade rotation, is convected downstream by the flow and interacts with the blade in the downwind part of the rotation. The simulation of this behaviour is a challenging matter, where many uncontrollable variables play an important role. For this reason, before comparing the code predictions with the VAWT experimental data two simpler configurations are considered. The first one is the steady aerofoil, which allows the results to be compared with those of Drela's Xfoil code (that uses the same boundary layer equations as the present model). The second one is an aerofoil in pitching motion, which shares some features with the Vertical Axis Wind Turbine (i.e., periodicity of the flow, dynamic stall), but not the wake-blade interaction.

In the first section, the results for the steady and pitching aerofoils obtained at $Re = 1.5 \times 10^6$ for a NACA 0015 profile are compared with the experimental data collected at the University of Glasgow [18] and the predictions of the code developed by Riziotis et al. [17].

The second section provides a comparison of the numerical results with the forces extracted from 2D-PIV experimental data concerning the steady and pitching motion of a NACA 0012 aerofoil. The *Reynolds* number is $Re = 5 \times 10^4$ and the experiments were performed by the author at the Delft University of Technology.

4.1 Naca 0015, steady and pitching motion

In this section the numerical results are presented for a NACA 0015 aerofoil in steady and unsteady pitching motion and in deep stall. They are compared with experimental data obtained at the Glasgow University low speed wind tunnel [18] for $Re = 1.5 \times 10^6$ and $Ma = 0.12$. The boundary layer was

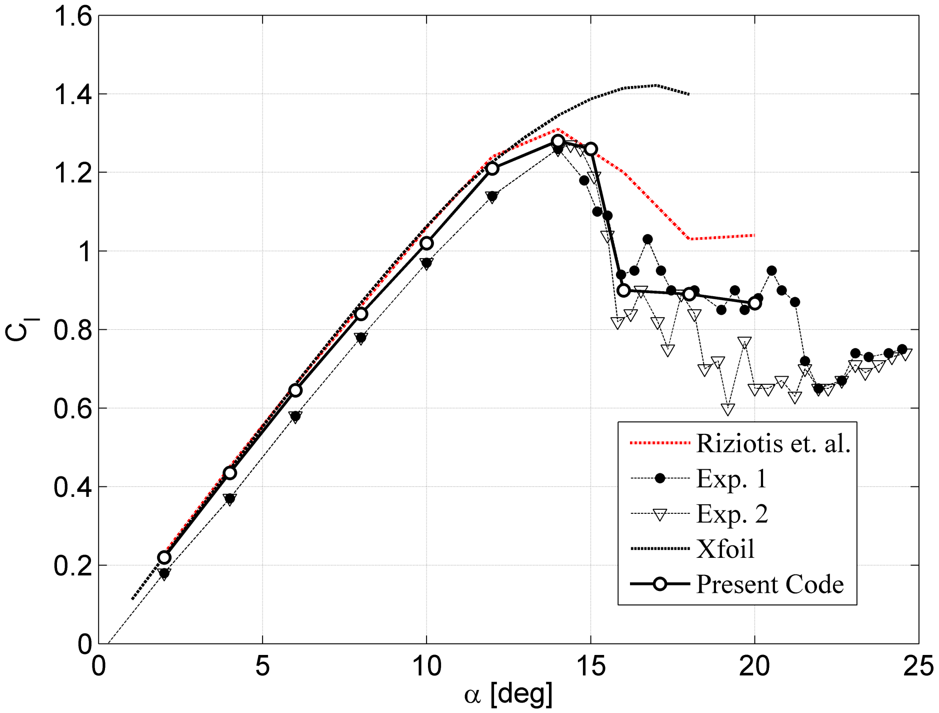

Figure 4.1: Comparison of steady lift coefficient. NACA 0015, $Re = 1.5 \times 10^6$.

tripped on both the upper and lower surface of the aerofoil with transition strips placed at the leading edge. The pitching motion is sinusoidal, with mean angle $\alpha_0 = 11°$, amplitude $\alpha_1 = 8°$ and reduced frequency $k = (\Omega L)/2U_\infty = 0.05$. Figure 4.1 shows the comparison of the lift coefficient of the steady aerofoil predicted by the present code with the measurements [18] and the numerical results from Riziotis et al. [17] and Xfoil [39]. It is observed that, for attached flow conditions ($2° < \alpha < 12°$), all the numerical codes give almost the same results, due to the use of the same closure relationships for the boundary layer equations. They overestimate slightly the lift coefficient, but the shift of the zero-lift angle of attack that appears in the experimental data suggests the presence of 3D effects in the measurements [17]. The present code, when compared with the other ones, provides smaller values of the lift for medium angles of attack, which makes its predictions closer to the experimental results. The underestimation of the lift with respect to the other codes is mainly due to some different simplifications used in the discretization of the wake, which lead to predict a smaller velocity at the trailing edge. Therefore, a larger diffusion occurs on the suction side which results in a thicker boundary layer. This

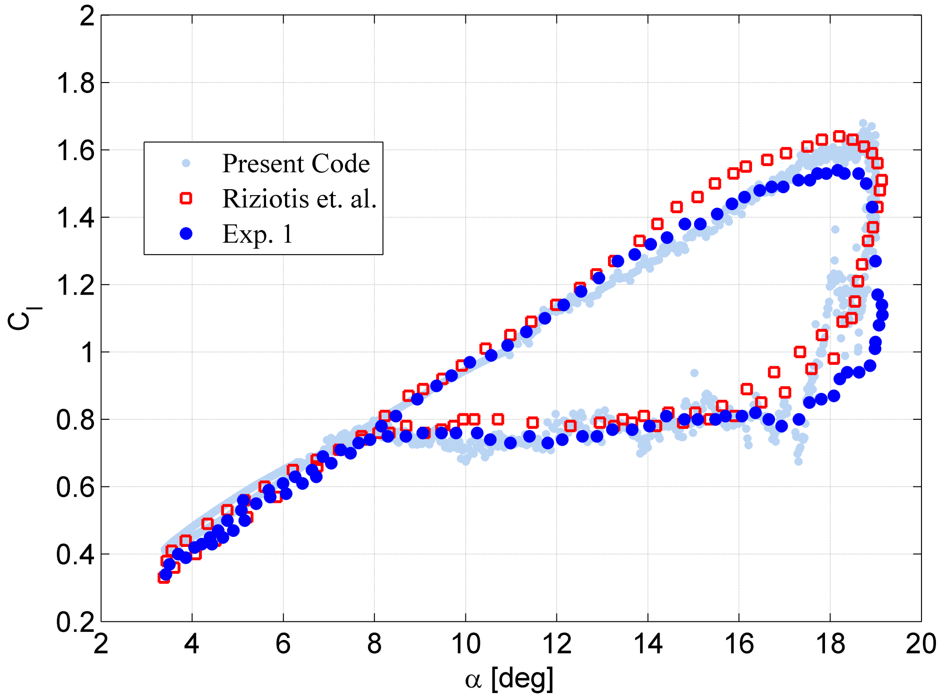

Figure 4.2: Lift coefficient vs. angle of attack for pitching aerofoil NACA 0015. $Re = 1.5 \times 10^6$, $\kappa = 0.05$.

increases the flow blockage and more fluid is moved towards the pressure side, which reduces the negative pressure peak on the suction side. This finally results in higher pressures on the suction side and hence in smaller lift coefficients. When the aerofoil stalls ($\alpha > 14$) the present results agree well with the experimental data, while, as expected, Xfoil (steady, single wake model) starts to fail.

Figure 4.2 shows the comparison of numerical predictions and measurements concerning the pitching aerofoil. The results of the present model are in good agreement with the experimental data, although they exhibit a slight overestimation of the lift for low angles of attack ($3° < \alpha < 8°$) and for high ones ($\alpha \approx 19°$). A small deviation in the shape of the C_l loop can be detected in the region close to the maximum pitching angle during the downstroke. Furthermore, the present numerical results exhibit some oscillations when the stall occurs. This is due to the displacement of the panel in the separation wake, which is not continuous but "jumps" from one panel node to another one. A local remeshing scheme is implemented to reduce the length of this "jump", but

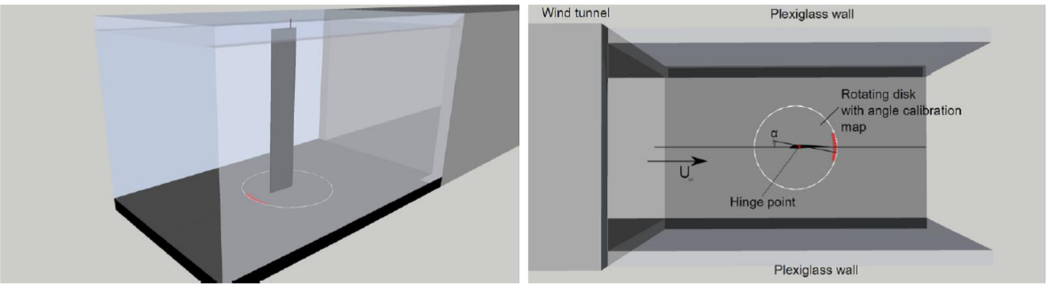

(a) (b)

Figure 4.3: Jet section of the wind tunnel. (a) 3D view and (b) top view of the blade in the test section.

a smoother approach should be used, the development of which is currently in progress.

4.2 Naca 0012, comparison with time-resolved 2D PIV data

Before presenting the data analysis, a brief description of the experimental setup is reported. The PIV measurements are used to validate the numerical model results for the aerofoil in steady and pitching motion for two reduced frequencies ($\kappa = 0.05$ and $\kappa = 0.15$).

At present, the large amount of PIV data acquired have been only partially processed. Data concerning other reduced frequencies and *Reynolds* numbers will be useful in a future extension of the present work to perform a more extensive analysis of the influence of the reduced frequency and *Reynolds* number on the phenomenology of the dynamic stall.

4.2.1 Wind Tunnel facility

PIV measurements were carried out at the open jet M-tunnel of the High Speed Laboratory of the faculty of Aerospace Engineering at the TU Delft. The jet section has an area of $0.16m^2$ ($0.40m \times 0.40m$) and it is extended by a transparent box to allow optical access (Fig. 4.3). The driving mechanism for the pitching motion is the Maxon DC RE 35 Motor, which produces a deviation of less than 2% with respect to the pure sinusoidal motion. The tunnel, equipped with an axial flow fan, operates with a flow velocity, measured by a pitot tube, between 3 and $30m/s$. The turbulence intensity, measured by

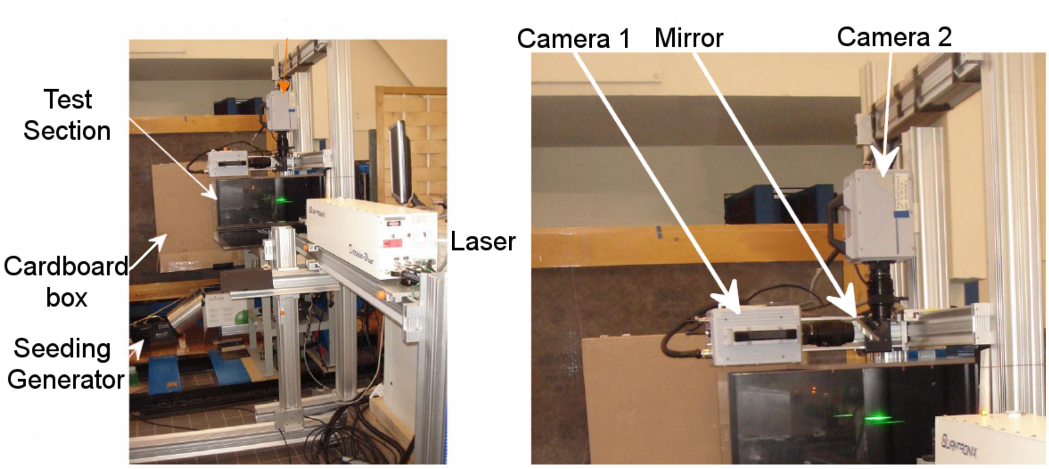

Figure 4.4: Camera and laser setup for PIV measurements.

a hot wire anemometer placed in the centre of the test section, is less than 0.2%. During the experiments the flow velocity was set at 7.56 ± 0.04 m/s in order to obtain $Re \approx 5 \times 10^4$. The investigation was performed on both sides of a 0.1 m chord NACA 0012 aerofoil (2D geometric blockage $\approx$ 8.5%). It was made of plexiglass and it was positioned vertically (see Fig. 4.3) to provide the optical access required by the PIV technique.

The seeding particles injected into the test section were $1\mu m$ water-based fog droplets, produced by a Safex twin-fog "Double Power" fog generator. They were added to the tunnel airstream through a cardboard box, which allowed their uniform distribution over the test section. Since the experiments were performed using ambient air, the particle response time was estimated to be about $3.1\mu s$. In the test section the particles were illuminated by a Quantronix Darwin Duo dual oscillator, single head Nd:YLF laser. The laser light is emitted at $527nm$ wavelength and each pulse has a duration of $200ns$ and an energy of $25mJ$ at 1 kHz. The light scattered by the seeding particles is captured by two Photron Fast CAM SA1 cameras with a sensor size of 1024×1024 pixel at $5.4kHz$. The pixel size is $20\mu m$. The data acquisition was performed by a DaVis software (LaVision GmbH) and data were processed by using commercial software PivView (PIVTEC GmbH).

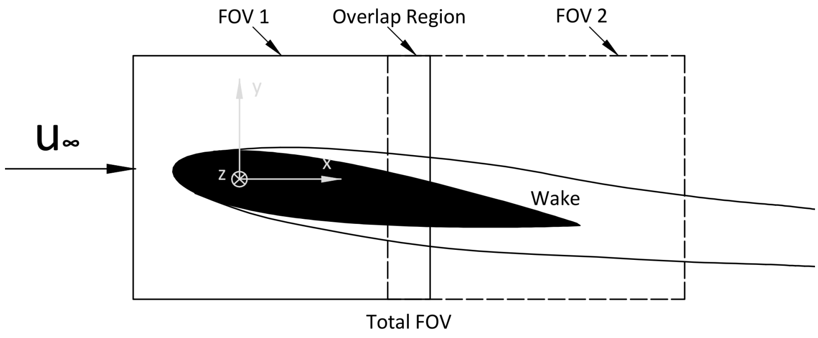

Figure 4.5: Field of view of the two cameras

$\alpha[deg]$	$U_{\infty}[m/s]$	$f_{acq.}[Hz]$	$\triangle t_{acq.}[s]$	$Reynolds$
6	7.56	2700	1	50000
10	7.56	2700	1	50000
12	7.56	2700	1	50000
14	7.56	2700	1	50000
17	7.56	2700	1	50000
20	7.56	2700	1	50000

Table 4.1: Steady aerofoil tests

4.2.2 PIV optical arrangement

In order to satisfy both the requirement of high spatial resolution and full field of view, two cameras with $105mm$ lens were used. These cameras were mounted on the top of the aerofoil as shown in figure 4.4. A mirror was used to allow camera 1 to detect the left part of the field of view, i.e., FOV1 in fig. 4.5. Camera 2 was placed vertically along the span of the aerofoil and it covered the right part of the field of view, FOV2. In this way the full field of view was covered with a 5% overlap of the two windows. During the experiments a plate covered with millimeter paper was used to align the cameras with the laser sheet and to obtain the same magnification factor for both cameras. This target allowed also the camera views to be aligned each other with a minimal overlap in order to cover all the desired field of view.

4.2.3 Overview of the PIV data collected

The summary of the steady aerofoil tests are presented in table 4.1.

k	$\alpha_{min}[deg]$	$\alpha_{max}[deg]$	$U_\infty[m/s]$	$f_{acq.}[Hz]$	$\triangle t_{acq.}[s]$	$Reynolds$
0.15	6	20	7.56	2700	1	50000
0.15	6	20	7.56	1000	2.7	50000
0.13	6	20	7.56	2700	1	50000
0.1	6	20	7.56	2700	1	50000
0.1	6	20	7.56	500	5.4	50000
0.1	6	20	15.11	2700	1	100000
0.1	6	20	15.11	1000	2.7	100000
0.1	6	20	15.11	500	5.4	100000
0.05	6	20	7.56	2700	1	50000

Table 4.2: Pitching tests

Table 4.2 shows a summary of the pitching motion tests.

4.2.4 Load estimation from the time-resolved 2D-PIV data

Theoretical background

Consider an arbitrary time-dependent control volume, $V(t)$ in Fig. 4.6, enclosed externally by surface $S(t)$ and internally by body surface $S_b(t)$. The forces acting on the body are obtained by the momentum integral equation:

$$\begin{aligned}\frac{\bar{F}}{\rho} = &-\frac{d}{dt}\int_{V(t)} \bar{u}\, dV \\ &+ \oint_{S(t)} \bar{n}\cdot\left[-\frac{p}{\rho}\bar{I} - (\bar{u}-\bar{u}_s)\bar{u} + \bar{T}\right] dS \\ &- \oint_{S_b(t)} \bar{n}\cdot(\bar{u}-\bar{u}_s)\bar{u}\, dS\end{aligned} \tag{4.1}$$

where:

- $\bar{n}$ is the unit vector normal to the control surface
- $\bar{I}$ is the unit tensor
- $\bar{T}$ is the viscous stress tensor
- $\bar{u}_s$ is the velocity of the boundary surface

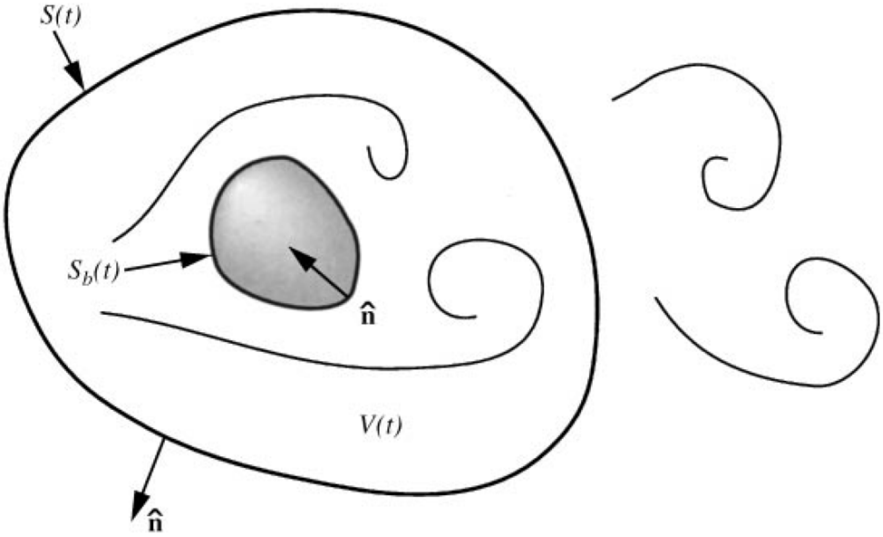

Figure 4.6: Integration domain for the evaluation of fluid-dynamic forces

Thus, the fluid forces can be obtained when the velocity field in the control volume and the pressure distribution on the boundary surface are known. The application of eq.(4.1) to the PIV experimental data presents two main difficulties:

- The velocity field should be determined also in the boundary layer, which is not usually feasible or accurate enough.
- The pressure distribution on the boundaries is unknown, and it should be reconstructed a posteriori from the velocity field.

In the last years the determination of the pressure field from PIV measurements has been explored and different approaches have been developed [48]. Anyhow, further efforts are necessary to fully understand the impact of some approximations made in those models and to single out the parameters that actually determine the success of the pressure evaluation. For this reason, instead of considering the pressure reconstruction, the forces have been evaluated by using the “flux” equation derived by Noca et al. [49] for incompressible flow:

$$\begin{aligned}\frac{\bar{F}}{\rho} &= \oint_{S(t)} \bar{n}\cdot\gamma_{flux}\; dS \\ &\quad - \oint_{S_b(t)} \bar{n}\cdot(\bar{u}-\bar{u}_s)\;\bar{u}\; dS - \frac{d}{dt}\oint_{S_b(t)} \bar{n}\cdot(\bar{u}\bar{x})\; dS\end{aligned} \tag{4.2}$$

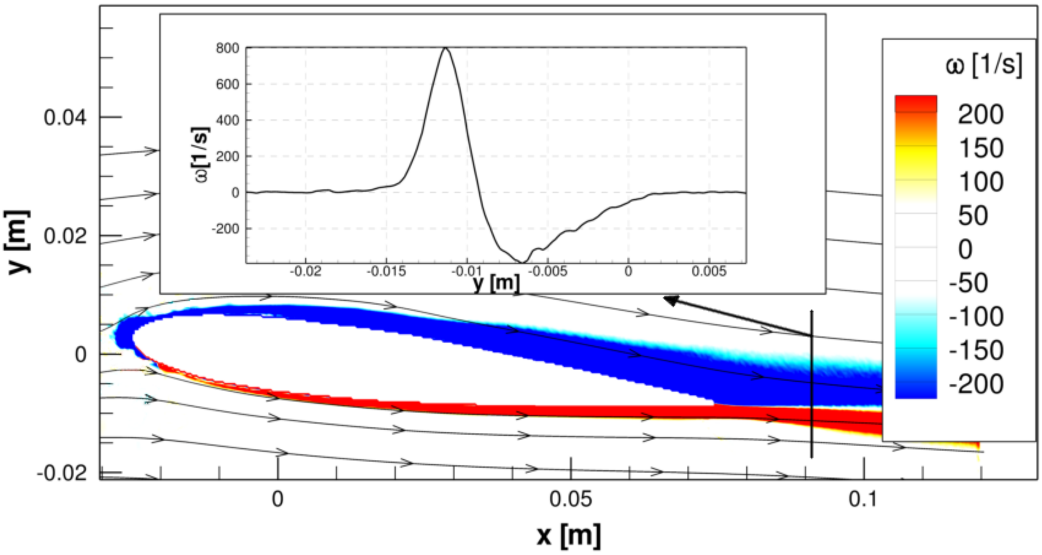

Figure 4.7: PIV mean vorticity field. NACA 0012 aerofoil, $\alpha = 6°$.

where $\bar{x}$ is the position vector and the flux term is:

$$\begin{aligned}\gamma_{flux} =& \frac{1}{2}u^2\bar{I} - \bar{u}\bar{u} - \frac{1}{Dim-1}\bar{u}(\bar{x}\times\bar{\omega}) + \frac{1}{Dim-1}\bar{\omega}(\bar{x}\times\bar{u}) \\ & - \frac{1}{Dim-1}\left[\left(\bar{x}\cdot\frac{\partial\bar{u}}{\partial t}\right)\bar{I} - \bar{x}\frac{\partial\bar{u}}{\partial t} + (Dim-1)\frac{\partial\bar{u}}{\partial t}\bar{x}\right] \\ & + \frac{1}{Dim-1}\left[\bar{x}\cdot\left(\nabla\cdot\bar{T}\right)\bar{I} - \bar{x}\left(\nabla\cdot\bar{T}\right)\right] + \bar{T}\end{aligned} \tag{4.3}$$

Dim being the dimension of the space. This formulation of the momentum equation requires the knowledge of the velocity and its derivatives only on the boundary of the control volume. The use of PIV data to evaluate eq. 4.2 is rather straightforward because the second integral on the right hand-side vanishes while the third one is known by the aerofoil motion law. Therefore, an accurate evaluation of the flow velocity very close to the body surface, difficult when using the PIV technique, is not required.

Application to the present PIV time-resolved data

The elimination of the pressure term in the eq. 4.1 causes the appearance of vorticity ω in eq. 4.2, which represents a source of error for two main reasons:

- If the wake is thin, the relative coarseness of the measurement grid coupled with the asymptotic variation of the vorticity could produce a significant integration error.

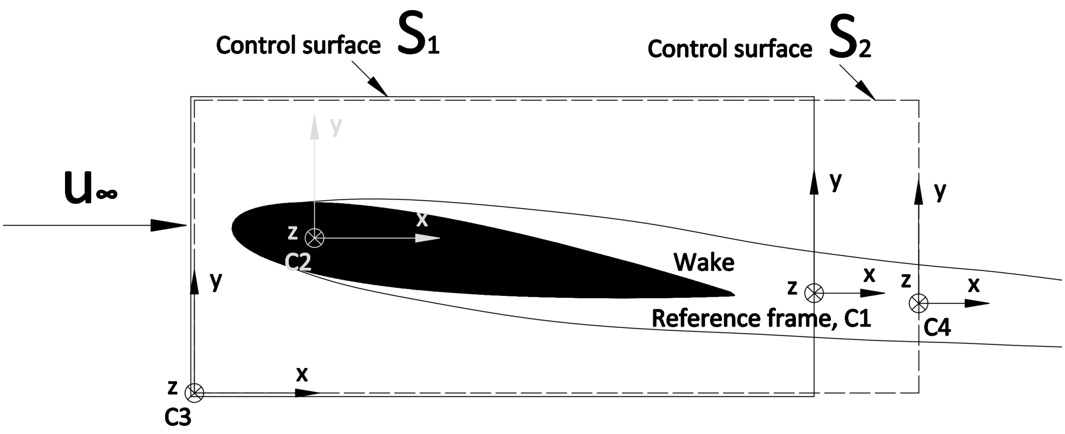

Figure 4.8: Control surfaces and reference frames for forces evaluation

	C_1	C_2	C_3	C_4
S_1	0%	-4%	-5.7 %	1%
S_2	1.5%	5%	6.5 %	0.7%

Table 4.3: Per cent deviations of the lift coefficient for $\alpha = 6°$

- The implicit averaging of the flow field due to the interrogation windows of the PIV technique could lead to a measurement error.

These difficulties can be overcome by placing the origin of the reference frame in the point where the evaluation of the vorticity from the PIV data is more problematic, namely, in the middle of the wake. At this position, the vorticity exhibits a negative and a positive peak, and $|d\omega/dS|$ is maximum (see fig 4.7). Putting the origin of the reference frame in this point reduces the influence of the wake vorticity distribution on the forces evaluation, because the contribution of the vorticity to γ_{flux} depends on the distance from the origin, as shown by terms $\bar{x} \times \bar{\omega}$ and $\bar{\omega}\,(\bar{x} \times \bar{u})$ in eq.(4.3). Other geometric parameters that can affect the accuracy of the forces extraction from PIV velocity fields are the shape and size of the control volume. In order to quantify the influence of these parameters, a comparison was performed between the forces computed by using two different control volumes (S_1 and S_2 in Fig. 4.8) and four different reference frames (C_1, C_2, C_3 and C_4). Table 4.3 shows the deviations of the lift coefficient for $\alpha = 6°$ from the reference value obtained for S_1 and C_1.

When the origin of the reference frame is placed on the point where $|d\omega/dS|$ is maximum (values highlighted in Tab. 4.3) the influence of the control volume size on the lift coefficient is negligible (a deviation of 0.7% is observed in Tab. 4.3). On the contrary, when the origin is far from the wake (C_2 and C_3) the contribution of the wake vorticity on the forces increases and deviations of 10% or larger are observed when changing the control surface.

The above observations confirm that the way the vorticity is evaluated influences considerably the computation of forces acting on the aerofoil. Therefore in order to reduce such an influence, the forces extracted from the PIV data that will be presented in the next section are computed by applying eqs. (4.2) and (4.3) to control surface S_1 in reference frame C_1, as depicted in Fig. 4.8.

From Noca et al. [49] it is known that the extraction of the forces from time-resolved PIV velocity fields is usually affected by high-frequency noise (see Fig. 4.9). This problem, can be overcome by filtering the signal with a 5th order Butterworth scheme and a cut-off frequency about ten times higher than the principal harmonic of the flow ([49], see Fig. 4.10). The same approach will be used in the following sections.

As an example, Fig. 4.11 shows the unfiltered data for the pitching aerofoil at $\kappa = 0.15$. The associated power spectrum of the signal is given in Fig. 4.12. The main peak is found at 3.71 Hz, which corresponds to the forcing frequency i.e., the aerofoil pitching frequency (3.67 Hz). The secondary peaks occurring between 10 and 20 Hz are due to the shedding of large vortical structures during the dynamic stall. Therefore, in the present application, the cut-off frequency of the low-pass filter was set at 100 Hz, well above the principal harmonics of the flow. After the signal has been filtered, it needs to be rephased. The delay is computed by performing a cross-correlation with the original signal (Fig. 4.13). The final result is shown in Fig. 4.14.

4.2.5 Steady Aerofoil Results

In this section the predictions for a steady aerofoil at $Re = 5 \times 10^4$ are presented. At this *Reynolds* number the Prandtl assumptions are at the limit of their validity range. However, this case was chosen because the PIV phase-locked measurements and the CFD-DES simulations for the VAWT were carried out at this *Reynolds* number [19]. Figure 4.15 shows the comparison between the numerical predictions and the PIV mean vorticity field for $\alpha = 12^\circ$. The position and shape of the separation shear layer are well predicted although the separation point appears slightly closer to the leading edge. At the trailing edge the predicted shed vorticity does not leave straight the aerofoil and the reason of that is probably related to the slightly different vorticity distribution in the separated flow region. The vorticity predicted between the two shear layers

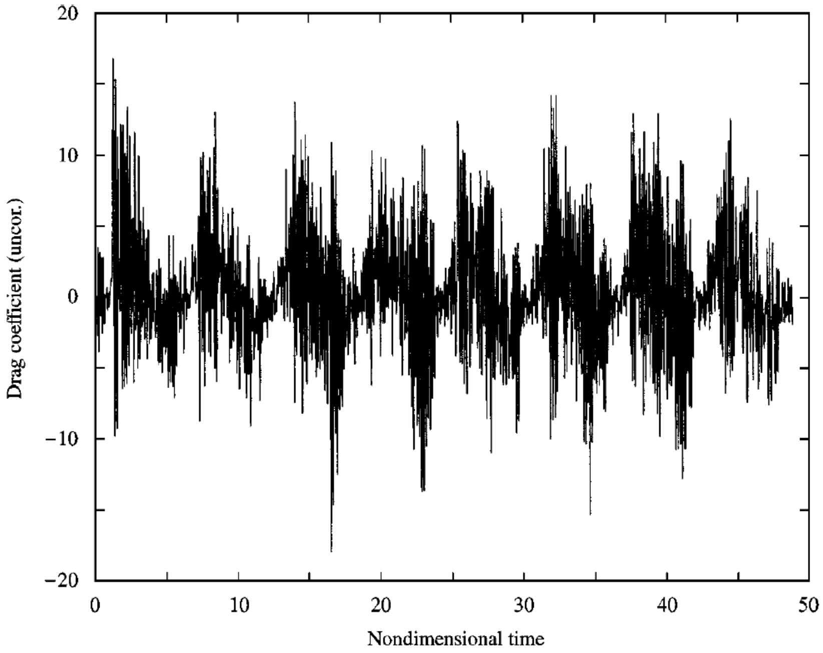

Figure 4.9: Unfiltered drag coefficient of a cylinder [49]

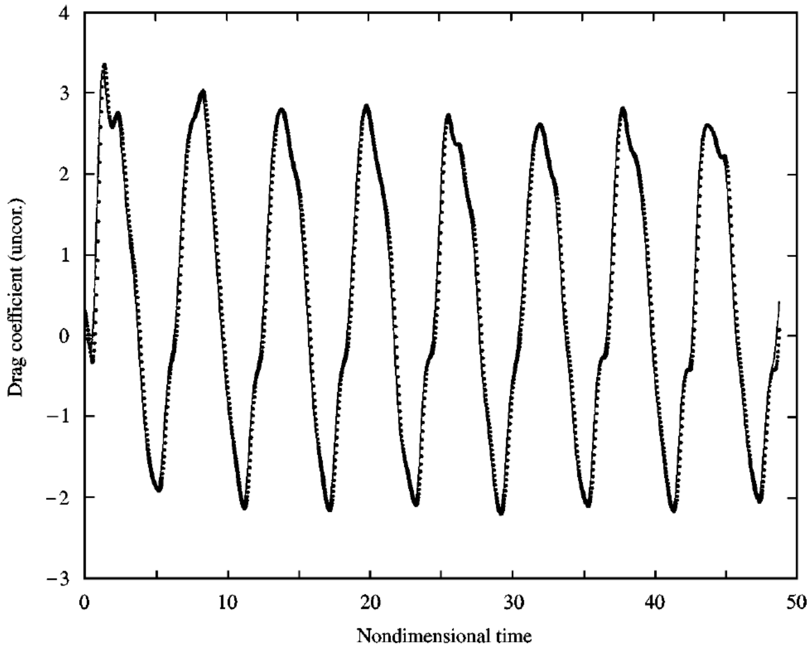

Figure 4.10: Drag coefficient of a cylinder filtered by a 5th order Butterworth scheme with a cut-off frequency ten times higher than the principal harmonic [49]

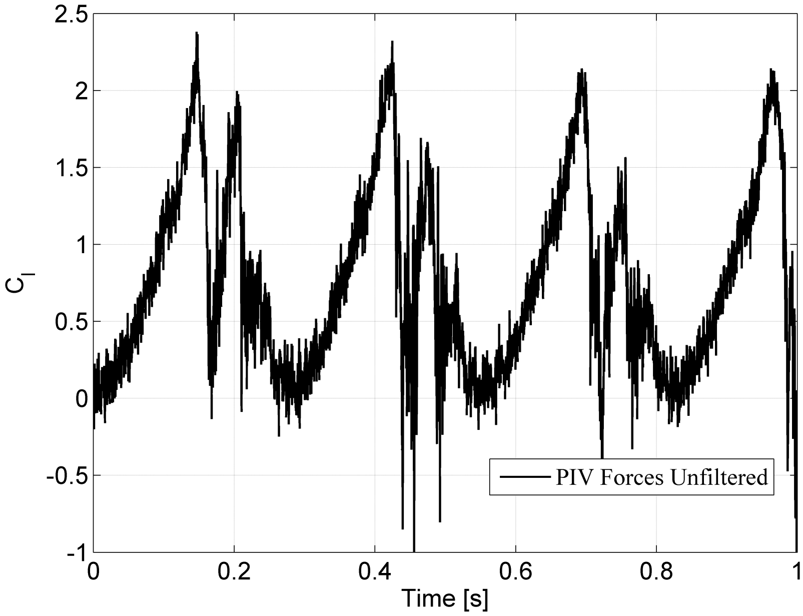

Figure 4.11: Unfiltered lift coefficient of a pitching aerofoil for $\kappa = 0.15$

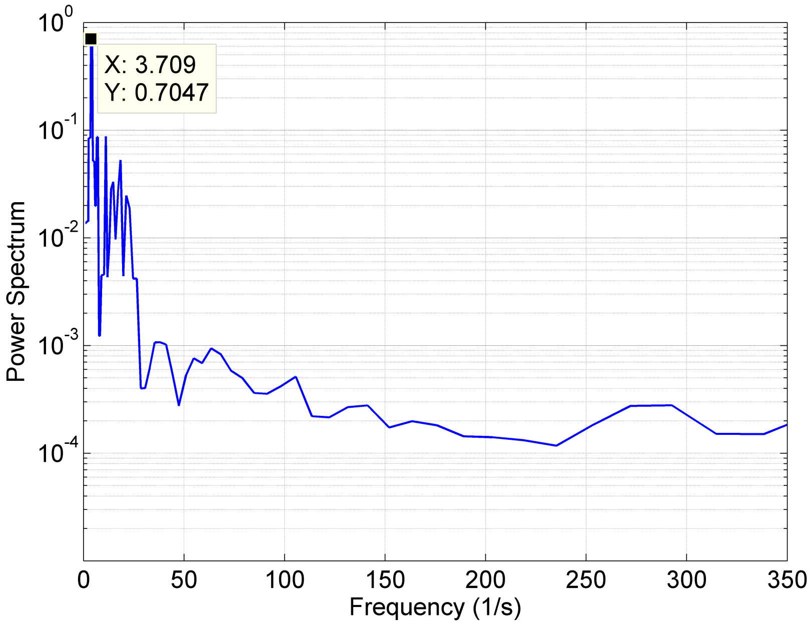

Figure 4.12: Power spectrum of the signal in Fig. 4.11

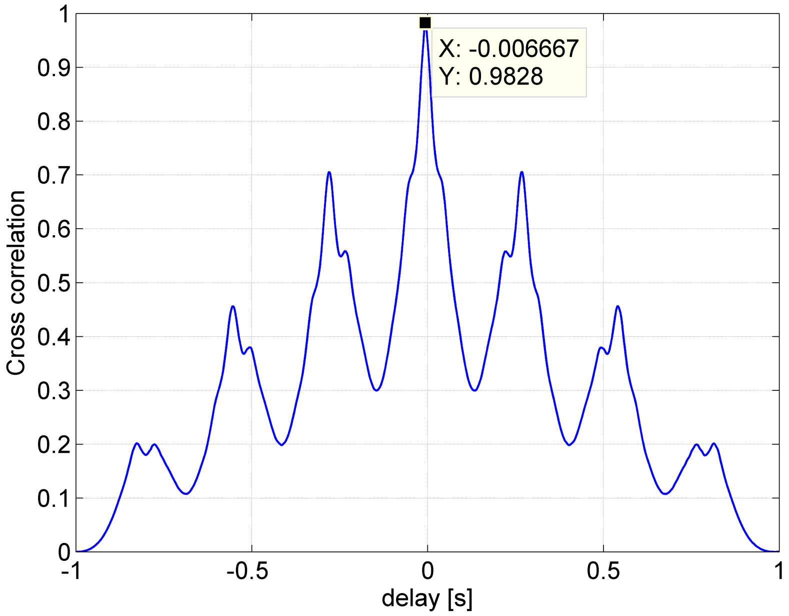

Figure 4.13: Results of the cross-correlation of the signal in Fig. 4.11 with its filtered counterpart

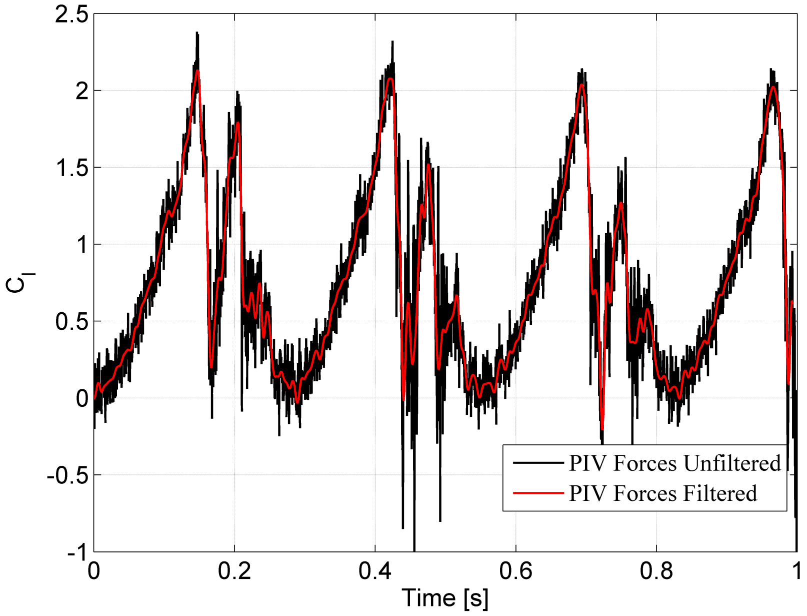

Figure 4.14: Filtered and unfiltered lift coefficient from the PIV data

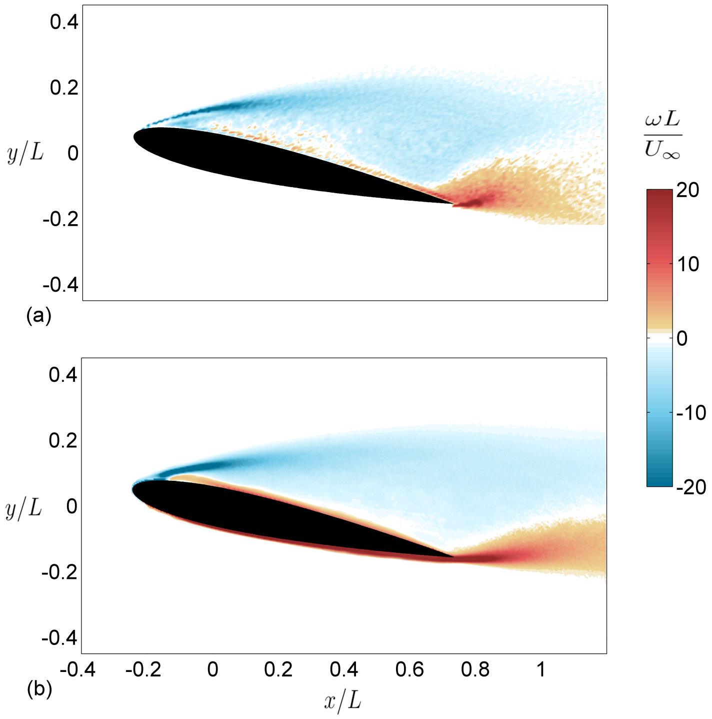

Figure 4.15: Mean vorticity field, a) Vortex panel model b) PIV data

should be more spread, indeed several zero-vorticity spots are present. This is due to the use of the vortex blobs to model the vorticity shedding, and thus it cannot be considered as an error.

Figure 4.16 shows the comparison of the lift coefficient predicted by the present model with the results of Xfoil [39] and the experimental values obtained from the integration of the PIV velocity field. The present code is able to capture the trend of the lift coefficient also in deep stall conditions but it exhibits a constant shift with respect to the experimental results. This could be due to the low *Reynolds* number, really in the edge of the Prandtl assumptions, or to three dimensional effects on the measurements.

Furthermore, it has to be mentioned that the experimental C_l in Fig. 4.16 is referred to the geometric angle of attack, no wind tunnel correction having been applied to that angle. A preliminary analysis suggests that the geometric angle of attack, in the wind tunnel, should be reduced to make the measurements comparable with the solution in an unbounded flow field. In particular, the predicted and measured laminar separation positions, laminar to turbulent transition points and velocity fields turn out to agree well if the experimental geometric angle of attack is reduced according to the wind tunnel correction.

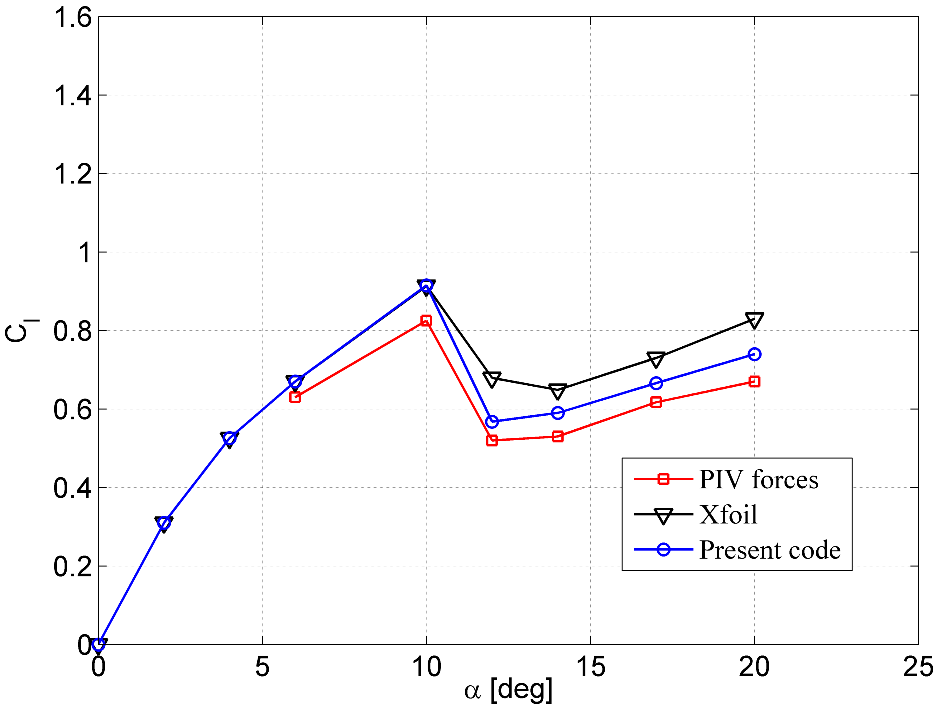

Figure 4.16: Comparison of the lift coefficients predicted by the present model with the numerical results of Xfoil and the forces extracted from the measured flow. Steady flow past a NACA 0012 aerofoil, $Re = 5 \times 10^4$.

This is a well-known occurrence, but the estimation of the proper correction is not straightforward, especially for the aerofoil in pitching motion. On the other hand, its impact on the results of the present work is not significant enough to justify an additional effort.

4.2.6 Pitching aerofoil results, low reduced frequency

In this section the analysis of the results for the aerofoil in pitching motion with reduced frequency $\kappa = 0.05$ and $Re = 5 \times 10^4$ is presented. Figure 4.17 shows the comparison of the forces extracted from the PIV velocity fields with the model predictions for a single complete oscillation which is representative of the mean behaviour. Due to the low *Reynolds* number the evolution of the vorticity (see, e.g., Fig. 4.18) shows concentrations of strong vortices on the aerofoil suction side, which are responsible for the temporary oscillations of the lift coefficient.

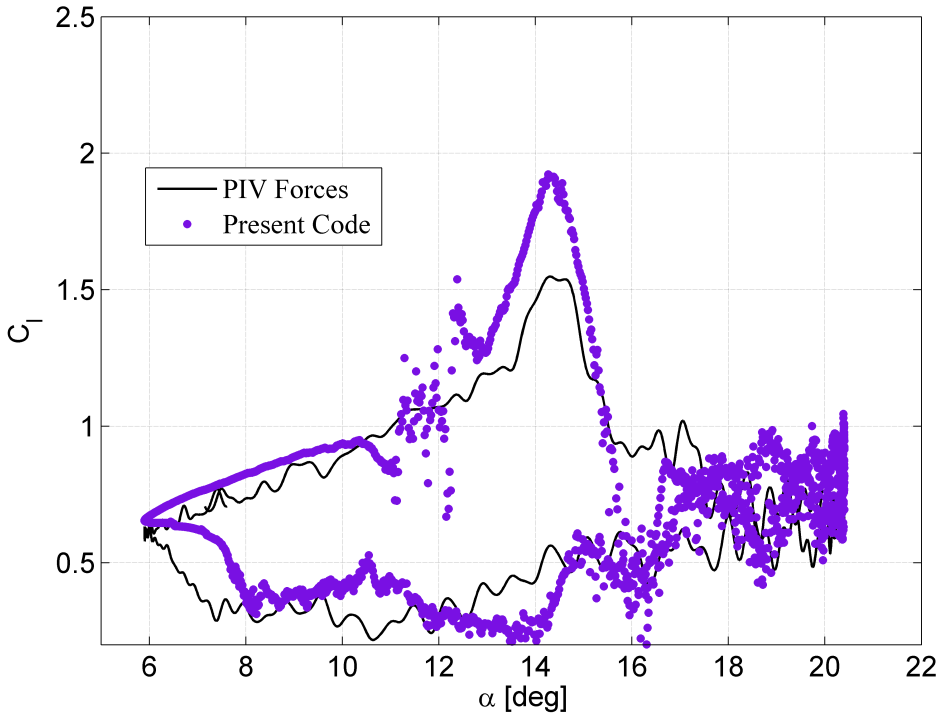

Figure 4.17: Pitching motion results for a NACA 0012 aerofoil at $Re = 5 \times 10^4$ and $\kappa = 0.05$. Comparison of the predicted lift coefficients with the forces extracted from the PIV velocity fields.

As in the steady case, in the last part of the downstroke motion ($6^\circ < \alpha < 7^\circ$) and in the first part of the upstroke ($6^\circ < \alpha < 11^\circ$) the model overestimates slightly the lift coefficient. At about $\alpha = 12^\circ$ the flow separation starts from the leading edge and a dynamic vortex begins to grow while the flow keeps on reattaching on the suction side after the vortical bubble. This induces an "overshoot" in the lift ($12^\circ < \alpha < 15^\circ$) till the detachment of the vortex is complete [47]. The present model is able to capture this behaviour, with some problems in the early stage, where the "jump" of the separation position to the leading edge causes some oscillations in the forces (see sec. 4.1 for details). Also, the model overestimates the maximum lift coefficient, which is due to the larger size and the different shape of the predicted leading edge vortex. This difference can be clearly observed in fig. 4.19 and, in the author's opinion, it can be ascribed to an imperfect modelling of the viscous part of the flow. In the present model, as discussed in sec. 2.1.2, the circulation released in the separation point is computed by assuming that all the vorticity contained

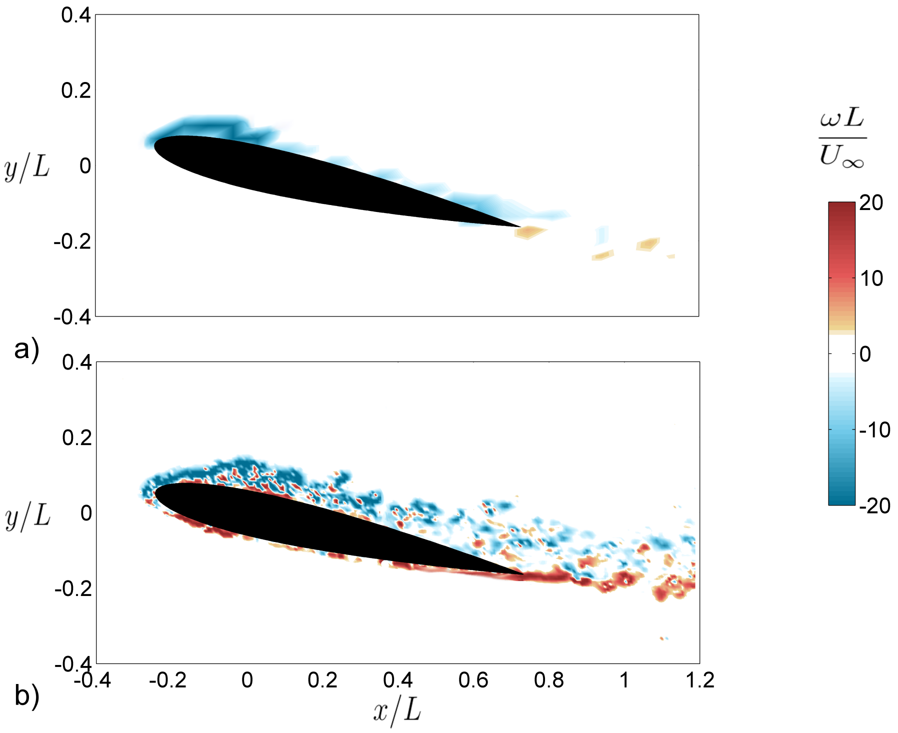

Figure 4.18: Instantaneous vorticity field during pitching motion. Vortex panel model (a) Vs. PIV (b) results. $\alpha = 12.6°$ upstroke, $\kappa = 0.05$.

in the boundary layer is injected into the inviscid flow field. This is usually a reasonable assumption, but especially when an abrupt separation occurs there are evidences that only part of the vorticity at the separation point is discharged into the inviscid flow [15].

Another reason of the difference in the vortex size and shape can be ascribed to the predominant role of three dimensional effects in the first stage of separation. In fact, in the real flow the instability that triggers the leading edge vortex does not act uniformly on the blade span, so that the separation does not start simultaneously along the blade. When the separation begins at some position the lift (and hence the circulation) of that section increases (the "overshoot"), and from Kelvin's theorem a circulation is shed from the trailing edge. According to the Helmholtz second theorem *(a vortex filament cannot end in a fluid; it must extend to the boundaries of the fluid or form a closed path)*, if the lift of a blade section increases while remaining unchanged in the adjacent section, where the flow is still attached, a vorticity orthogonal to the blade span should be shed. This induces a "downwash" (as at the tip of a wing) that causes the propagation of the separation, deforms the leading edge vortex

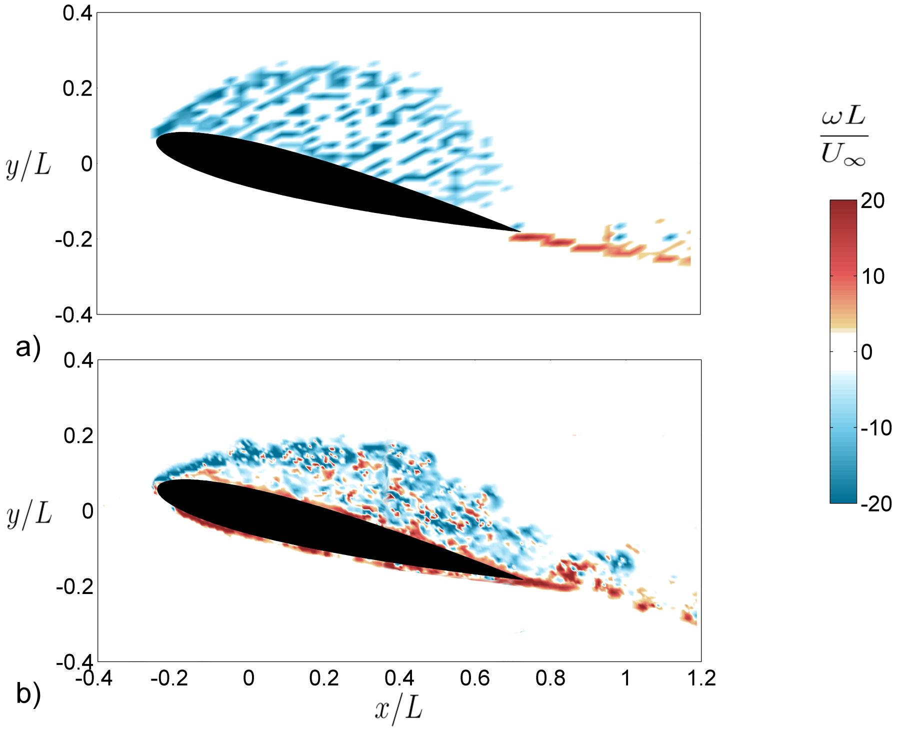

Figure 4.19: Instantaneous vorticity field during pitching motion. Vortex panel model (a) Vs. PIV (b) results. $\alpha = 14°$ upstroke, $\kappa = 0.05$.

and pushes it on the aerofoil surface. In other words, the 2D assumption is valid as far as the spanwise distribution of the lift is uniform, which is not the case at the beginning of the separation process where three dimensional effects may occur according to the Helmholtz second theorem.

After the shedding of the dynamic vortex, when the blade is fully stalled, the lift along the span can be reasonably assumed constant, so that the 2D approach produces again good predictions. It is also true that the difference in the vortex shape could be ascribed to wind tunnel effects.

The flow reattachment during downstroke ($8° < \alpha < 12°$) is correctly predicted, but it seems to end slightly earlier in the simulation ($\alpha \approx 8°$) than in the PIV measurement ($\alpha \approx 7.5°$). This is probably due to the discrete movement of the separation panel and, therefore, better results should be obtained with the smoothing procedure under development.

The main feature of the pitching motion is the formation and release of the leading edge vortex, which plays a fundamental role also in the VAWT aerodynamics. Since the numerical model should be able to capture this phenomenon, it is worth while to compare the predicted vortex evolution with the experimen-

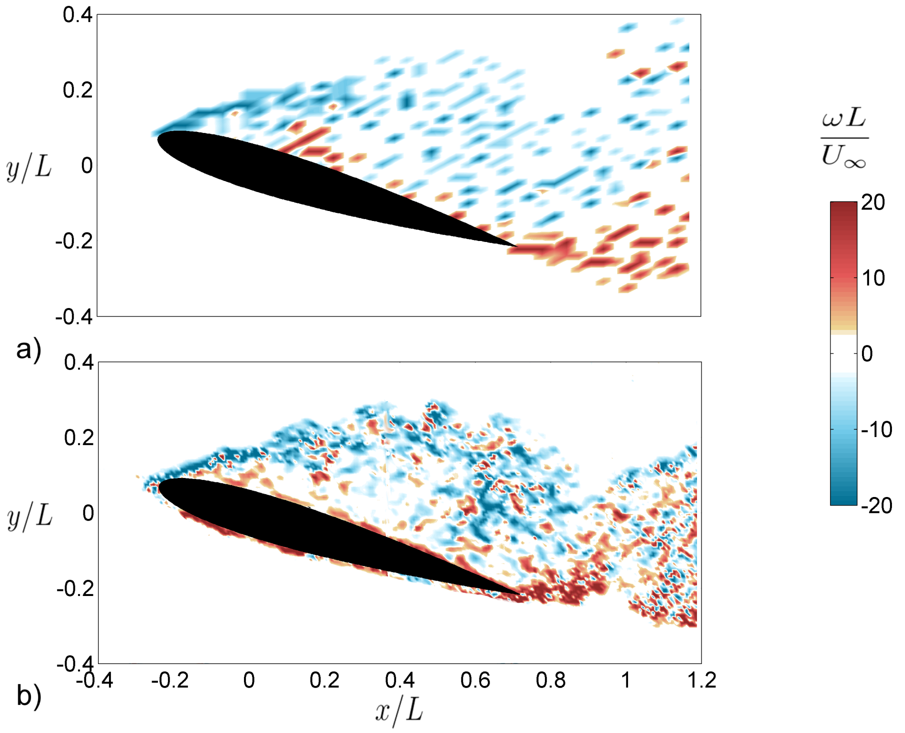

Figure 4.20: Instantaneous vorticity field during pitching motion. Vortex panel model (a) Vs. PIV (b) results. $\alpha = 16.8°$ upstroke, $\kappa = 0.05$.

tal results. From fig. 4.18 showing the vorticity field at the beginning of the separation, it can be observed that the formation of the dynamic vortex is well predicted by the present code. In fig. 4.19 the leading edge vortex reaches its maximum size and, as explained above, the different vortex shape predicted by the model is probably due to an imperfect modelling of the viscous part of the flow and to three dimensional effects. After the vortex has been shed, a fully separated flow is established, which is predicted in good agreement with the PIV experimental data (fig. 4.20).

4.2.7 Pitching aerofoil results, high reduced frequency

In this section the results for the aerofoil in pitching motion with reduced frequency $\kappa = 0.15$ and $Re = 5 \times 10^4$ are presented. Figure 4.21 shows the comparison of the forces extracted from the PIV velocity fields with the model predictions for a single complete oscillation, which is yet representative of the mean behaviour. Also in this case, due to the concentration of strong vortices on the aerofoil suction side (see, e.g., Fig. 4.22), there are temporary

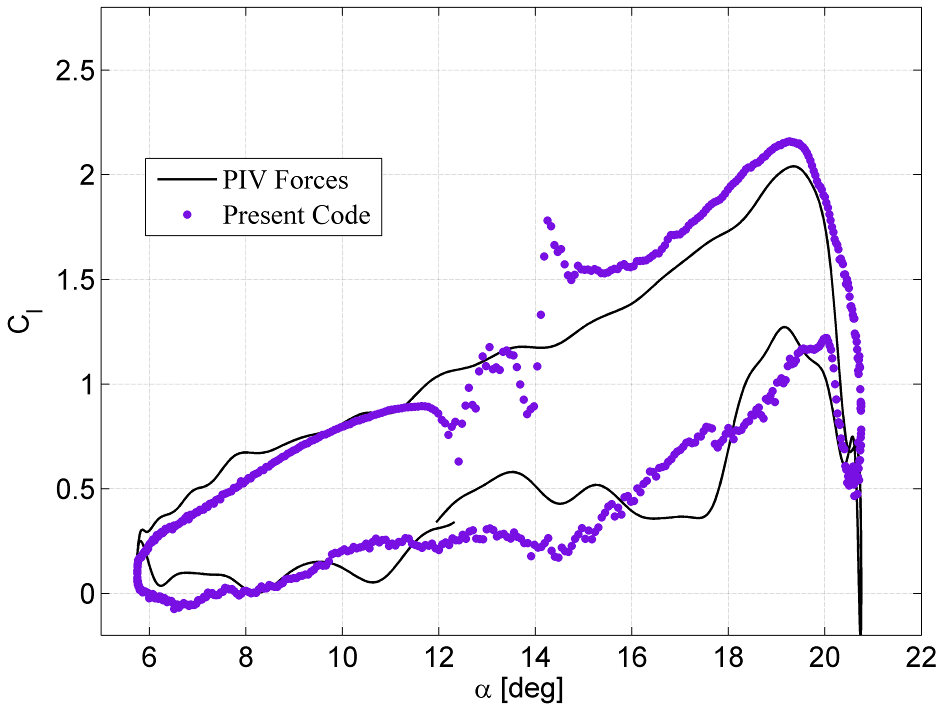

Figure 4.21: Pitching motion results for a NACA 0012 aerofoil at $Re = 5 \times 10^4$ $\kappa = 0.15$. Comparison of the predicted lift coefficients with the forces extracted from the PIV velocity fields.

oscillations of the lift coefficient.

In this case the model underestimates slightly the lift coefficient in the last part of the downstroke motion ($6° < \theta < 10°$) and in the first part of the upstroke ($6° < \theta < 9°$). At about $\alpha = 13°$ the flow separation starts from the leading edge and the dynamic vortex begins to grow while the flow keeps on reattaching on the suction side after the vortical bubble. For this reduced frequency the "overshoot" ends at $\alpha = 19.6°$ when the detachment of the leading edge vortex starts. Also in this situation the present model is able to properly reproduce the "overshoot", with some problems in the early stage, when (as for $\kappa = 0.05$) the "jump" of the separation position to the leading edge causes some oscillations in the forces (see sec. 4.1 for details). The maximum lift coefficient (at $\alpha = 19.6°$) is well predicted, better than in the previous situation ($\kappa = 0.05$, sec. 4.2.6). To investigate the reasons for this better agreement it is interesting to compare the vorticity fields of the two solutions ($\kappa = 0.05$ and $\kappa = 0.15$) at the maximum lift position (Figs.

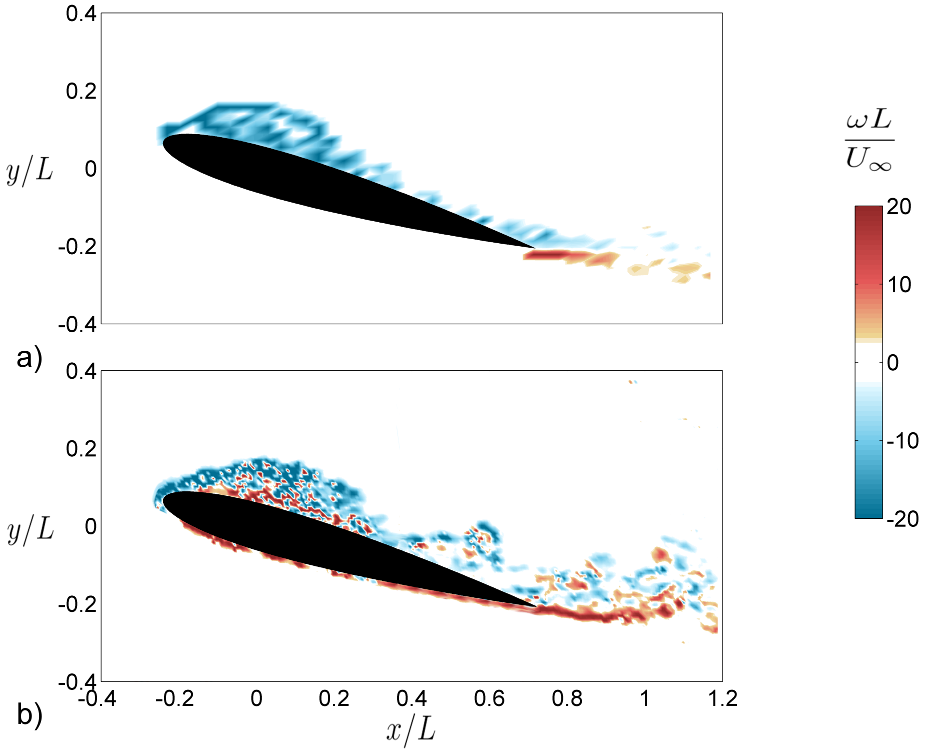

Figure 4.22: Instantaneous vorticity field during pitching motion. Vortex panel model (a) Vs. PIV (b) results. $\alpha = 16°$ upstroke, $\kappa = 0.15$.

4.19 and 4.23. For the higher reduced frequency the experimental data show that the rear part of the leading edge vortex is more lengthen and detached from the aerofoil suction side, probably due to the higher down speed of the surface. Therefore, the bigger vortical structure, partially detached from the aerofoil surface, induces higher lift coefficient. The same difference cannot be appreciated in the simulation results. The leading edge vortex, which is responsible for the "overshoot", has almost the same roundish shape in the two cases and its size is only slightly increased when changing from $\kappa = 0.05$ to $\kappa = 0.15$. Therefore, in the experimental results the size and shape of the leading edge vortex seem to be more sensitive to the aerofoil pitching frequency. The time required for the growth of the vortical structure is well predicted by the numerical model and for $\kappa = 0.05$ it is 10% longer than for $\kappa = 0.15$. The time period from the formation of the leading edge vortex to its shedding is then a weak function of the reduced frequency, probably because this phenomenon is mainly controlled by the flow convection, as for the vortical structures during the reattachment process (see sec. 3.3). A thorough analysis of this behaviour

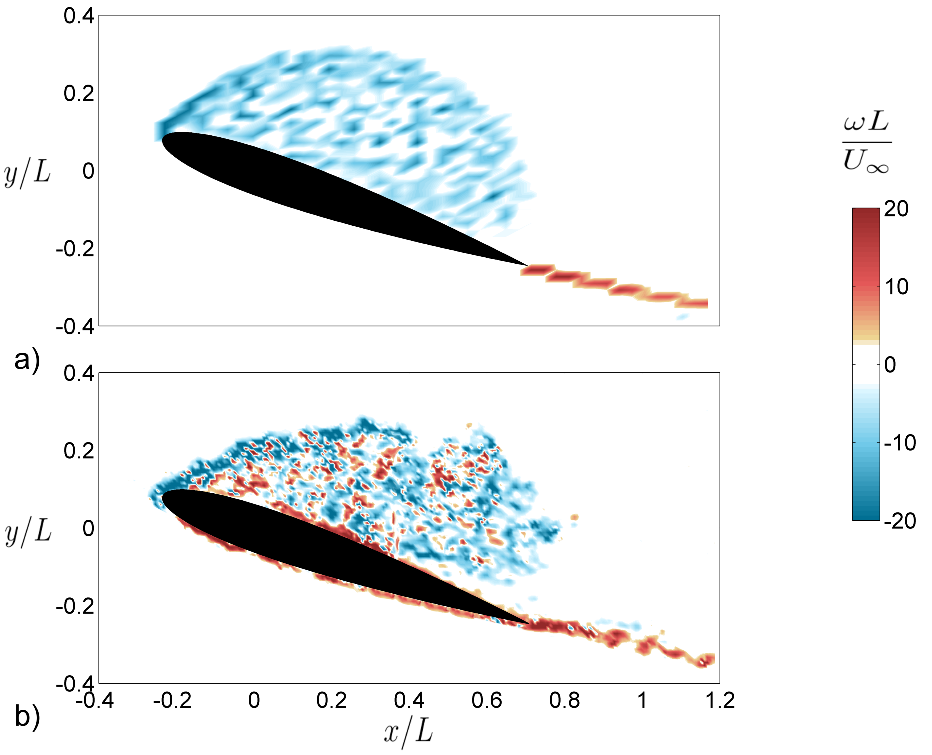

Figure 4.23: Instantaneous vorticity field during pitching motion. Vortex panel model (a) Vs. PIV (b) results. $\alpha = 19.2^\circ$ upstroke, $\kappa = 0.15$.

could be an interesting subject for a future research, since PIV data for $\kappa = 0.1$ and $\kappa = 0.13$ (collected by the author) are already available.

After the leading edge vortex has been shed ($\theta = 20^\circ$, upstroke) the lift coefficient reaches a relative minimum that is well predicted by the numerical model. In the downstroke part of the pitching motion, for $\kappa = 0.15$, the aerofoil is subjected to a weak "overshoot" due to the growth and shedding of a second leading edge vortex ($\theta = 19^\circ$), which is also well predicted by the present code.

As done for $\kappa = 0.05$, the predicted vortex evolution is compared with the experimental results. From Fig. 4.22 showing the vorticity field at the beginning of the separation, it can be observed that the formation of the dynamic vortex is well predicted by the present code. In Fig. 4.23 the leading edge vortex reaches its maximum size and the shedding starts. Then, the trailing edge vortex starts to roll up, Fig. 4.24, and the leading edge vortex is convected downstream. Figure 4.25 shows the reattachment of the leading edge vortex (downstroke, $\theta = 19^\circ$) after the shedding of the first vortical structure. It can be concluded that, also for the present reduced frequency, the model is

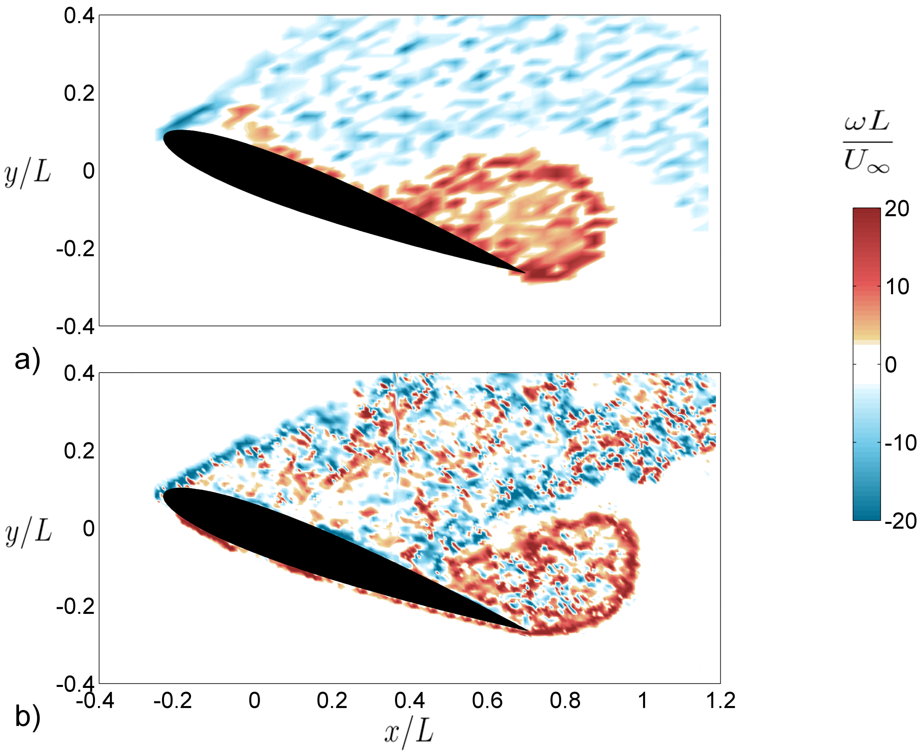

Figure 4.24: Instantaneous vorticity field during pitching motion. Vortex panel model (a) Vs. PIV (b) results. $\alpha = 20°$ upstroke, $\kappa = 0.15$.

capable of reproducing the formation and release of the leading edge vortices in excellent agreement with the experimental data.

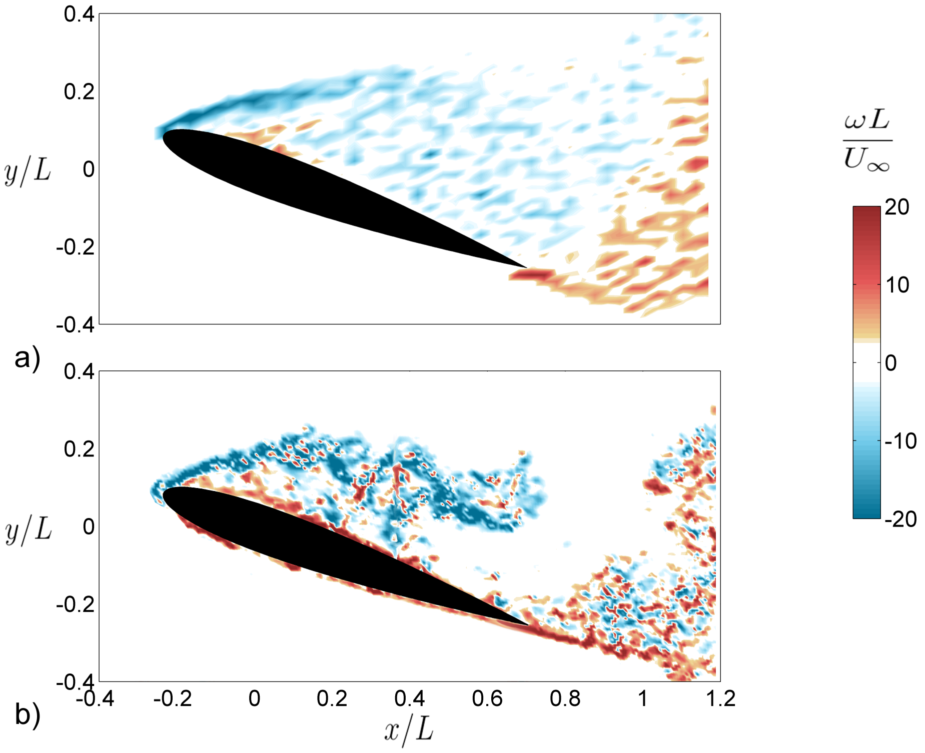

Figure 4.25: Instantaneous vorticity field during pitching motion. Vortex panel model (a) Vs. PIV (b) results. $\alpha = 19°$ downstroke, $\kappa = 0.15$.

5

Results

In this chapter the numerical code is used to study the aerodynamic behaviour of vertical axis wind turbines in dynamic stall. In this working condition, especially due to the wake-blade interaction, random load components occur, so that comparing integral values (such as power or forces) can mask cancellation errors [8]. To evaluate the accuracy of the present model in simulating the wake structure, predicted vorticity fields are computed with PIV phase-locked data (from [19]). Afterwards, the predicted forces are compared with CFD-DES results (from [16]). In the remaining sections the present model is used to investigate the influence of some parameters (number of blades, reduced frequency and dynamic stall) on VAWT performance. Nevertheless, the results presented in the next sections are not claimed to be an extensive study of the VAWT, but they are mainly aimed at showing the predictive capabilities and the opportunities provided by the present model.

5.1 Vertical Axis Wind Turbine

The results of the present model will be validated against the PIV and CFD data of Simão Ferreira et al. [19] [16] for a single blade VAWT, $\lambda = 2$, $\kappa = 0.125$, $Re = 5 \times 10^4$. In this condition the VAWT exhibits deep dynamic stall and the flow is characterized by the evolution and release of leading and trailing edge vortices (see Figs 5.1 and 5.3, PIV data, phase-locked average). The leading edge vortex starts to form when the separation occurs ($\theta \approx 72°$) and it grows on the suction side of the aerofoil. When $\theta \approx 90°$ its length reaches the chord size and it begins to move away from the surface under the influence of the trailing edge vortex that starts to roll up and to grow. At $\theta > 138°$ the leading edge vortex is released from the aerofoil due to the growth of the trailing edge vortex, and it is transported downstream by the flow.

The first step in the validation is to compare the predicted and measured vorticity distributions during the VAWT blade rotation. The larger difference

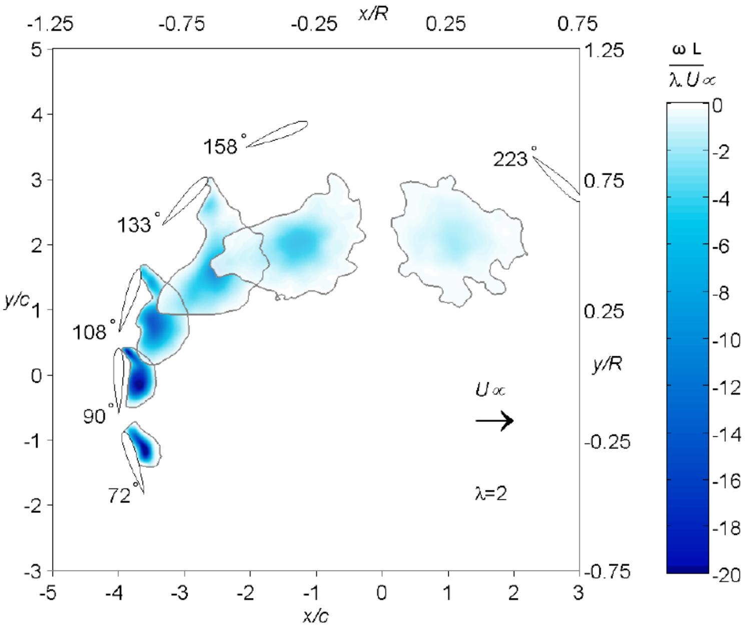

Figure 5.1: Evolution of the leading edge vortex for $\lambda = 2$, phase-locked average (PIV data from Ferreira et al. [19])

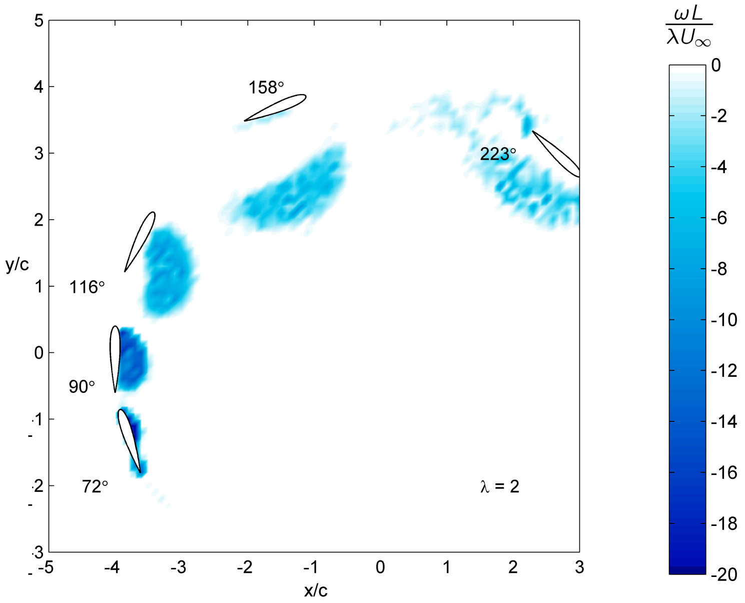

Figure 5.2: Evolution of the leading edge vortex for $\lambda = 2$, phase locked average (vortex model, double wake)

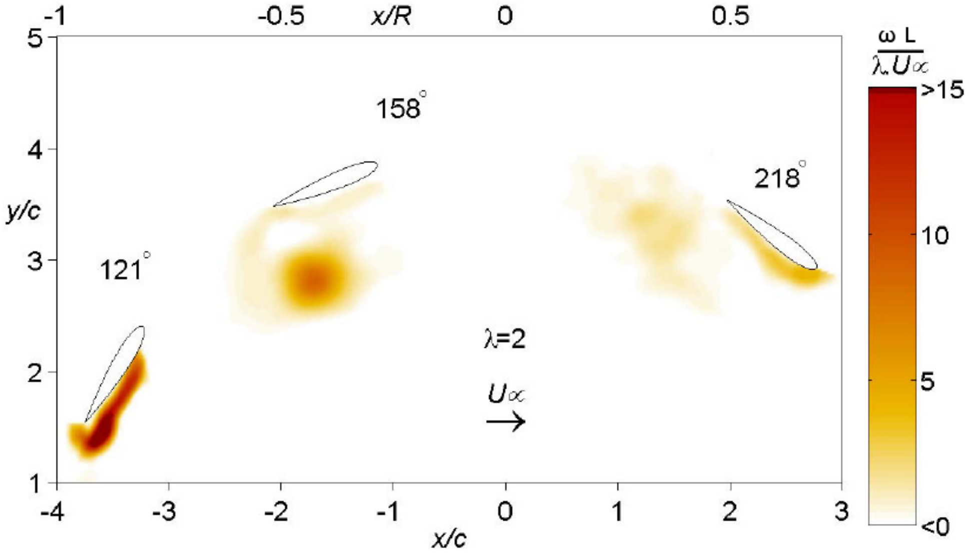

Figure 5.3: Evolution of the trailing edge vortex for $\lambda = 2$, phase locked average (PIV data from Ferreira et al. [19])

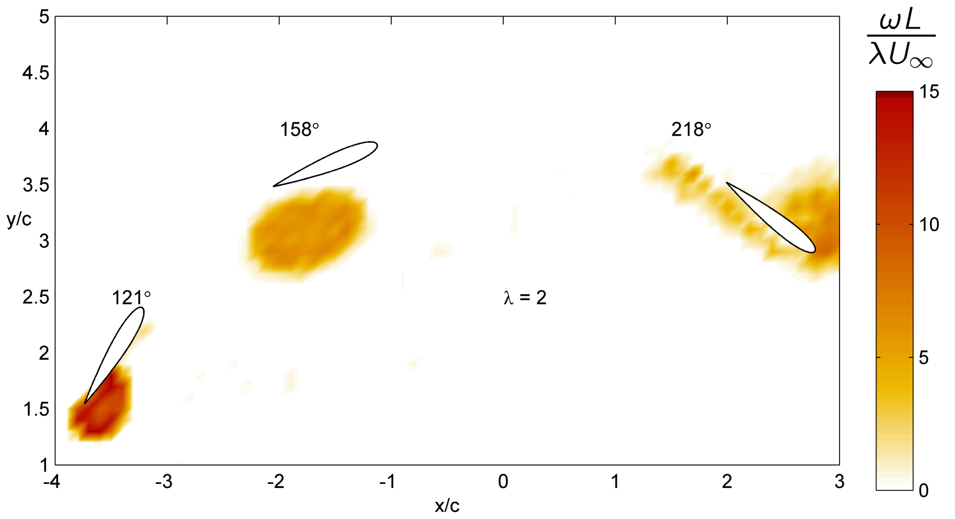

Figure 5.4: Evolution of the trailing edge vortex for $\lambda = 2$, phase locked average (vortex model, double wake)

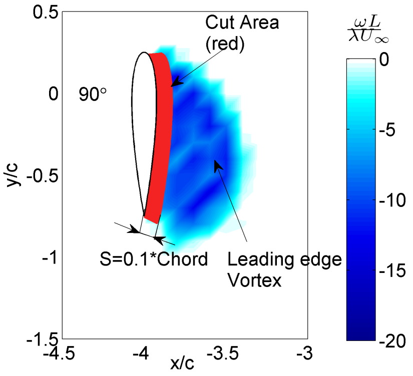

Figure 5.5: Integration contour

between the vortex model predictions (Fig. 5.2) and the PIV data (Fig. 5.1) is found for $\theta \approx 223°$, where the numerical model predicts a stronger vorticity distribution close to the aerofoil. From the comparison of Fig. 5.3 (PIV data) with Fig. 5.4 (model results) it turns out that, according to the PIV data, the trailing edge vortex starts to grow for $\theta = 121°$, whereas the model predicts this occurrence some degrees before. For $\theta = 158°$ the simulation gives a broader region of high vorticity than the PIV data and for $\theta = 218°$ its shape is slightly different. However, apart from these quantitative differences, the "double wake" model is able to reproduce the evolution of the leading edge and trailing edge vortices in good agreement with the experimental data.

The use of the vorticity to validate the numerical model is relevant only when considering both strength and distribution (see Simão Ferreira [8]). Therefore, after this "qualitative" analysis, it is necessary to focus on quantitative values such as the circulation of the leading edge vortex. The computation of the circulation from the PIV data can be affected by several sources of uncertainty. Some of them are intrinsic weaknesses of the technique, such as the measurement uncertainty and the evaluation of the flow velocity as a mean value on the interrogation window, which can reduce the accuracy in the computation of a differential operator in space as vorticity is. Furthermore, the distance of the vorticity integration contour from the blade surface cannot be taken less than two PIV interrogation windows (see Simão Ferreira [8]) and the contour extension is limited by the field of view of the PIV system. In conclusion, it is clear that there are some uncertainties in the evaluation of the results from PIV data, which heavily depend on the distance of the computation contour from the aerofoil surface. For this reason, the numerical results are plotted in Fig. 5.6 for three different values of S, which is the distance (fraction of the

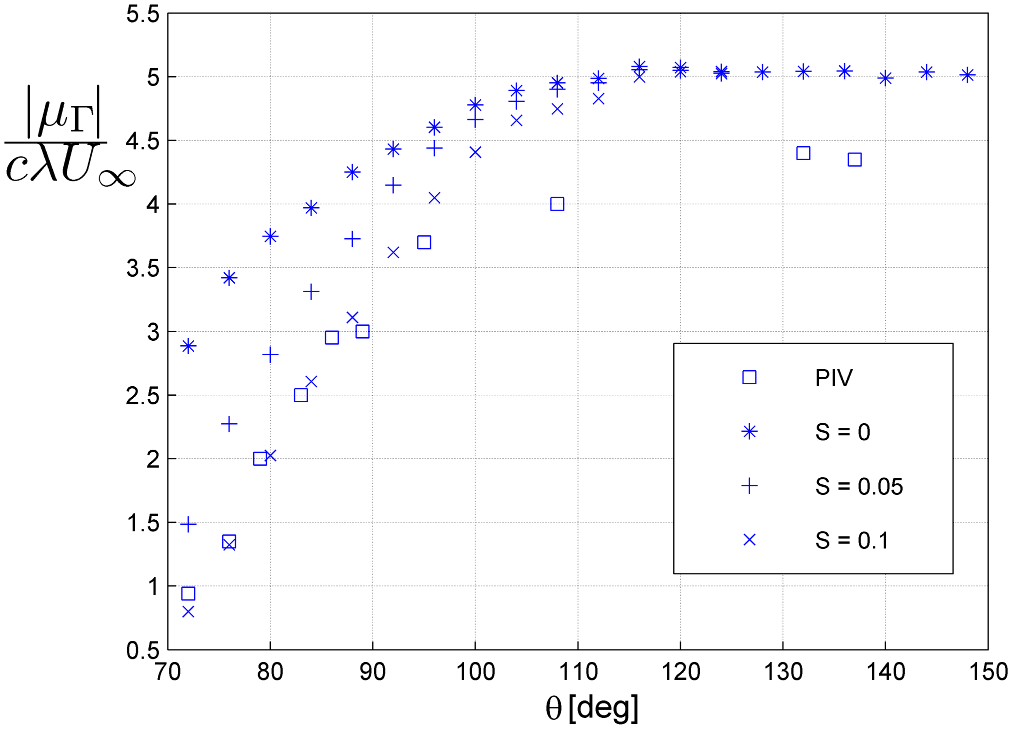

Figure 5.6: Comparison of the circulation of the simulated leading edge vortex with PIV experimental results

chord length) between the surfaces of the aerofoil and the integration contour (see Fig. 5.5). Figure 5.6 shows that the predicted circulation curve become closer and closer to the experimental one as parameter S grows. This happens especially for $70° < \theta < 95°$, when the vorticity bubble is very close to the suction side of the aerofoil and the PIV data are less reliable. In the first part of the plot the agreement can be considered as a good one because the best result is obtained for S = 0.1, which corresponds exactly to the size of two interrogation windows of the PIV system. For $\theta > 98°$ the experimental results show that the trailing edge vortex starts to roll up and the circulation of the leading edge vortex grows at a lower rate than before [8]. The numerical model predicts a smoother change in the circulation slope, which is responsible for its overestimation in the right side of the plot. However, the uncertainties in the PIV data processing require further investigations.

After the comparison with the experimental data, the forces predicted by the present model are compared with those resulting from CFD-DES simulations

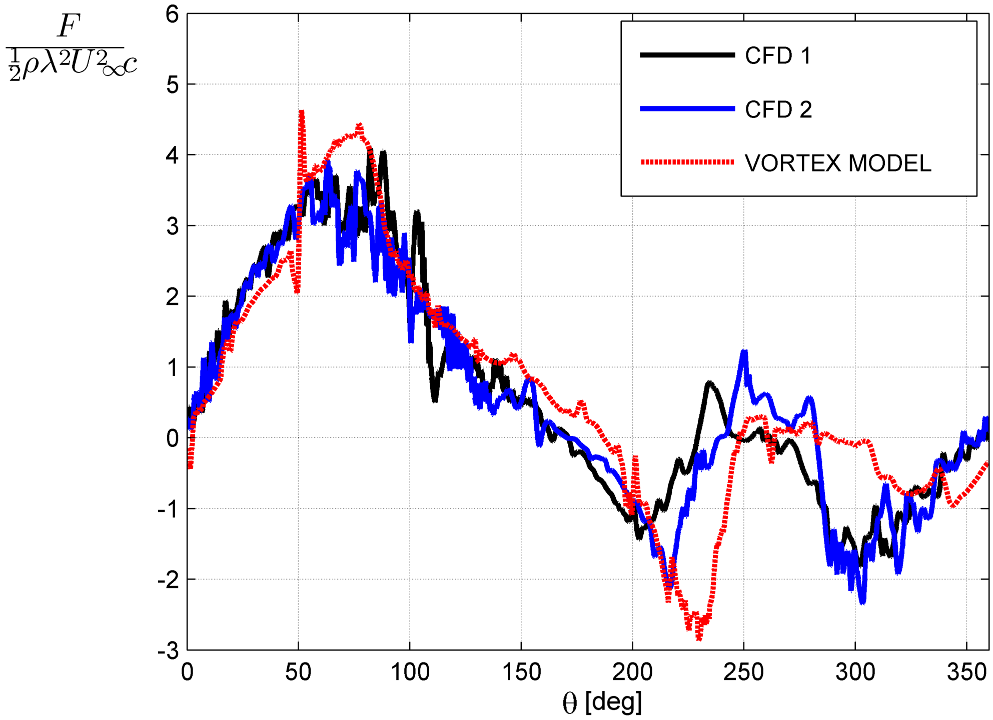

Figure 5.7: Normal forces, Vortex Model vs. CFD

(Simão Ferreira et al.[16]). Figures 5.7 and 5.8 show the normal and tangential forces predicted by the present code and by the Detached Eddy Simulation model for two different rotor revolutions (CFD 1 and CFD 2). The trend of the normal force is well captured, even though a small delay is observed when the detached leading edge vortex meets the blade ($\theta \approx 220°$). It should be stressed that almost the same difference is present between the two revolutions simulated by DES because dynamic stall and blade-vortex interaction generate a random component on loads [8]. The prediction of the tangential force agrees well, but for $\theta > 50°$ it drops too quickly. This can be due to the "jump" of the separation point to the leading edge (laminar separation). In this perspective the use of unsteady boundary layer equations could improve the accuracy of the present model predictions. However, the code captures quite well the trends of both the normal and tangential forces, so being able to simulate properly the generation, growth and release of the leading and trailing edge vortices and to reproduce their influence in the downwind part of the blade rotation.

In conclusion, the ability of the code to simulate the flow field induced by

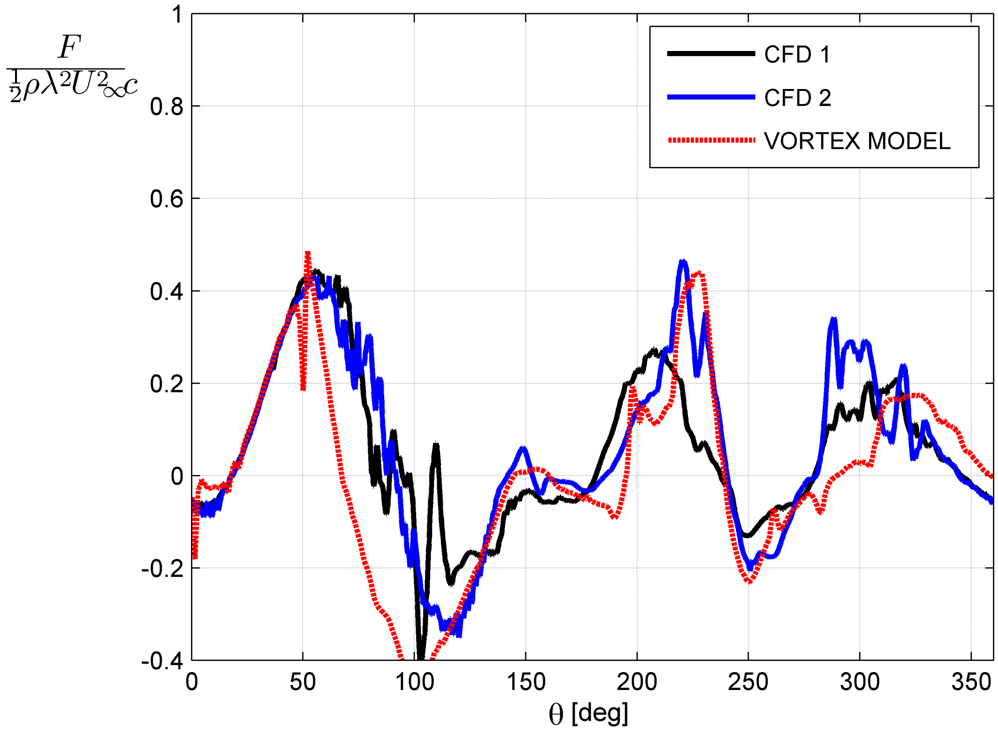

Figure 5.8: Tangential forces, Vortex Model vs. CFD

the VAWT was proved from both qualitative and quantitative standpoints. In the next section, the present code will be used to analyse the influence of the unsteadiness on the VAWT performance.

5.2 Influence of the dynamic stall on the vorticity field

To clarify the influence of the dynamic stall on the vorticity distribution, the solution of the potential flow in attached conditions (single wake model) is presented at first in Fig. 5.9. The working condition is the same as in Fig. 5.10 i.e., one blade, $\lambda = 2$, $\kappa = 0.125$ and $Re = 5 \times 10^4$. In this configuration the vorticity shed from the trailing edge depends only on the variation of the aerofoil circulation that, in a potential flow, is directly related to the angle of attack. For this reason, for $-90^\circ < \theta < 90^\circ$ the vorticity is always positive while for $90^\circ < \theta < 270^\circ$ it is always negative (clockwise). A solution such that

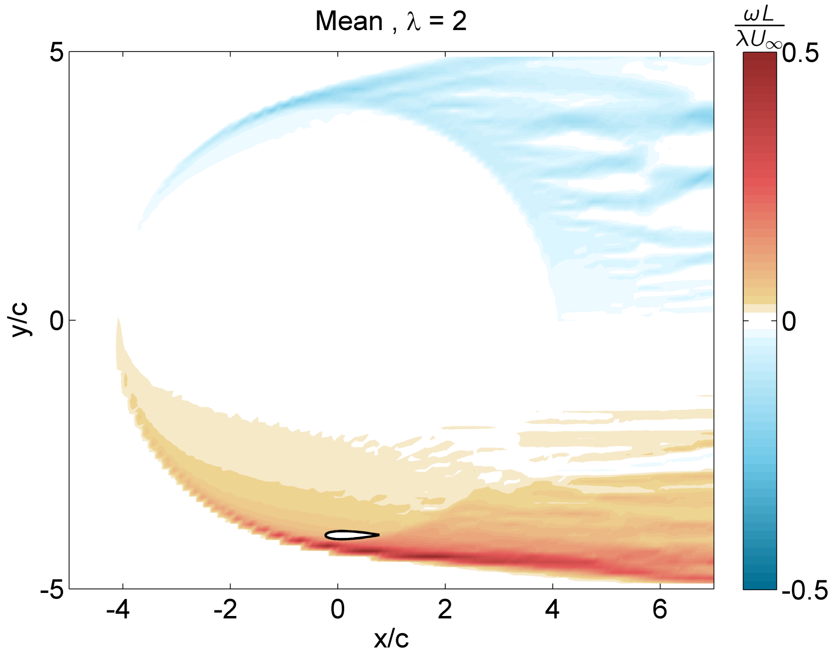

Figure 5.9: Results of the single wake panel model (without stall): time-averaged vorticity distribution

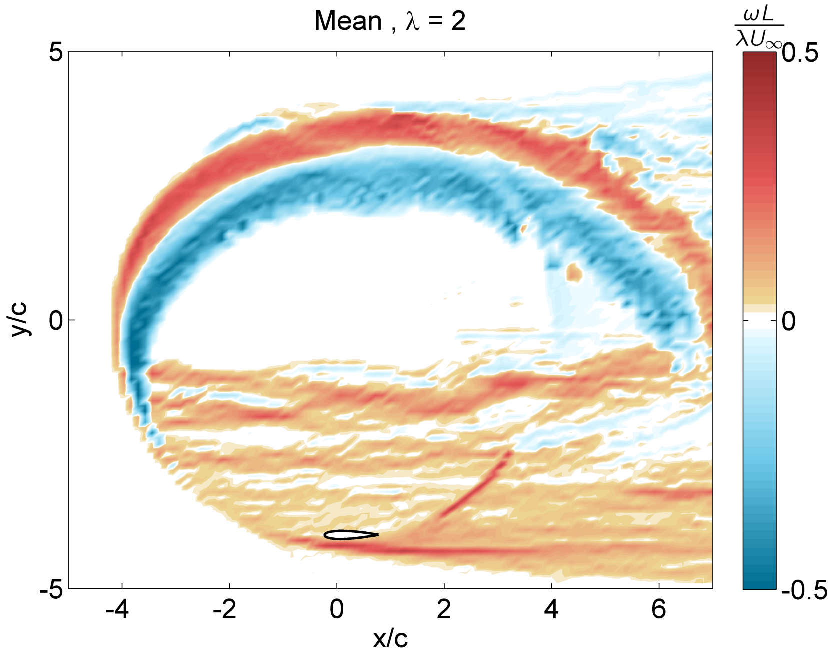

Figure 5.10: Results of the double wake panel model (with stall modelling): time-averaged vorticity distribution

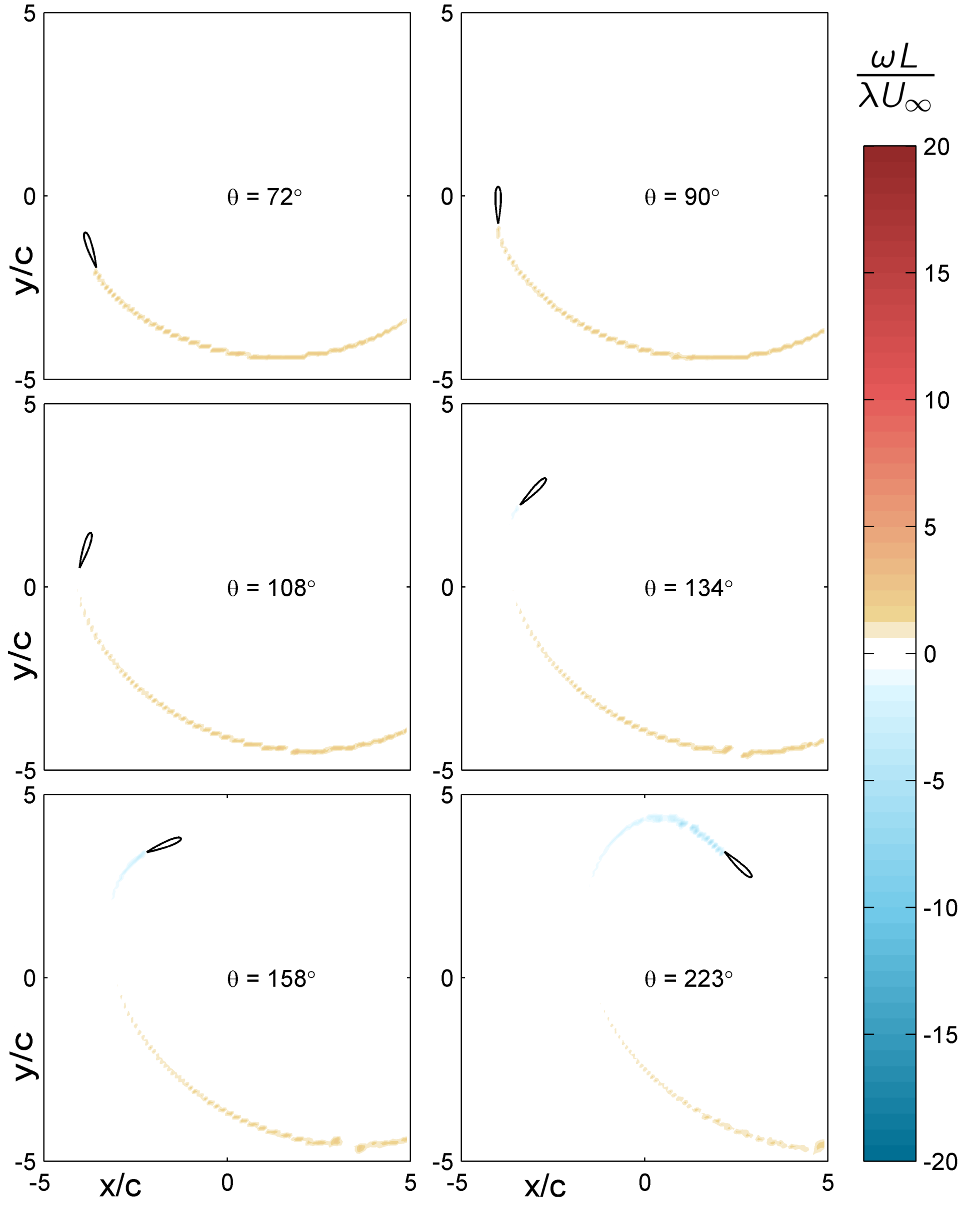

Figure 5.11: Results of the single wake panel model: vorticity distribution, phase locked average

in Fig. 5.9 can be considered as a good approximation of the real flow as long as the tip speed ratio is larger than 4, but for lower values of λ (when the stall occurs) it becomes unacceptable. This is clearly evidenced in the phase locked averaged solutions of Fig. 5.11 that, when compared to the solution of the double wake model (Fig. 5.12), shows no roll up of the trailing edge vortex.

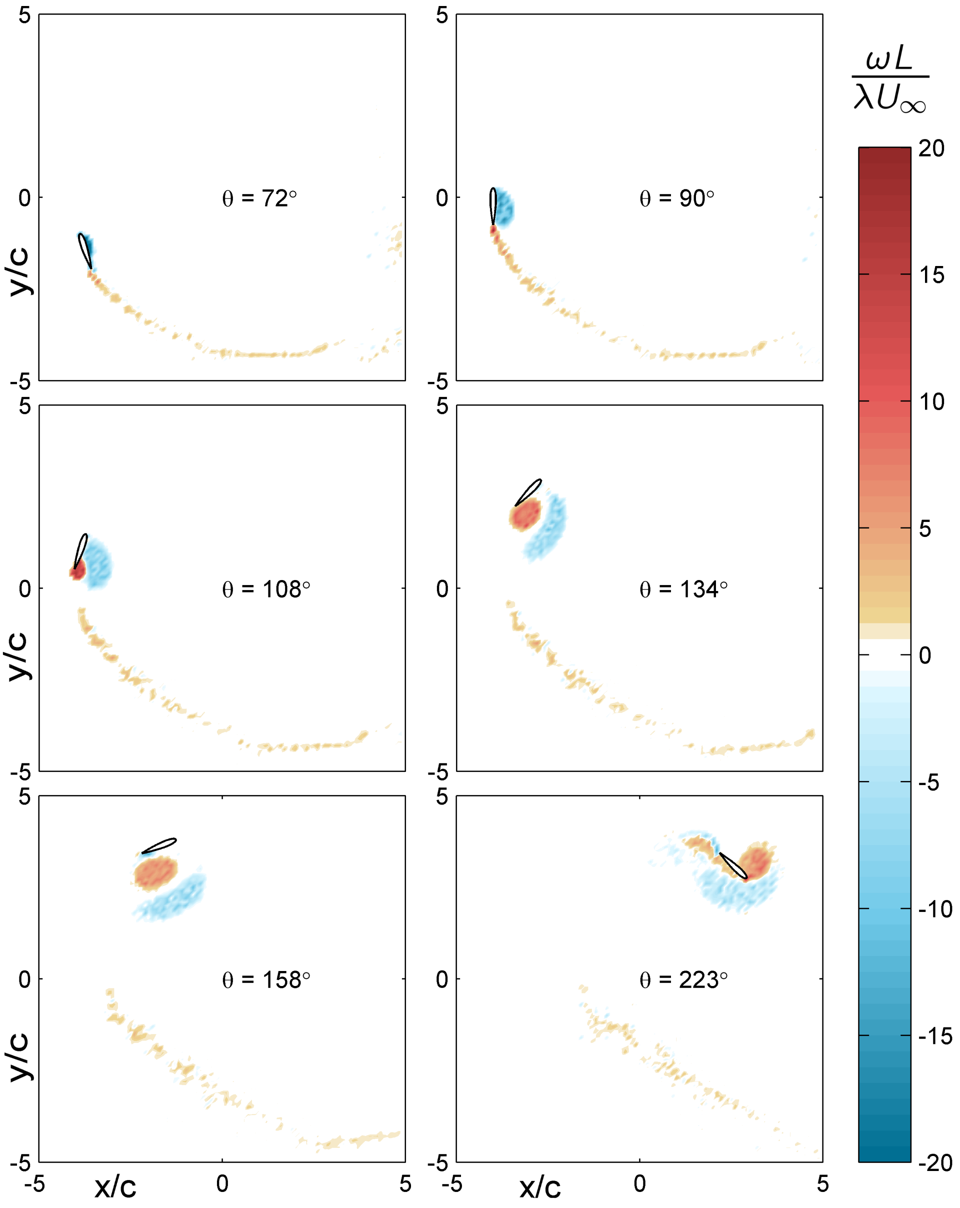

Figure 5.12: Results of the double wake panel model: vorticity distribution, phase locked average

This leads to a strongly inaccurate prediction of the VAWT performance. The first reason is the overestimation of the lift and the second one is the absence of the trailing and leading edge vortices that, especially for $150° < \theta < 270°$, strongly influence the induced velocity field. Therefore, the use of the single wake model for $\lambda < 4$ causes an important part of the wake-blade interaction

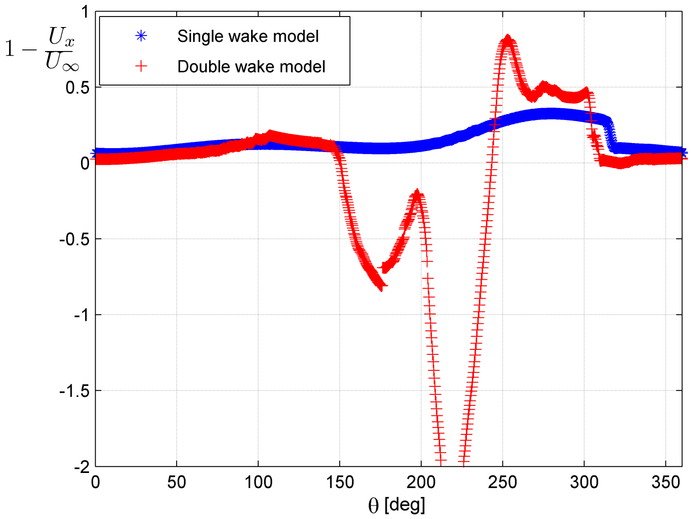

Figure 5.13: Induction factor for the single and double wake models

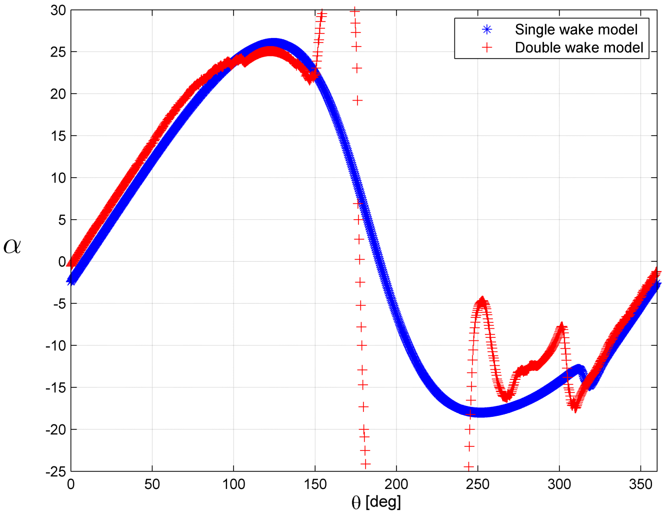

Figure 5.14: Angle of attack for the single and double wake models

to be neglected.

To quantify the influence of the dynamic stall it is interesting to compute the induction factor a ($a = 1 - (u_x/u_\infty)$ where u_x is the flow velocity in x-direction at a quarter of the blade chord) from the solutions of the single and double wake models. The induction factor (the same used in the momentum models) quantifies the local change of the freestream velocity due to the wake, and permits to compute the angle of attack perceived by the aerofoil. This parameter is very useful in the momentum models, where the knowledge of the perceived angle of attack allows the use of experimental databases of lift and drag.

Figure 5.13 shows a comparison between the single and the double wake models in terms of induction factor. Parameter a is computed excluding all vortices that are, contemporaneously, closer than two chords to the chord midpoint of the aerofoil and released in the last quarter of rotation. This is necessary especially for the double wake model where all these vortices are used to model the separation wake, but they are not yet part of the wake.

The initial trends of the two curves in Fig. 5.13 are comparable until the stall occurs ($\theta \approx 50°$). Due to the lower induction in the double wake solution, the perceived angle of attack is larger (see Fig. 5.14). In the second half of the upwind part, in the attached flow condition, the bound circulation and hence the induction start to decrease. What happens in the dual wakes model solution is more interesting. The leading edge vortex is released from the aerofoil ($\theta \approx 138°$) and since it is transported downstream by the flow while remaining close to the blade, it starts to strongly influence the velocity field surrounding the aerofoil. For this reason the induction exhibits a first negative peak (a corresponding positive peak is observed for the perceived angle of attack) that should be considered as an indication of a strong wake-blade interaction, which in turn makes the use of the induction factor unfounded. This can be a serious problem for the models based on the momentum theory, where the induction is obtained from a local momentum balance, that are not able to capture the wake-blade interaction. A second negative peak is observed in the first half of the downwind part, when the leading and trailing edge vortices, transported downstream by the flow, meet the aerofoil. At the start of the second half of the downwind part ($\theta \approx 270°$) the double wake model predicts a higher induction and, as a consequence, a smaller absolute value of the perceived angle of attack. Close to the end of the revolution a third wake-blade interaction occurs and the induction predicted by the separation model becomes lower than the one of the fully inviscid solution.

In conclusion, the dynamic stall of a VAWT has been shown to strongly

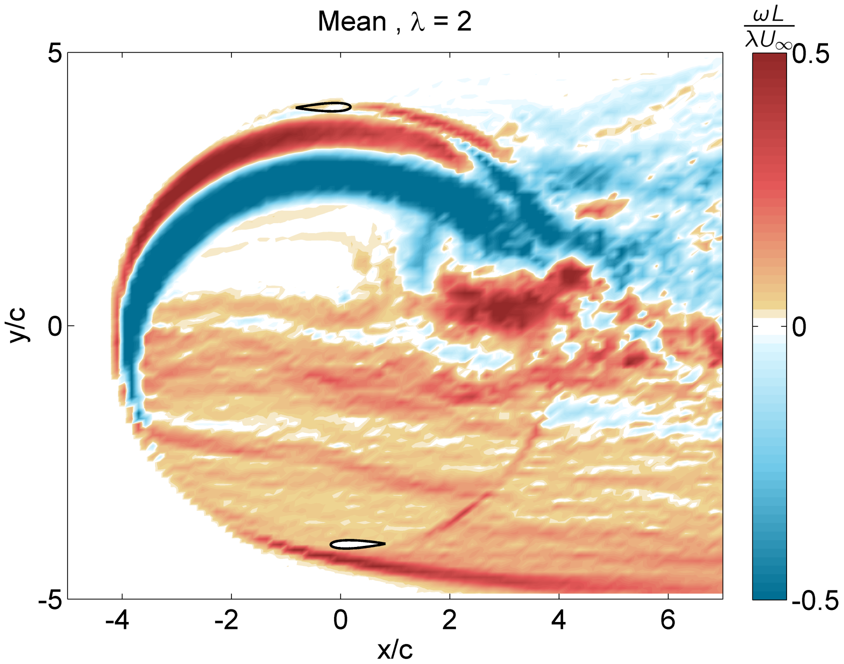

Figure 5.15: Two-blades VAWT, time-averaged vorticity distribution over 8 rotations, $\lambda = 2$, $k = 0.125$ and $Re = 50000$

affect the wind turbine performance also due to the interaction of the blade with the leading and trailing edge vortices transported downstream by the flow. This effect is not captured by the momentum based approaches, but it is properly taken into account by the present double wake model.

5.3 Influence of the number of blades

In section 5.2 the wake-blade interaction due to the dynamic stall was discussed for a single blade VAWT. Figure 5.15 shows the time-averaged vorticity field over eight rotations for a two-blade rotor ($\lambda = 2$, $\kappa = 0.125$ and $Re = 5 \times 10^4$).

It is noticed that the vorticity field preserves the same distribution as in the one-blade configuration (Fig. 5.10). This is confirmed by the phase locked average, where the formation and growth of the leading edge vortex follows the same process (Fig. 5.16).

The only significant difference is in the downwind part of the rotation, where the leading and trailing edge vortices, released from the previous aerofoil slow down the downstream motion of the new vortices. Therefore, this continu-

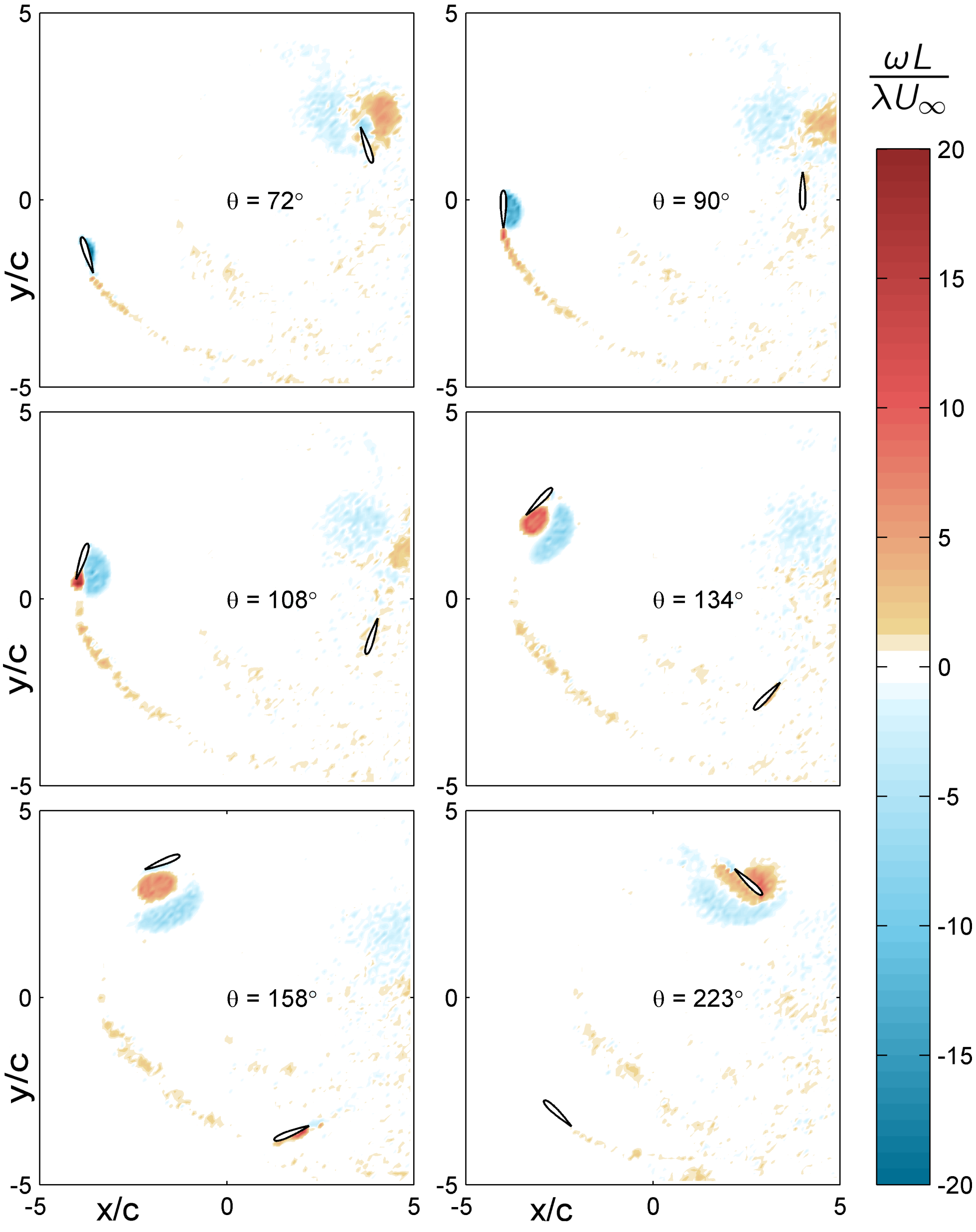

Figure 5.16: Two-blades VAWT, vorticity distribution for $\lambda = 2$, $k = 0.125$ and $Re = 50000$. Phase locked average

ous vortex shedding creates a region of low velocity ($\theta \approx 270°$) that makes the induction field quite different from the one produced by the single blade configuration (Fig. 5.19).

The trends of the tangential and normal forces (Figs. 5.17 and 5.18) in the

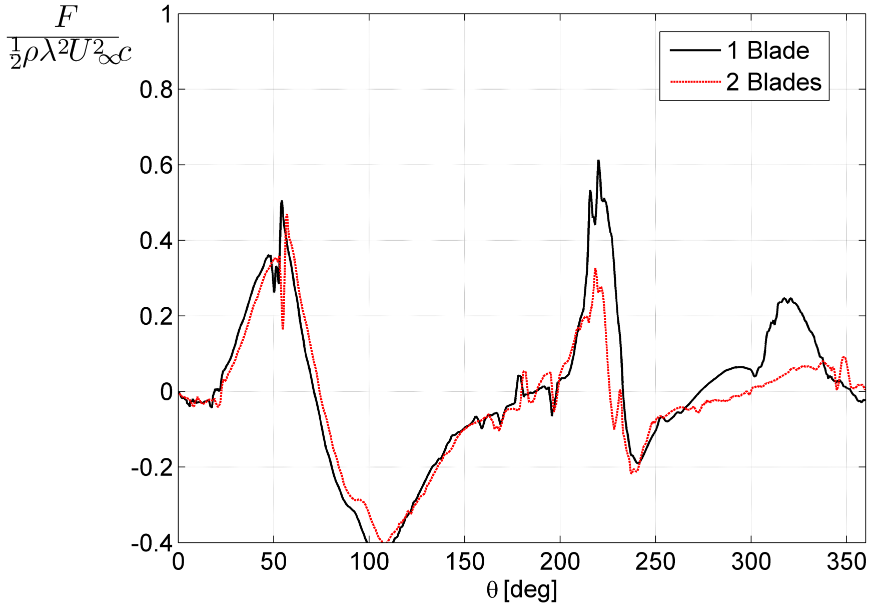

Figure 5.17: Tangential forces over one rotation, one- and two-blades VAWT

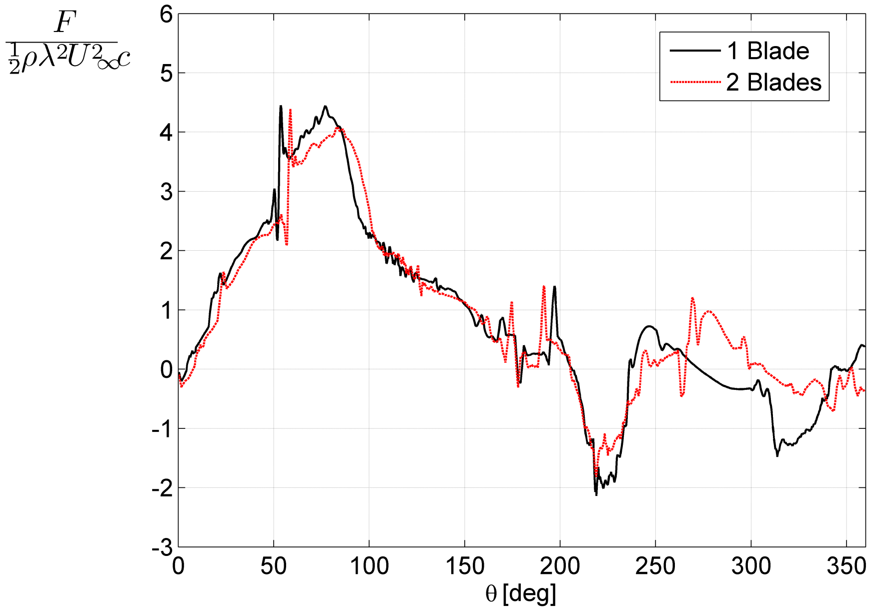

Figure 5.18: Normal forces over one rotation, one- and two-blades VAWT

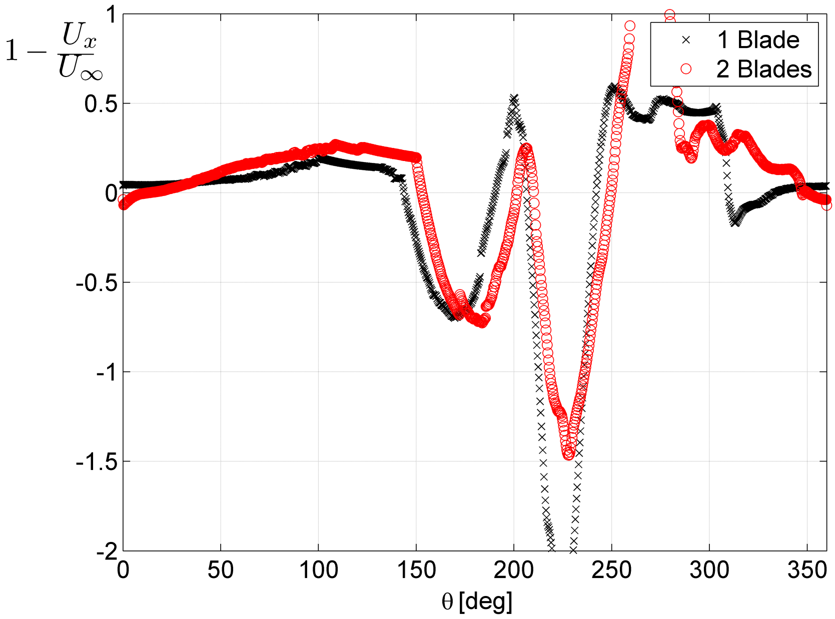

Figure 5.19: Induction factor over one rotation, one- and two-blades VAWT

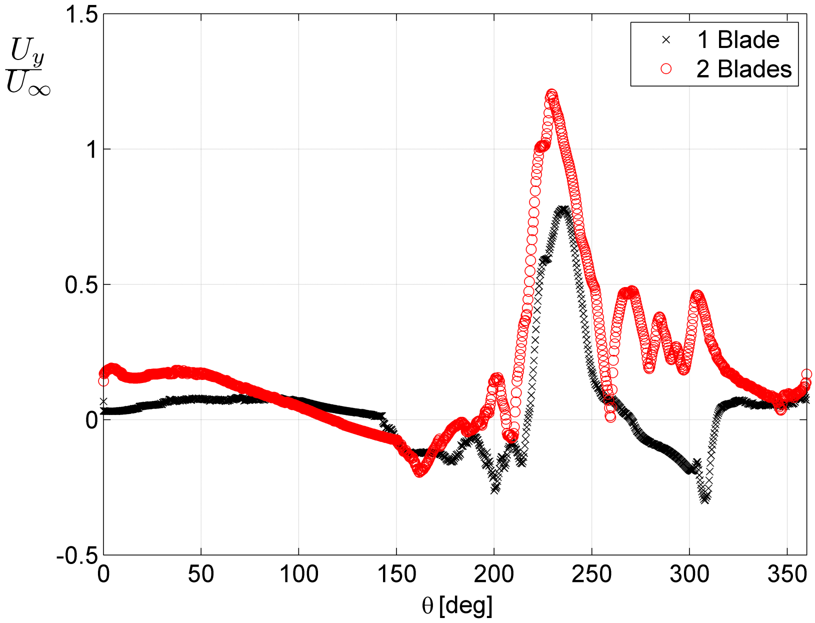

Figure 5.20: Induction factor normal to the freestream velocity over one rotation, one- and two-blades VAWT

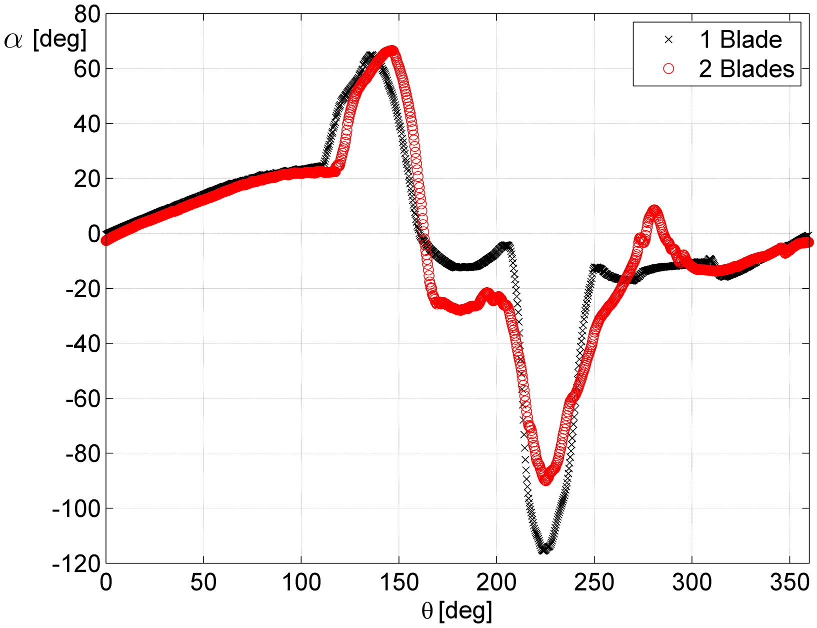

Figure 5.21: Angles of attack over one rotation, one- and two-blades VAWT

cases of one-blade and two-blades VAWT are similar, with some differences in the downwind part of the rotation. As expected, in the first part of the rotation ($0° < \theta < 60°$) the forces are lower in the two-blades configuration, but this is not caused by the increase in the induction factor due to the greater power exchange, as should be predicted by the momentum models. In fact, the induction in x direction for the two-blades VAWT is lower than in the single blade configuration (it is even negative for $\theta < 20°$, Fig. 5.19), but a stronger induction appears in the y direction (Fig. 5.20) that reduces the forces on the blade by decreasing the angle of attack (Fig.5.21). This behaviour is caused by the low convection velocity of the leading and trailing edge vortices, which are almost at a stop in the downwind part of the rotor, so producing a deviation of the flow towards the leeward and windward parts of the rotor (Fig. 5.22). Therefore the increase in the flow expansion in the two-blades configuration (compare Figs. 5.23 and 5.22) is not only due to the greater power extraction in the first upwind part of the rotation, but it is also due to the presence of the leading and trailing edge vortices in the downwind part of the rotor.

Since the most common tool used for the simulation of the VAWT is the momentum model (sec. 1.3.1), it seems necessary to remind the reader that the actuator disk concept (also in the most advanced version, i.e. the double

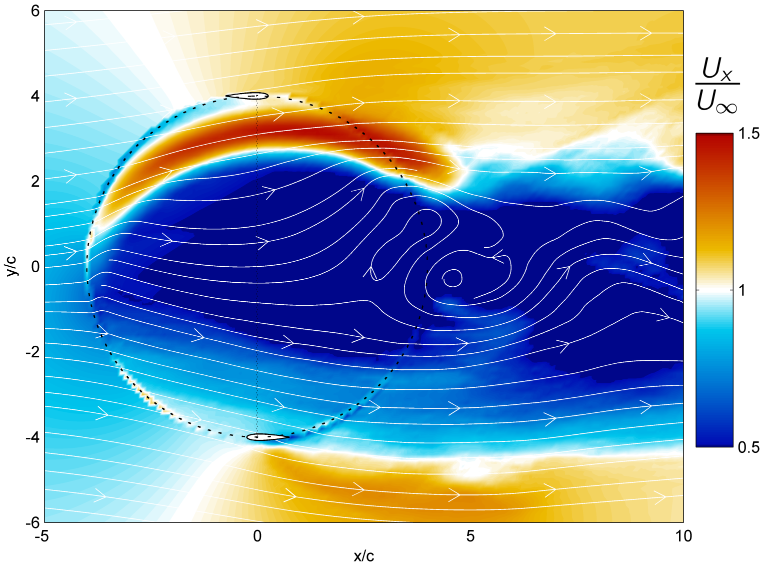

Figure 5.22: Streamlines and contour plot of the mean velocity (over one rotation) in the streamwise direction. Two-blades VAWT

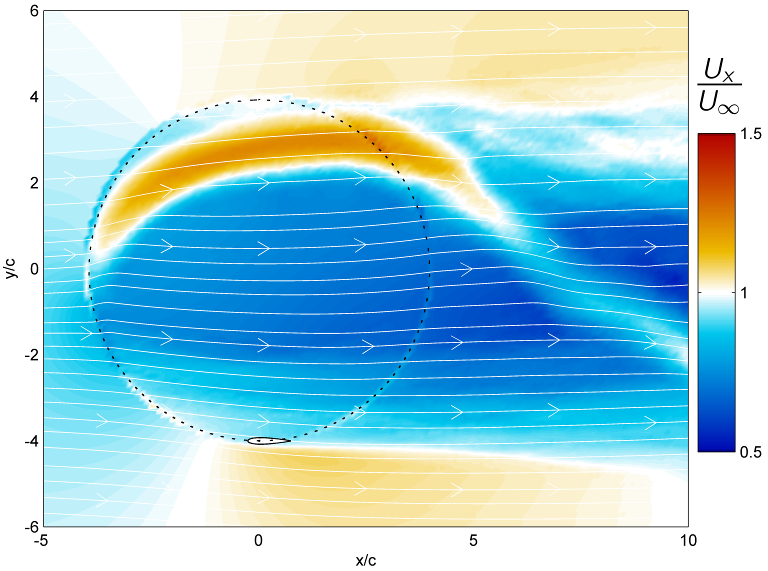

Figure 5.23: Streamlines and contour plot of the mean velocity (over one rotation) in the streamwise direction. One-blade VAWT

multiple streamtube model) is not capable of reproducing these complex flow conditions. It could be argued that a correction for the streamline expansion can be included in the momentum models (see, e.g., Simão Ferreira [8]), but this would still neglect the influence of the strong leading and trailing edge vortices and hence the physics of the energy conversion process.

For $130° < \theta < 260°$ the flow that surrounds the aerofoil is highly disturbed by the wake and a large variation of the perceived angle of attack (Fig. 5.21) occurs due to the strong leading and trailing edge vortices. As said in sec. 5.2, the unreasonable values of the induction factor and the perceived angle of attack are due to the strong blade-wake interaction, which in turn makes their use unfounded. In the two-blades configuration the wake-blade interaction region is larger (till $\theta = 310°$), so that in about all the downwind part of the rotation the flow is highly bended by the vortices. That makes unreasonable the use of aerofoil section data for the evaluation of the lift as done in the momentum models or in the free vortex wake method (secs. 1.3.1 and 1.3.2).

5.4 Comparison between dynamic and quasi-steady stall

For low values of κ a significant change in the separation and shedding phenomenology occurs. Therefore, below $\kappa = 0.05$ the stall condition will be defined as “quasi-steady stall” to distinguish it from the “dynamic stall”.

To deepen the knowledge of the influence of the unsteadiness, the previous results will be compared with the quasi-steady stall condition. It should be mentioned that the reduction in the reduced frequency implies a change in the chord-to-radius ratio. In order to keep constant the rotor solidity, the one-blade VAWT, $\lambda = 2$, $\kappa = 0.125$, $Re = 5 \times 10^4$, will be compared with a three blades turbine, $\lambda = 2$, $\kappa = 0.0416$ and $Re = 5 \times 10^4$.

Figure 5.24 shows the mean vorticity field over eight rotations for the three blades VAWT. It provides a clear picture of the path of the leading and trailing edge vortices released from the aerofoil and transported downstream by the flow. The vorticity distribution and hence the induction field turn out to be very different compared to the ones produced by the dynamic stall. The leading and trailing edge vortices do not grow anymore following the suction side of the aerofoil, but they are released and transported with a shedding frequency that is much higher than the one of the blade rotation (Fig. 5.25). This radically changes the distribution of the vorticity in the wake, which produces important changes in the wake-blade interaction. Figures 5.26 and 5.27 show the normal

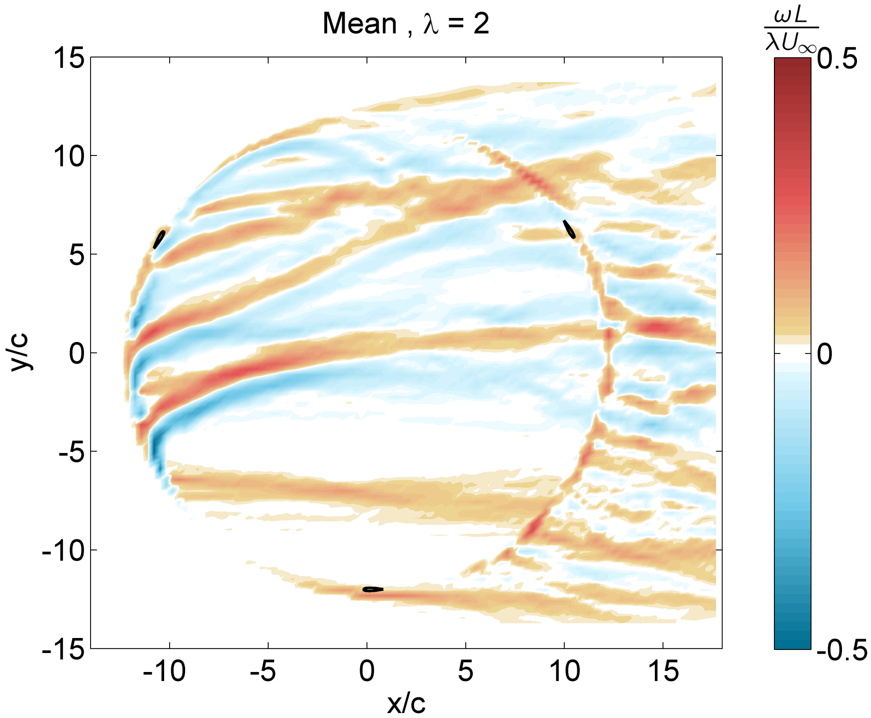

Figure 5.24: Three blades VAWT, time-average vorticity distribution over 4 rotations, $\lambda = 2$, $k = 0.0416$ and $Re = 5 \times 10^4$

and tangential forces for the two configurations. The influence of the dynamic stall is evident in the upwind region, where it introduces a stall that causes the force drop to be deferred. When the separation occurs, in the quasi-steady stall condition both the normal and the tangential forces exhibit oscillations, due to the shedding of the leading and trailing edge vortices, the frequency of which is much higher than the blade rotation frequency.

In the downwind region, for $\kappa = 0.0416$, the absence of a strong leading edge vortex in phase with the blade rotation has two main consequences on the tangential force. The peak at $\theta = 220°$, due to the leading edge vortex that hits the aerofoil, disappears. Furthermore, no flow reattachment is observed for $\kappa = 0.0416$. On the contrary, the reattachment occurs at $\theta \approx 250°$ in the case $\kappa = 0.125$, due to the high velocity induced by the strong leading edge vortex that reduces the absolute value of the perceived angle of attack (see, Fig. 5.28). For $240° < \theta < 300°$ the separation occurs in the quasi-steady stall condition and, as in the upwind part, force oscillations are induced by the vortex shedding at a frequency higher than the blade rotation frequency.

The same periodic behaviour is observed in the induction factors (Figs. 5.29

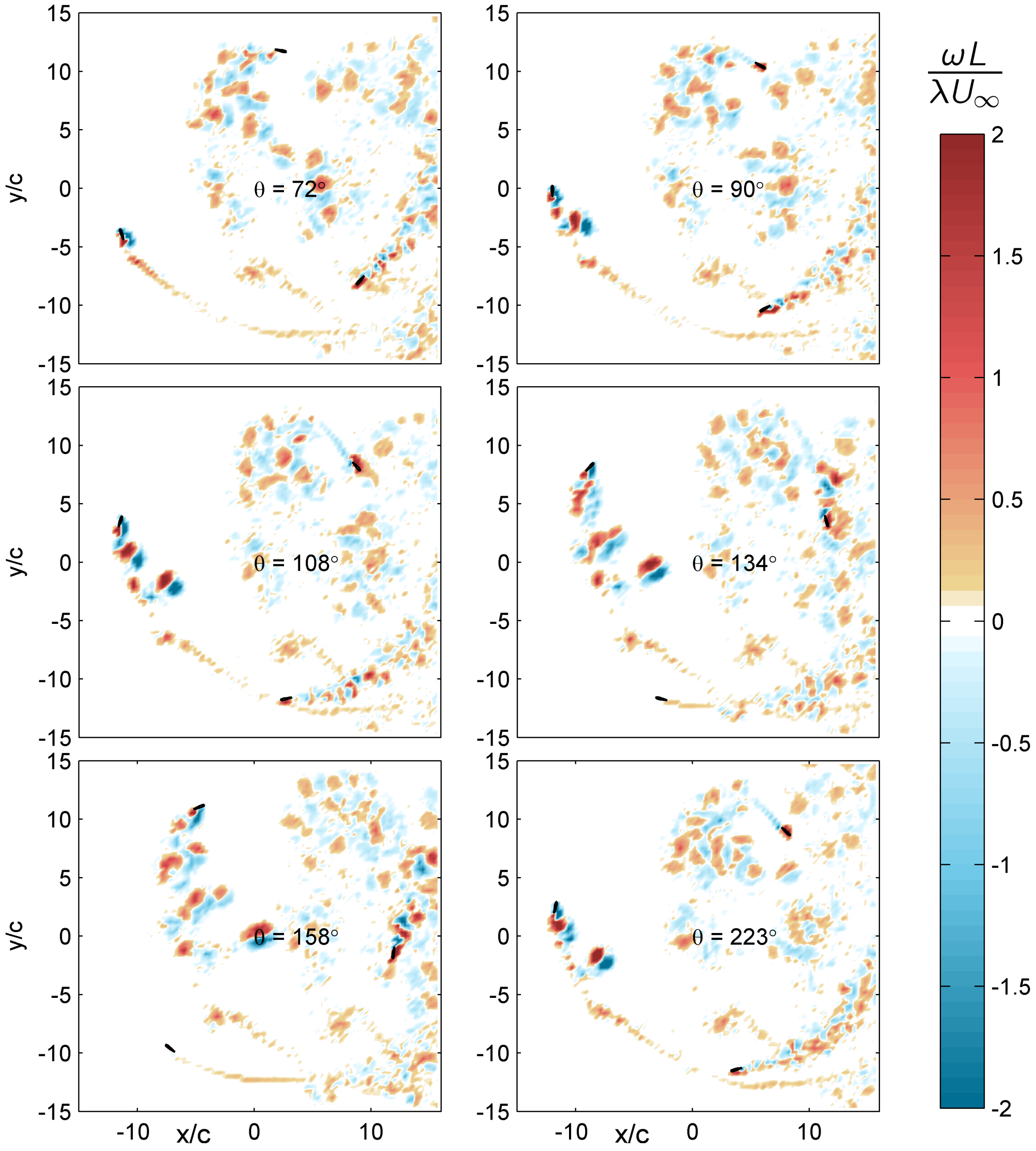

Figure 5.25: Three blades VAWT, phase locked averaged vorticity, $\lambda = 2$, $k = 0.0416$ and $Re = 5 \times 10^4$

and 5.30) where the peaks due to the wake-blade interaction are lower than in the dynamic stall condition.

In summary, the dynamic stall, when compared with the quasi-steady stall, causes a delay in the aerofoil stall and produces a strong leading edge vortex that interacts with the blade and influences the flow field (and forces) in the downwind passage.

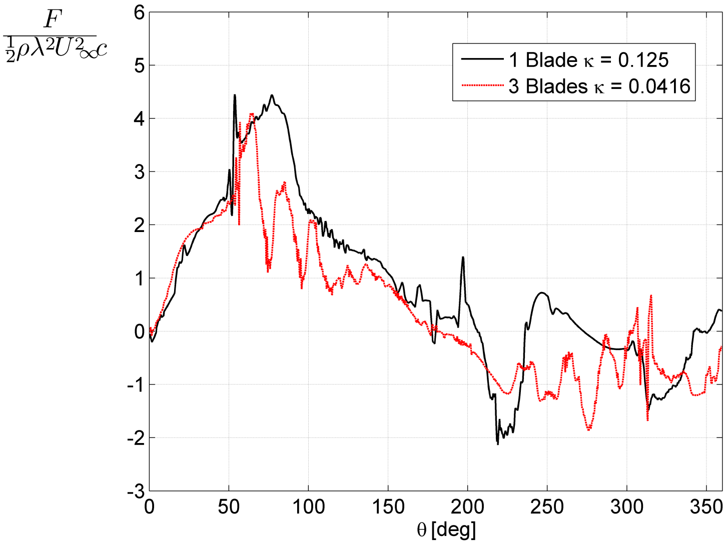

Figure 5.26: Normal forces over one rotation, dynamic stall ($\kappa = 0.125$), quasi-steady stall ($\kappa = 0.0416$) and $Re = 5 \times 10^4$

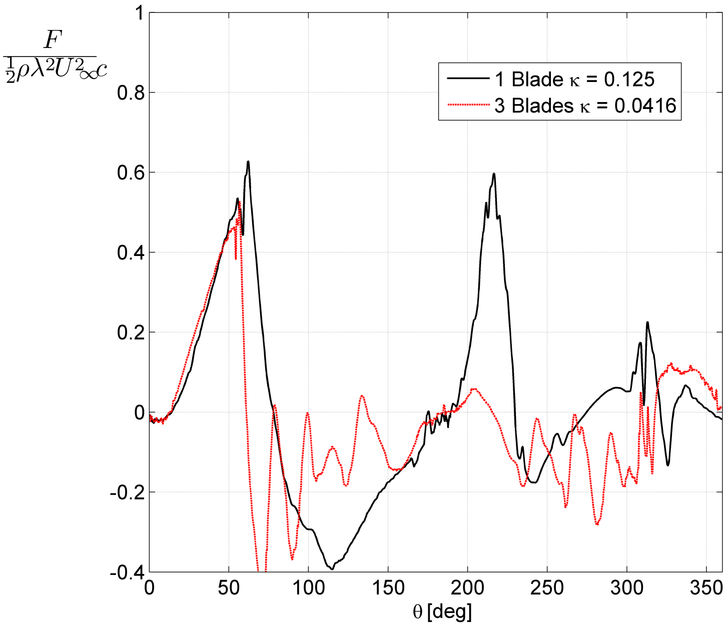

Figure 5.27: Tangential forces over one rotation, dynamic stall ($\kappa = 0.125$), quasi-steady stall ($\kappa = 0.0416$) and $Re = 5 \times 10^4$

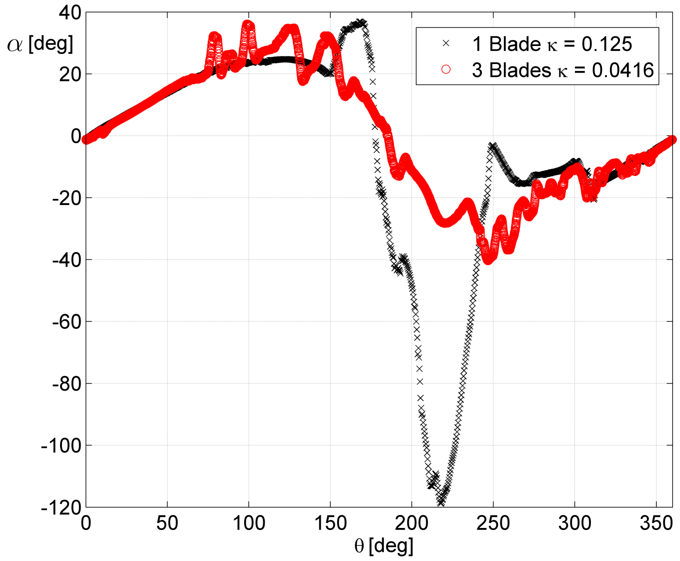

Figure 5.28: Perceived angle of attack over one rotation, dynamic stall ($\kappa = 0.125$), quasi-steady stall ($\kappa = 0.0416$) and $Re = 5 \times 10^4$

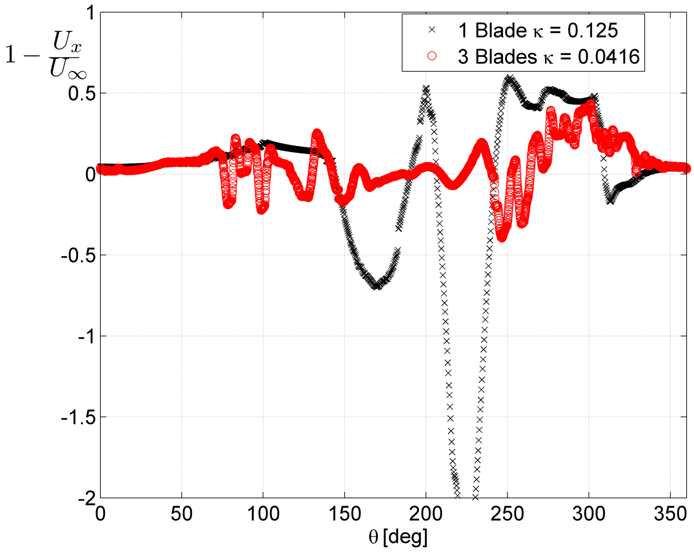

Figure 5.29: Induction factor over one rotation, dynamic stall ($\kappa = 0.125$), quasi-steady stall ($\kappa = 0.0416$) and $Re = 5 \times 10^4$

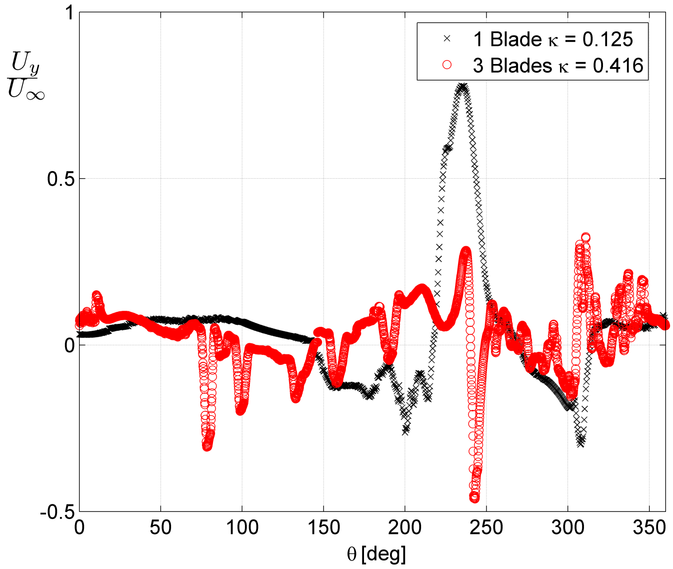

Figure 5.30: Induction factor normal to the freestream velocity over one rotation,dynamic stall ($\kappa = 0.125$), quasi-steady stall ($\kappa = 0.0416$) and $Re = 5 \times 10^4$

5.5 VAWT performance

In this section, the 2D VAWT rotor performance in terms of power coefficient C_p, at different tip speed ratios λ, is presented. The simulation results for a single blade VAWT are plotted in Fig. 5.31 by comparing the solutions at $Re_{rotor} = 2 \times 10^5$ ($Re = 5 \times 10^4$ for $\lambda = 2$) $Re_{rotor} = 4 \times 10^5$.

For $2 < \lambda < 3$ and $Re_{rotor} = 2 \times 10^5$ C_p is negative, due to the deep stall in the upwind region. The machine starts to extract energy from the flow when $\lambda = 3.5$, although the dynamic stall still occurs. Increasing the rotor *Reynolds* number ($Re_{rotor} = 4 \times 10^5$), C_p becomes positive for $\lambda = 3$, earlier than before, because the increase in the blade *Reynolds* number delays the separation, which allows a higher energy exchange in the upwind part of the rotation.

For $\lambda > 4$, the higher blade *Reynolds* number and the lower perceived angle of attack allow, in both simulations, to avoid the separation from the leading edge. Therefore, the power coefficient rises and only a weak separation occurs close to the trailing edge. For both $Re_{rotor} = 2 \times 10^5$ and $Re_{rotor} = 4 \times 10^5$ the maximum value of C_p is obtained for $\lambda = 5$, over which the power coefficient starts to decrease due to the rapid increase in the viscous forces. These forces are also responsible for the gap between the two curves ($4 < \lambda < 6$), since

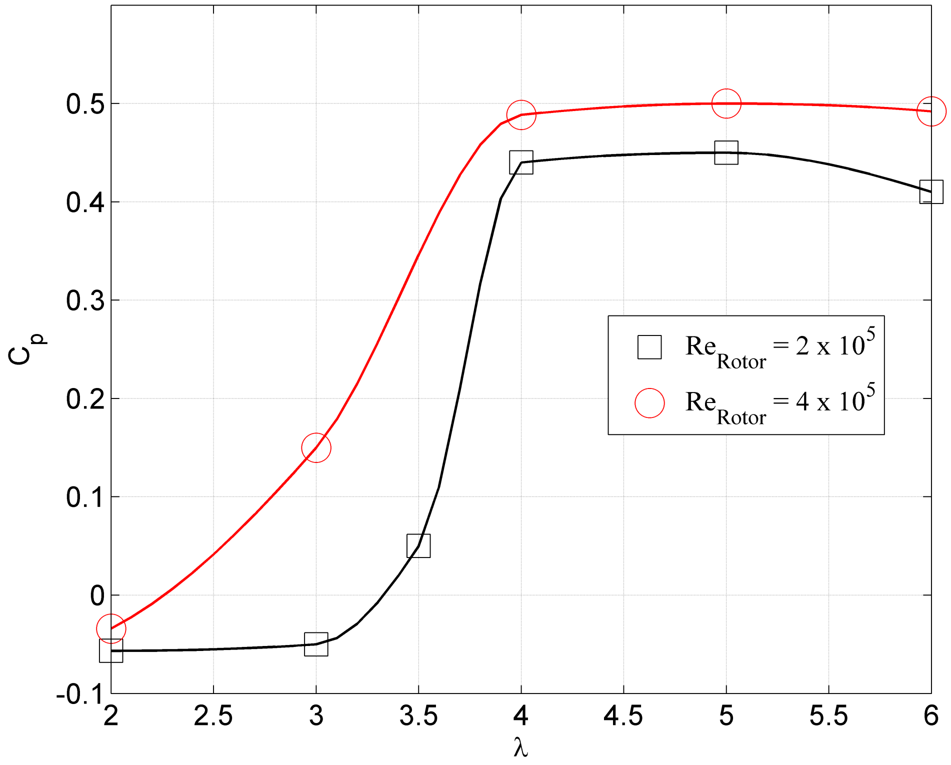

Figure 5.31: Power coefficient vs. tip speed ration λ

the viscous contribution, in proportion, decreases at increasing the *Reynolds* number.

In the present thesis no attempt is made to compare the predicted power curve (C_p vs. λ) with that of a real three dimensional VAWT. In fact, as previously discussed in sec. 1.5, the influence of the tip vortices on the turbine global performance is too strong to be neglected.

In the 2D momentum models some empirical formulations are used (see [20],[12]) in order to apply tip-effect corrections to the loading. Of course some kind of corrections could be applied also to the present model, but it was not done because the purpose of the present work is to increase the knowledge of the physics of the energy conversion process under the 2D flow assumption and a complex three dimensional feature as the tip vortex cannot be reproduced by a 2D model. The prediction of the power curve and the physics of the energy conversion process of a real VAWT is an interesting challenge, but it must be carried out with the appropriate tool, namely, a 3D model.

6

Conclusions

A double wake panel vortex method coupled with the boundary layer equations has been developed for simulating the 2D flow past a VAWT. This model is able to face rotating multi-aerofoils problems in separated flow conditions. It is one of the very few double wake vortex models available for VAWTs.

A preliminary model validation has been performed by comparing the results obtained for a steady and a pitching aerofoil in dynamic stall at high *Reynolds* number ($Re = 1.5 \times 10^6$) with experimental load data available in the literature. An excellent agreement was observed in both attached and separated flow conditions. In particular, satisfactory predictions of the aerodynamic loads and flow separation and reattachment were obtained for the steady aerofoil as well as for the pitching aerofoil in dynamic stall.

Subsequently, the model has been tried out in a more critical flow condition ($Re = 5 \times 10^4$) by comparing the numerical results with time-resolved PIV data, collected by the author, concerning a steady aerofoil and two oscillation frequencies of a pitching aerofoil in dynamic stall. The PIV data were properly processed in order to obtain the vorticity fields and blade loads to be compared with the model predictions. For the steady aerofoil, the predicted and experimental loads agree well in both attached and separated flow conditions, as well as the position and shape of the separated shear layer do. At both pitching frequencies the load hysteresis loops are well predicted and the dynamics of the leading edge vortex, which characterises the dynamic stall, is well captured. In particular, the comparison with the PIV vorticity fields shows that all the processes of vortex formation, growth and shedding are correctly reproduced. Also the flow reattachment in dynamic stall is properly simulated thanks to the special strategy devised to move the separation panel along the aerofoil surface. At the higher pitching frequency the phenomenology of the dynamic stall includes the shedding of two strong vortical structures from the leading edge. This is correctly reproduced by the numerical results, which proves the good sensitivity of the model to the variation rate of the angle of attack.

The model has been used to compute the wake flow past a VAWT in dynamic stall and the numerical results have been compared with phase-locked PIV data and CFD-DES simulations available in the literature. The complex vorticity distribution due to the energy conversion process is well reproduced, showing the ability of the present model to cope with separated flows and strong wake-blade interactions. The predicted values of the forces turn out to be comparable with the ones provided by the much more expensive CFD approaches.

The capabilities of the present model have been explored further on by performing an analysis of the influence of dynamic stall, number of blades and reduced frequency on the VAWT vorticity field and forces. When compared with a single wake model, which cannot allow for the dynamic stall, the present model predicts much more complex vorticity and induction fields characterised by the release of vorticity of opposite signs from the separation point and the trailing edge, which strongly alters the dynamics of the blade-wake interaction. When considering a two blades VAWT instead of a single blade one, vorticity is observed to accumulate in the downwind region, which causes a strong expansion of the main flow crossing the rotor. A low reduced frequency, corresponding to the "quasi-steady stall" condition, gives rise to the release of vortical structures at a frequency much higher than the rotation frequency, which introduces high frequency oscillations in the aerodynamic forces and reduces the power extraction in the downwind part of the blade rotation.

More generally, the model allows the influence of the dynamic stall to be characterised in both the aerofoil scale and the rotor/wake scale. The former is very important in the upwind part of the rotor motion, where the stall mainly affects the pressure distribution on the blade, so reducing the lift and hence the aerofoil performance. In the rotor/wake scale the dynamic stall modifies the vorticity distribution in the wake, which results in a strong wake-blade interaction in the downwind part of the rotation.

Finally, the 2D VAWT rotor performance, in terms of power coefficient vs. tip speed ratio, has been computed for two different rotor *Reynolds* numbers. As expected, the power coefficient increases with the rotor *Reynolds* number in the whole operating range of the wind turbine. However, in the present thesis no attempt is made to compare the predicted overall performance with that of a real three dimensional VAWT, since the complex 3D effects (e.g., tip vortices) cannot be either neglected or reproduced by a 2D model.

The present work suggests many hints for future research developments, concerning both possible improvements of the model and its extensive application for the analysis of the influence of important design parameters on the turbine performance. In particular, a remeshing algorithm is under development to smooth the movement of the panel at the separation position. Furthermore, PIV data concerning the pitching aerofoil at other reduced frequencies and *Reynolds* numbers are going to be processed in order to deepen the knowledge of the influence of these parameters on the dynamic stall. As far as the applications to VAWTs are concerned, a useful sensitivity analysis could be performed by analysing the influence of *Reynolds* number, freestream turbulence intensity, number of blades, and aerofoil pitch and camber angles on the turbine performance. However, the most interesting and challenging task is the extension of the present model to three dimensions. Based on the results obtained in the present work, a 3D double wake vortex method exhibits the potential for an accurate simulation of VAWTs with reasonable computational costs when compared to CFD approaches.

A

Laminar Closure Relationships

A.0.1 Skin friction coefficient (C_f)

$$C_f = \begin{cases} \left(0.0727\frac{(5.5-H)^3}{(H+1)} - 0.07\right)\frac{1}{Re_\vartheta}, & \text{if } H < 5.5 \\ \left(0.015\left(1 - \frac{1}{(H-4.5)}\right)^2 - 0.07\right)\frac{1}{Re_\vartheta}, & \text{if } H \geq 5.5 \end{cases} \tag{A.1}$$

A.0.2 Dissipation coefficient (C_D)

$$\frac{2C_D}{H^*} = \begin{cases} \left(0.00205(4-H)^{5.5} + 0.207\right)\frac{1}{Re_\vartheta}, & \text{if } H < 4 \\ \left(\frac{(H-4)^2}{1+0.02(H-4)^2} - 0.0016 + 0.207\right)\frac{1}{Re_\vartheta}, & \text{if } H \geq 4 \end{cases} \tag{A.2}$$

A.0.3 Energy thickness shape parameter (H^*)

$$H^* = \begin{cases} 0.0111\frac{(H-4.35)^2}{H+1} - 0.0278\frac{(H-4.35)^3}{H+1} + & \\ \quad +1.528 - 0.0002(H^2 - 4.35H)^2, & \text{if } H < 4.35 \\ 0.015\frac{(H-4.35)^2}{H} + 1.528, & \text{if } H \geq 4.35 \end{cases} \tag{A.3}$$

B

Turbulent Closure Relationships

B.0.4 Skin friction coefficient (C_f)

$$C_f = \begin{cases} 0.3e^{-1.33H}\left(\frac{log(Re_\vartheta)}{2.3026}\right)^{-1.74-0.31H} & \\ \qquad +0.00011(tanh\left(4-\frac{H}{0.875}\right)-1), & \text{if } Re_\vartheta \geq e^3 \\ 0.3e^{-1.33H}\left(\frac{3}{2.3026}\right)^{-1.74-0.31H} & \\ \qquad +0.00011(tanh\left(4-\frac{H}{0.875}\right)-1), & \text{if } Re_\vartheta < e^3 \end{cases} \tag{B.1}$$

B.0.5 Dissipation coefficient (C_D)

$$\begin{aligned} \frac{2C_D}{H^*} = \frac{C_f U_s}{H^*}\left(\frac{1}{2}+\frac{tanh\left(\frac{(H-1)log(Re_\vartheta)}{2.1}\right)}{2}\right) & \\ +\frac{2C_\tau(0.995-U_s)}{H^*}+0.15\frac{2(0.995-U_s)^2}{Re_\vartheta H^*} & \end{aligned} \tag{B.2}$$

B.0.6 Energy thickness shape parameter (H^*)

$$H_0 = \begin{cases} 3+\frac{400}{Re_\vartheta}, & \text{if } Re_\vartheta > 400 \\ 4, & \text{if } Re_\vartheta \leq 400 \end{cases} \tag{B.3}$$

$$Re_z = \begin{cases} Re_\vartheta, & \text{if } Re_\vartheta > 200 \\ 200, & \text{if } Re_\vartheta < 200 \end{cases} \tag{B.4}$$

$$H^* = \begin{cases} \left(0.5 - \frac{4}{Re_z}\right)\left(\frac{H_0 - H}{H_0 - 1}\right)^2 \frac{1.5}{H + 0.5} + 1.5 + \frac{4}{Re_z}, & \text{if } H < H_0 \\ (H - H_0)^2 \left(\frac{0.007 \ log(Re_z)}{\left(H - H_0 + \frac{4}{log(Re_Z)}\right)^2} + \frac{0.01499}{H}\right) + 1.5 + \frac{4}{Re_Z}, & \text{if } H \geq H_0 \end{cases} \tag{B.5}$$

B.0.7 Equilibrium shear stress coefficient ($C_{\tau eq}$)

$$C_{\tau eq} = \frac{0.014851 H^* \left(H - 1\right)\left(H - 1 - \frac{18}{Re_\vartheta}\right)^2}{(1 - U_s) H^3} \tag{B.6}$$

B.0.8 Normalised wall slip velocity (U_s)

$$U_s = \frac{H^*}{6}\left(\frac{4}{H} - 1\right) \tag{B.7}$$

B.0.9 Boundary layer thickness (δ)

$$\delta = \vartheta\left(3.15 + \frac{1.72}{H - 1}\right) + \delta^* \tag{B.8}$$

B.0.10 $G - \beta$ locus ($\frac{1}{w_e}\left(\frac{\partial w_e}{\partial s}\right)_{eq}$)

$$\frac{1}{w_e}\left(\frac{\partial w_e}{\partial s}\right)_{eq} = \frac{0.5 * C_f - \left(\frac{H - 1 - 18/RT}{6.7H}\right)^2}{0.75 \delta^*} \tag{B.9}$$

C

Wake Closure Relationships

C.0.11 Dissipation coefficient (C_D)

$$\frac{2C_D}{H^*} = \frac{C_f U_s}{H^*} \left(\frac{1}{2} + \frac{tanh\left(\frac{(H-1)log(Re_\vartheta)}{2.1}\right)}{2} \right) + \frac{2C_\tau(0.995 - U_s)}{H^*} + 0.15\frac{2(0.995 - U_s)^2}{Re_\vartheta H^*} \tag{C.1}$$

C.0.12 Energy thickness shape parameter (H^*)

$$H_0 = \begin{cases} 3 + \frac{400}{Re_\vartheta}, & \text{if } Re_\vartheta > 400 \\ 4, & \text{if } Re_\vartheta \leq 400 \end{cases} \tag{C.2}$$

$$Re_z = \begin{cases} Re_\vartheta, & \text{if } Re_\vartheta > 200 \\ 200, & \text{if } Re_\vartheta < 200 \end{cases} \tag{C.3}$$

$$H^* = \begin{cases} \left(0.5 - \frac{4}{Re_z}\right)\left(\frac{H_0-H}{H_0-1}\right)^2 \frac{1.5}{H+0.5} + 1.5 + \frac{4}{Re_z}, & \text{if } H < H_0 \\ (H - H_0)^2 \left(\frac{0.007\ \ log(Re_z)}{\left(H-H_0+\frac{4}{log(Re_z)}\right)^2} + \frac{0.01499}{H} \right) + 1.5 + \frac{4}{Re_Z}, & \text{if } H \geq H_0 \end{cases} \tag{C.4}$$

C.0.13 Equilibrium shear stress coefficient ($C_{\tau eq}$)

$$C_{\tau eq} = \frac{0.014851 H^* (H-1)(H-1)^2}{(1-U_s)H^3} \tag{C.5}$$

C.0.14 Normalised wall slip velocity (U_s)

$$U_s = \frac{H^*}{6}\left(\frac{4}{H} - 1\right) \tag{C.6}$$

C.0.15 Boundary layer thickness (δ)

$$\delta = \vartheta\left(3.15 + \frac{1.72}{H-1}\right) + \delta^* \tag{C.7}$$

C.0.16 $G - \beta$ locus ($\frac{1}{w_e}\left(\frac{\partial w_e}{\partial s}\right)_{eq}$)

$$\frac{1}{w_e}\left(\frac{\partial w_e}{\partial s}\right)_{eq} = \frac{0.5 * C_f - \left(\frac{H-1}{6.03H}\right)^2}{0.75\delta^*} \tag{C.8}$$

References

[1] Darrieus Georges Jean Marie. Turbine having its rotating shaft transverse to the flow of the current. (1835018), December 1931.

[2] Gipe, P. *Wind energy comes on age*. John Wiley & Sons., 1995.

[3] van Bussel, G.J.W., Mertens, S., Polinder, H., and Sidler, H.F.A. Turby®: concept and realisation of a small vawt for the build environment. *The Science of making Torque from Wind. 19-21 April 2004, Delft, The Netherlands*, pages 509–516.

[4] Mertens, S., van Kuik, G.A.M., and van Bussel, G.J.W. Performance of an h-darrieus in the skewed flow on a roof. *Journal of Solar Energy Engineering*, 125(4):433–440, 2003.

[5] Katz, J. and Plotkin, A. *Low Speed Aerodynamics*. Cambridge University Press, 2nd edition edition, 2000.

[6] Burton, T., Sharpe, D., Jenkins, N., and Bossanyi, E. *Wind Energy Handbook*. John Wiley & Sons, 2001.

[7] Sørensen, J.N. and Shen, W.Z. Numerical modelling of wind turbine wakes. *J. Fluids Eng.*, 124(2):393–9, 2002.

[8] Simão Ferreira, C.J. *The near wake of the VAWT, 2D and 3D views of the VAWT aerodynamics*. PhD thesis, Delft University of Technology, 2009.

[9] Hofemann, C., Simão Ferreira, C.J., van Bussel, G.J.W., van Kuik, G.A.M., Scarano, F., and Dixon, K.R. 3d stereo piv study of tip vortex evolution on a vawt. *European Wind Energy Association EWEA*, 2008.

[10] Glauert, H. *The elements of airfoil and airscrew theory.* Cambridge University Press, 2nd edition edition, 1947.

[11] Wilson, R.E. and Lissaman, P.B.S. *Applied Aerodynamics of wind power machines*. Oregon State University, 1974.

[12] Paraschivoiu, I. *Wind Turbine Design with emphasis on Darrieus Concept*. Polythecnic International Press, 2002.

[13] Strickland, J. H., Webster, B. T., and Nguyen, T. Vortex model of the Darrieus turbine: An analytical and experimental study. *NASA STI/Recon Technical Report N*, 80:25887–+, February 1980.

[14] Zanne, L. *Fluid Dynamic Modelling of wind turbines*. PhD thesis, University of Udine, 2010.

[15] Oler, J.W., Strickland, J.H., Im, B.J., and Graham, G.H. Dynamic stall regulation of the darrieus turbine. *Sandia Contract No. 74-1218*, 1983.

[16] Simão Ferreira, C.J., Bijl, H., van Bussel, G., and van Kuik, G. Simulating dynamic stall in a 2d vawt: Modeling strategy, verification and validation with particle image velocimetry data. *Journal of Physics: Conference Series*, 75(1):012023, 2007.

[17] Riziotis, V.A. and Voutsinas, S. G. Dynamic stall modelling on airfoils based on strong viscous inviscid interaction coupling. *International Journal for Numerical Methods in Fluids*, 56:185–208, January 2008.

[18] Galbraith, R.A.McD., Gracey, M.W., and Leitch, E. Summary of pressure data for thirteen aerofoils on the University of Glasgow's aerofoil database. *G.U. Aero Report 9221*, 1992.

[19] Simão Ferreira, C.J., van Kuik, G., van Bussel, G., and Scarano, F. Visualization by piv of dynamic stall on a vertical axis wind turbine. *Experiments in Fluids*, 46:97–108, 2009. 10.1007/s00348-008-0543-z.

[20] Clancy, L.J. *Aerodynamics*. John Wiley & Sons, 1975.

[21] Ponta, F.L. and Jacovkis, P.M. A vortex model for darrieus turbine using finite element techniques. *Renewable Energy*, 24:1–18, 2001.

[22] McIntosh, S.C., Babinsky, H., and Bertenyi, T. Unsteady power output of vertical axis wind turbines operating within a fluctuating free-stream. *46th AIAA Aerospace Sciences Meeting and Exhibit, Reno, Nevada, USA*, 7-10 Jan 2008.

[23] Coton, F.N. Unsteady prescribed wake model for vertical axis wind turbine. *Proceedings of the institution of mechanical engineers*, 208:13–16, 1994.

[24] Schlichting, H., Kestin, J., and Street, R.L. Boundary-layer theory (seventh edition). 1978.

[25] Moran, J. *An introduction to theoretical and computational aerodynamics*. Dover Publication, 2003.

[26] Basu, B.C. and Hancock, G.J. The unsteady motion of a two-dimensional aerofoil in incompressible inviscid flow. *Journal of Fluid Mechanics*, 87:159–178, 1978.

[27] Kundu, P. and Cohen, I. *Fluid Mechanics*. Academin Press, 3th edition edition, 2004.

[28] Voutsinas, S.G. and Riziotis, V.A. A viscous-inviscid interaction model for dynamic stall simulations on airfoils. *AIAA*, 1999.

[29] Vezza, M. and Galbraith, R.A.McD. An inviscid model of unsteady aerofoil flow with fixed upper surface separation. *J. Num. Meth. in Fluids*, 1985.

[30] Katz, J. A discrete vortex method for the non-steady separated flow over an airfoil. *J. of Fluids Mechanics*, 1981.

[31] Fage, A. and Johansen, F.C. On the Flow of Air behind an Inclined Flat Plate of Infinite Span. *Royal Society of London Proceedings Series A*, 116:170–197, September 1927.

[32] Giesing, J.P. Vorticity and Kutta condition for unsteady multi-energy flows. *Trans. A:S:M:E:, J. Appl. Mech.*, 91:608, 1969.

[33] Zanon, A. and Simão Ferreira, C.J. Influence of dynamic stall in the near wake vorticity distribution of a Vertical Axis Wind Turbine. *Torque 2010*, 2010.

[34] Kline, S.J., Morkovin, M.V., Sovran, G., and Cockrell, D. Computation of turbulent boundary layers. *Dept. of Mech. Engrg., Stanford Univ.*, 1968.

[35] M. Drela. Xfoil: an analysis and desing system for low reynolds number airfoil. In University Notre Dame, editor, *Conference on Low Reynolds Number Aerodynamics*, 1989.

[36] Drela, M. Power Balance in Aerodynamic Flows. *AIAA Journal*, 47:1761–1771, July 2009.

[37] M. Drela. *Two-dimensional transonic aerodynamic design and analysis using the euler equation.* PhD thesis, MIT.

[38] Wolles, B.A. and Hoeijmakers, H.W.M. On viscid-inviscid interaction modelling for airfoils as a numerical technique. 1998.

[39] M. Drela. http://web.mit.edu/drela/public/web/xfoil/, XFOIL 6.9.

[40] Kernkamp, G.J. Evaluation and extension of the mathematical model underlying ises. Master's thesis, Delft University of Technology, 1994.

[41] van Ingen, J.L. A suggested semi-empirical method for the calculation of the boundary layer transition region. 1956.

[42] Drela, M. and Giles, M.B. Viscous-inviscid analysis of transonic and low Reynolds number airfoils. *AIAA Journal*, 25:1347–1355, October 1987.

[43] Veldman, A.E.P. *A numerical view on strong viscous-inviscid interaction*, pages 343–363. 1984.

[44] Goldstein, S. On Laminar Boundary-Layer flow near a position of separation. *The Quarterly Journal of Mechanics and Applied Mathematics*, 1(1):43–69, 1948.

[45] Mueller, T.J. The influence of laminar separation and transition on low Reynolds number airfoil hysteresis . *Journal of Aircraft*, 22:763–770, 1985.

[46] Niven, A.J., Galbraith, R.A.McD., and Herring, D.G.F. Analysis of reattachment during ramp down tests. *European Rotorcraft Forum, 14th, Milan, Italy*, 13:187–196, 1988.

[47] Sheng, W., Galbraith, R.A.McD., and Coton, F.N. Return from Airfoil Stall During Ramp-Down Pitching Motions. *Journal of Aircraft*, 44:1856–1864, 2007.

[48] de Kat, R. and van Oudheusden, B.W. Instantaneous planar pressure from piv: analytic and experimental test-case. *15th Int Symp on Applications of Laser Techniques to Fluid Mechanics, Lisbon, Portugal*, pages 154–163, July 2010.

[49] Noca, F., Shiels, D., and Jeon, D. A comparison of methods for evaluating time-dependent fluid dynamic forces on bodies, using only velocity fields and their derivatives. *Journal of Fluids and Structures*, 13(5):551 – 578, 1999.